Sapienza Università di Roma

Modeling Acceleration of a High Brightness Electron Beam by Plasma Wakefield

Author:
Francesco Massimo

Supervisors:
Prof. Luigi Palumbo
Prof. Stefano Atzeni
Co-supervisor:
Dr. Alberto Marocchino

A thesis submitted as partial fulfilment of the requirements
for the degree of Doctor of Philosophy in Accelerator Physics

2015

A great master samurai had three sons, each a skilled fighter. One day he decided to test his three sons and devised the following test: he placed a pillow above the door to his room, balancing it so that it would fall as soon as anyone entered the room, and then summoned each of his sons in turn.

Prior to entering the room, the eldest son immediately sensed something amiss. He cautiously opened the sliding door, extended his hand and caught the pillow when it fell. The second son dodged and caught the falling pillow. The youngest son went straight into the room but he was able to draw his sword and cleave the pillow in two in midair. The master samurai called his three sons together and spoke to them. He praised the eldest son: "You will become a great master samurai." He complimented the progress of the second son: "You as well will become a great master samurai eventually. Persevere and continue to study hard." Finally he severely reprimanded the youngest son: "You are a disgrace. You still need much exercise in the art of swordmanship."

Koan of the samurai and his three sons [1]

---

[1] adapted from *Zen Stories of the Samurai* by N. Dulligan (Global Thinking Books, 2004) and *Budo Sectrets* by J. Stevens (Shambhala Publications, Inc., 2001), inspired by the life of Tsukahara Bokuden.

Abstract

Considerable interest has been shown in the last few decades in the Plasma Wakefield Acceleration (PWFA). This plasma acceleration scheme has demonstrated to produce accelerating gradients greater by at least two orders of magnitude higher than the ones obtainable with conventional accelerating techniques employing radio-frequency metallic cavities. Nonetheless, the quality of the plasma accelerated beams is still not comparable with the one obtainable with conventional accelerating techniques. The modeling and the numerical simulation of Plasma Wakefield Acceleration (PWFA) of electrons are addressed in this work, prompted by the need of studies aimed to improve the quality of the electron beams accelerated through this technique. Models and numerical tools of interest for efficient experimental design for the COMB experiment planned at SPARC_LAB facility in Laboratori Nazionali di Frascati are presented. The issues involved in realizing a plasma acceleration process which maintains the accelerated beams quality and their possible solutions are discussed. The novel time-explicit hybrid kinetic fluid code Architect, developed for this thesis work, is presented and the comparison of its results with the 3D fully kinetic code ALaDyn is shown. The code accuracy and speed make it suitable for quick parametric scans. Applications of the code flexibility in the study of experimental PWFA scenarios are shown in the framework of the COMB experiment.

Contents

Introduction

Particle accelerator applications span from the nuclear and particle physics investigation to medical and industrial uses. Although their role in the scientific research is widely known mainly in the study of elementary particles, they play an essential role also in studies for material science, cultural heritage, biology, medicine and in the electronic industry production. A commonly trait associated to particle accelerators is their size, which in the case of high energy colliders can reach an order of tens of kilometers in their total length. Their size is mainly determined by the highest magnitude of the electromagnetic fields which can be excited to accelerate and deflect charged particles. Since 1979 a novel research field aims to realize a new technology of particle accelerators using plasmas, which can sustain electromagnetic fields orders of magnitude higher than conventional accelerators and thus potentially shrink the technology employed for particle acceleration. Although the generation of such electromagnetic fields and the consequent high energy gains have been widely demonstrated, the particle beams accelerated with these novel techniques still don't have the quality required in conventionally accelerated beams applications.

This thesis work has been developed in the framework of the COMB plasma acceleration experiment, planned at the SPARC_LAB facility in the Laboratori Nazionali di Frascati of INFN, Italy. The COMB experiment is a proof of principle experiment, which aims to demonstrate the realization of high gradients with plasma acceleration while maintaining a quality in the accelerated high brightness electron beams at a level acceptable for applications. The high degree in the control of the accelerated beams in the plasma demands modeling techniques which create a bridge between the fields of accelerator physics and plasma physics. This thesis work focuses on such techniques and tools, aiming in particular to efficiently aid the experimental team efforts in an experiment as COMB.

In Chapter 1 the motivations which led to the rise of the novel field of plasma acceleration are discussed. The plasma acceleration scheme addressed by this work, the Plasma Wakefield Acceleration, is introduced and its main experimental milestones are reported. The issues involved in the modeling and simulation of electron Plasma Wakefield Acceleration are summarized and the COMB experiment is briefly introduced.

In Chapter 2 the kinetic and fluid models of interest for plasma physics and accelerator physics are reviewed, in particular the derivation of the Vlasov-Maxwell description of beam-plasma systems and the definition of the beam quality parameters of interest for this work.

In Chapter 3 a simple 1D fluid model for wakefield excitation is discussed, from which cold relativistic wave breaking limit and Transformer Ratio quantities can be studied.

In Chapter 4 the Particle in Cell (PIC) method for simulating beam-plasma interactions is introduced. the results of a PIC code are compared with the ones obtainable with an extension of the fluid model presented in the previous Chapter.

In Chapter 5 a novel, flexible, time-explicit 2D hybrid kinetic fluid code is presented: Architect. Comparisons against the full 3D PIC code ALaDyn in benchmark scenarios are shown and discussed, as the scaling of the simulation time with the number of beam particles. The code results in different regimes of plasma oscillations are shown and the features of interest of each regimes for the acceleration are reviewed.

In Chapter 6 the COMB experiment is presented in more detail. Applications of Architect of interest for COMB are shown, including matching studies, effect of ramps and radially parabolic profiles in the plasma channel density on the matching. The results of two complete simulations of acceleration with one and three drivers are shown and discussed.

Chapter 1

Plasma acceleration and PWFA: state of the art

In this Chapter the topics and motivations of this thesis work are introduced. The motivations for the study of plasma acceleration and its basic principles are discussed. The main mechanisms, the experimental and theoretical state of art of Plasma Wakefield Acceleration of electrons are briefly summarized. Finally the Plasma Wakefield Acceleration experiment COMB, to which the modeling efforts of this thesis work have been devoted, is introduced.

1.1 Why plasma acceleration

The most controllable method used to increase the energy of charged particles at relativistic energies consists in using an accelerating electric field. With an electrostatic constant field of magnitude E, the maximum energy gain ΔK is proportional to the distance L travelled by the charge:

$$\Delta K = qEL \tag{1.1}$$

If the field varies in time, as in a metallic or dielectric accelerating cavity, the upper bound of the achievable energy gain at relativistic velocities can be estimated with the unrealistic assuption that the charge moves approximately with the same speed of the excited electromagnetic wave. In this ideal scenario, even supposing to have placed the charge at the phase of maximum accelerating field, denoting with E this field, the charge is subject to the same value of field along all the accelerating distance L and the maximum energy gain is still upper bounded by the right hand side of Eq.(1.1). From this limit it is clear that given a certain desired energy gain, the peak feasible electric field determines the minimum accelerating distance which is required and thus the minimum length of the needed accelerating structure; this minumum length does not take into account the necessity of devices, as quadrupole magnets, devoted to focus, control and diagnose the accelerated beam particles.

In the view of this consideration, technologies which allow to obtain higher accelerating gradients are always welcome in the accelerator field, provided that an acceptable degree of control on the particles' trajectory can be maintained. Higher gradients allow to realize smaller (and thus cheaper) and more manageable accelerating systems, either they are destined to high energy colliders for fundamental research or they are devices for applications e.g. radiation sources, medical or industrial accelerators. The present consolidated, stable technology for accelerating structures employs metallic cavities in which oscillating electromagnetic fields are excited. The injection of charged particles in the proper phase of the excited waves to accelerate them. In some cases also the focusing is provided by the electromagnetic fields in the metallic cavities, in other cases it is provided by magnets on the beamline. This technology, now labeled as part of the conventional accelerating techniques, is limited by the breakdown electric field thresholds and the peak achievable accelerating gradients are determined by the field discharge limits in the metallic cavities.

One of the techniques which in the future may overcome the gradient limits of conventional accelerators technology is plasma acceleration. Ionization creates plasmas, thus it does not constitute a problem in a device where the accelerating gradients are created in the plasma itself. When ionization is not a problem, higher gradients than in metallic cavities can be excited, allowing to reach the desired energies in shorter distances. A very rough estimate of the sustainable electric field in a plasma wave yields the cold wave breaking limit [1, 2]:

$$E_{WB}(\mathrm{GV/m}) = \frac{\mathrm{m_e}\omega_\mathrm{p}\mathrm{c}}{\mathrm{e}} \approx 100\sqrt{\frac{\mathrm{n_0}}{10^{18}\,\mathrm{cm^{-3}}}}, \tag{1.2}$$

where n_0 is the initial plasma density. Details on the derivation of Eq.(1.2) and a more accurate estimate which takes into account nonlinear effects are discussed in Chap. 3,

following [2–5]. Such a more accurate limit is higher than the one in Eq.(1.2) in regimes of interest for plasma acceleration. From Eq.(1.2) it can be inferred that with an initial plasma density of $n_0 = 10^{18}\mathrm{cm}^{-3}$, gradients of more than $E \approx\ 100\, GV/m$ can be achieved, three orders of magnitude than the ones achieved in usual linear accelerators.
Although conceptually simple and appealing with respect to potentially achievable peak gradients, plasma acceleration is currently far from replacing the conventional acceleration techniques, due to the difficulty of controlling the particles' trajectories in plasmas.
As discussed in more detail in Section 2.4, the quality of an accelerated beam, or in other words its utility for applications, is not quantified only by the energy reached by some of its particles, but by the requirement that most of them occupies regions of the phase space as compact as possible, i.e. they are compressed in a small spot, have approximately the same energy and are moving approximately in the same direction.
Indeed, although high gradients have been demonstrated, the quality parameters of the plasma accelerated beams, and the acceleration efficiency are far from the ones obtainable by the more controllable conventional acceleration techniques. The low repeatibility of plasma-based accelerator physics also is clashing with the repeatibility of conventional acceleration experiments. Despite the above challenges, plasma acceleration, originally proposed in 1979 [6], has become an established research field aiming to create the new generation of particle accelerators.

1.2 Basic mechanisms of plasma acceleration

The collective behavior of a plasma in response to perturbations of neutrality is the key mechanism of plasma acceleration. This perturbation can be induced by one (or more) intense laser pulse(s) or high energy charged particle beam(s). Such beams may be injected into a gas, which is ionized by the beam itself or in a pre-existing plasma channel. In the wake of this source of perturbation, often referred to as the *driver*, plasma electrons tend to oscillate, creatig a periodic or pseudoperiodic charge distribution and consequently an electric field, called wakefield, which follows the driver in the plasma channel. This wakefield can be used to both accelerate and focus charged particle beams with gradients higher than conventional acceleration techniques.
Since its proposal, the plasma acceleration field developed many schemes characterized

by different ways to excite the wake and to provide the particles that are accelerated, often called the witness particles. This thesis work addresses the acceleration of electrons. A major distinction in plasma electron acceleration schemes is given by laser-driven and beam-driven schemes, depending on the nature of the driver, either it be an intense laser pulse or a high energy charged particle beam. The first plasma acceleration schemes proposed by Tajima and Dawson employed laser pulses as drivers [6]. In the Plasma Beat-Wave Acceleration (PBWA) [7] scheme the beating of two laser pulses excites a wave at plasma frequency ω_p. In the Laser Wake Field Acceleration (LWFA) [7] scheme a single intense laser pulse is used to create the plasma wake. Historically PBWA was proposed as an alternative to LWFA due to the limits of the laser technology in 1979. To overcome some experimetal difficulties as laser pump depletion and diffraction which determined the energy gain limits of laser-driven schemes, the Plasma Wake Field Acceleration (PWFA) scheme was proposed [8], in which the driver is a high energy particle beam. The plasma electron acceleration schemes proposed afterwards (some examples are described in [7, 9]) are all variants of PBWA, LWFA and PWFA. Laser-driven and beam-driven schemes have different advantages and limits, making them suited for different energies and applications.

Another distinction is given by the way in which the witness bunch is injected into the accelerating and focusing phase of the plasma wave. In laser-driven schemes, the witness electrons can be provided by the plasma electrons themselves, injected in the proper phase of the excited plasma waves by spontaneous self-injection effects in highly nonlinear regimes or by means of more controllable triggering mechanisms devised e.g. from partial ionization of the plasma or the tapering of the plasma channel density [7, 10, 11]. The mentioned methods to provide electrons to be accelerated can be referred to as internal injection mechanisms, to distinguish them from the technique in which the witness electrons are injected from outside the plasma channel, or external injection. External injection of relativistic electrons in the plasma wave excited by a laser pulse implies the experimental challenge of synchronizing the laser and electron beams.

1.3 Plasma Wakefield Acceleration

In this Section electron accelerating scheme addressed by this thesis work is described. In 1985 P. Chen [8] proposed the PWFA acceleration scheme to obtain high gradients independent of the high power laser technology. Presently PWFA reaches gradient values unobtainable with LWFA-like schemes due to the diffraction and the depletion of the driving laser pulses in plasmas [12]. Despite the potentially higher energies obtainable, presently PWFA displays the strict experimental requirement of a conventional linear accelerator to provide both the driver and the witness beams to inject in a preformed plasma or in a gas channel. The potential shrinkage of an accelerator by plasma acceleration is not fully obtained in this scheme by this requirement, thus currently PWFA schemes are used to boost the energies of witness beams produced by an existing conventional accelerator. Future plasma colliders schemes are proposed which would self-generate the drivers and witness by LWFA stages and accelerate them to higher energies in multiple PWFA stages [11]. Presently the low quality and repeatibility of the plasma accelerated beams with both LWFA and PWFA (with respect to conventionally accelerated beams) prevents the realization of staged plasma accelerators.
As discussed in more detail in Chap. 3 in the case of PWFA, the magnitude of the perturbation provided by the driver in the plasma initial neutrality determines the regime of the excited plasma waves (see Figs. 3.1, 3.2, 3.3 and 3.4 from [13]). When such perturbation is small, the regime is linear and the excited waves are sinusoidal. Behind an electron driver a region with net positive charge forms due to the repulsion of the plasma electrons by the driver electrons. When the perturbation increases the sinusoids turn into sawtooth waves, reaching nonlinear regimes. In the limit of highly nonlinear regimes the positively charged region behind the driver becomes completely depleted of plasma electrons [14], as shown in Fig. 1.1, hence the name bubble or blowout regime. In the transition to nonlinear regimes the plasma wavelength increases due to the relativistic inertia of the plasma electrons. This has the experimental advantage of a broader region with both focusing and accelerating electric field in which the witness electron bunch can be injected. For this reason and its higher gradients, PWFA in highly nonlinear regimes promises high energy gains and higher beam quality than PWFA in linear regimes. Nevertheless, PWFA in weakly nonlinear regimes has been proposed [18] to maintain the controllability of linear regimes and higher gradients than linear regime plasma waves. A technique studied in this thesis work to obtain high gradients in linear

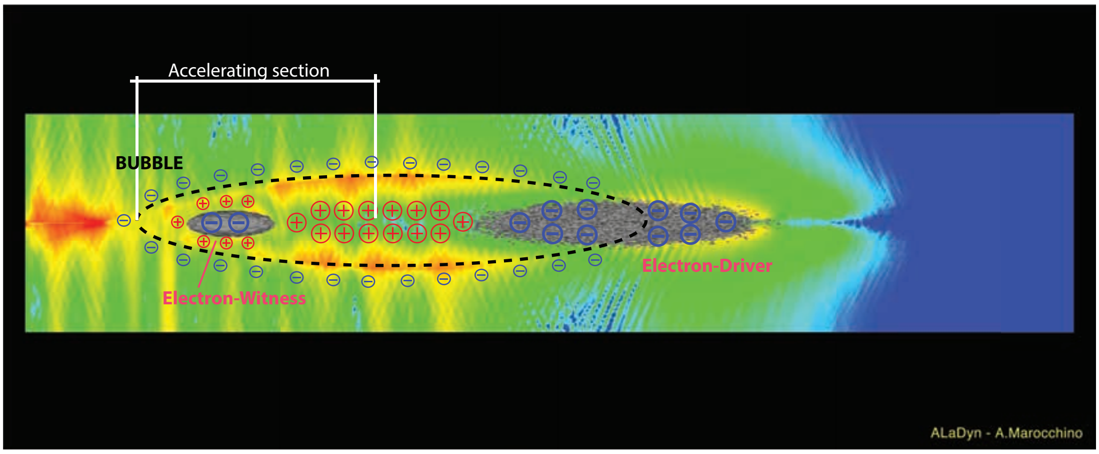

Figure 1.1: Blowout regime. Image by A. Marocchino, simulation performed with 3D PIC code ALaDyn [15–17]

and weakly nonlinear regimes is the resonant excitation of plasma waves by the injection at proper distances of multiple electron bunches [19–21]. This technique implies the experimental issues of synchronization and control in the injection of both the multiple drivers and the witness, as well as the control on the shape of the bunches.

1.3.1 Experimental progress of electron PWFA

Some of the principal milestones of electron PWFA experiments are reported, without any presumption of completeness, only to introduce some of the experimental issues of interest for this thesis work.

In 1988 J. B. Rosenzweig et al. [22] at the Argonne National Laboratory Advanced Accelerator Test Facility measured energy gain variations in correspondence of different witness delay distances from a driver injected in a half-meter scale hollow-cathode dc arc with density of order $n_0 \approx 10^{13}\mathrm{cm}^{-3}$. The spatial period with respect of witness injection distance of these energy gain variations was equal to the plasma wavelength $\lambda_p \approx 10\,\mathrm{mm}$. The peak measured energy gain were smaller than 100 MeV starting with 15 MeV witness electron bunches. This proof of principle was the first experimental observation of electrons accelerated in a PWFA scheme. One year later a similar detection of weakly nonlinear plasma oscillations excited by an electron driver was reported at the same test facility [23].

The quest for high quality and high energy beams found in the blowout regime [14] a potential promise for high gradients and linear focusing fields in the bubble region, similar to the ideal focusing fields in a conventional accelerator. In the first years of the

new century the availability of TW-lasers allowed to reach the bubble regime also in the LWFA [24–26]. Despite the experimental milestones achieved by LWFA in the bubble regime [27, 28], soon the limits in the accelerating distance and consequently in the total energy gains of the laser-driven schemes with respect of beam-driven schemes were recognized. Meanwhile PWFA experiments aimed to demonstrate high energy gains in short distances, even accelerating the electrons in a long driver tail rather than a witness bunch. With this variant of PWFA high gradients were demonstrated in the bubble regime at Stanford Linear Accelerator Center (SLAC) in 2002 [29] and in 2004 [30] in meter-scale plasma channels. In 2005 M. Hogan et al. [31] used an electron driver to both ionize a 10 cm lithium vapor and excite plasma wakefields in the blowout regime, making approximately the 7% of the driver particles on the tail experience a 37 GeV/m average gradient. A main milestone for the highest energies quest was posed in 2007 with the 'Energy Doubling experiment' at SLAC [32], where energy gains of 42 GeV were achieved in a meter-scale plasma channel for some electrons in the tail of the driver.
These experiments consituted a major proof of principle for high energy gains with respect of conventional electron accelerators but the obtained overall quality, i.e. energy spread, emittance (see Section 2.4), repeatibility and efficiency were too low with respect to those obtained with conventional accelerating techniques. A high quality of the witness particles is easier to obtain by accelerating the particles of a witness bunch distinct from the driver. In 2014 an improvement of the acceleration efficiency was obtained through careful utilization of the beam loading by the witness in the bubble regime [12]. To summarize, high gradients were demonstrated with PWFA, but nevertheless better control of the beam dynamics and parameters is needed to obtain induced energy spread and emittances competitive with the ones obtained with conventional accelerating techniques.

1.4 Theory and simulation of electron Plasma Acceleration

In the study of conventional electron accelerators, first assessments can be performed solving Maxwell equations and then the motion equation of electrons in the computed fields. Also, Maxwell equations in the vacuum of the metallic cavity are linear, analytically solvable in simple geometries and numerically solvable with well known methods also in complex geometries.

The first analytical works on electron PWFA performed similar assessments solving the fluid plasma equations with relativistic electron beams as perturbations to the plasma initial neutrality. In the linear regime solutions of these equations in 1D and 2D can be found also analytically [33]. In nonlinear regimes analytical solutions can be found with very simple driver shapes in 1D [34]. Within the fluid approximation, the complexity of the nonlinear relativistic fluid equations needs numerical integration to find the fields in regimes of interest for PWFA and for arbitrary driver shapes in order to perform studies on the physical mechanisms involved, or to study potential experimental working points. For more accurate predictions the self-consistent interaction of the plasma and the relativistic beams must be taken into account. The beams' fields significantly influence the motion of a plasma around them and the plasma induced fields in turn strongly influence the beams traveling through it. Also, the different velocities of near accelerated particles strongly determine the resulting beam quality. These considerations lead to the widespread use of kinetic simulation of PWFA, in particular the use of the Particle in Cell (PIC) method [35–37], discussed in more detail in Chap. 4. PIC codes played an essential role in the study of mechanisms involved in both LWFA and PWFA. For instance the blowout regime was first identified by simulations [14].

The massive increase of the computational power and resources available for PIC simulations allows to accurately study the kinetic details of the 3D plasma-beam interaction, involving also phenomena as collisions and ionization. Nevertheless the amount of resources required for these levels of detail are too massive for the quick parametric studies needed for the design of experiments. Besides, in some regimes of experimental interest not all of these details need to be known. For these reasons, in parallel to massive codes simulating a progressively more complete set of physical phenomena, simpler and quicker models have been developed, the so called reduced models. Examples of such codes include PIC codes with quasi-static approximation [38], e.g. WAKE [39, 40], QuickPIC [41, 42], HiPaCe [43] and codes including hybrid kinetic-fluid models, e.g. LCODE [44], INF&RNO [45], QFluid [46]. A compromise between accuracy and reduced simulation time makes them well suited for the investigation of physical mechanisms in some regimes of interest, preliminary results or validated by full PIC codes. Although they lack some elements of the physics (e.g. quasi-static codes cannot simulate self-injection, hybrid kinetic-fluid models cannot simulate wave-breaking), their use has been proven to be successful in several relevant scenarios [32, 40, 41, 47].

1.5 The COMB experiment

The PWFA experiment called COMB (Coherent plasma Oscillations by Multiple electron Bunches)[1] is planned at SPARC_LAB (Sources for Plasma Accelerators and Radiation Compton with Lasers and Beams) [48] accelerator test facility in the INFN Laboratories of Frascati. The experiment is conceived as a proof of principle, planned to resonantly excite plasma waves by means of a train of bunches [19–21] produced through the laser-comb technique [49] in a preionized plasma channel created by a discharge in hydrogen gas [50] inside a dielectric capillary. Among the goals of the experiment is to maintain a high quality in the accelerated bunches, injected in the plasma with an initial energy of $\approx$ 100 MeV and accelerated in the plasma up to $\approx$ 130 MeV. The plasma waves of COMB will be excited in a plasma channel of nearly uniform density $n_0 = 10^{16}\,\mathrm{cm}^{-3}$ in the weakly nonlinear regime, to maintain a degree of controllability typical of the linear regimes but achieving higher gradients and good features for acceleration (as discussed in Section 5.5) characteristic of the nonlinear regimes. A long term goal is to inject high brightness and low emittance accelerated bunches in the free electron laser (FEL) undulator of the facility, placed immediately after the plasma interaction chamber, demonstrating plasma acceleration with witness quality comparable to that needed for conventional acceleration applications.

The high degree of control of the beam dynamics required in the plasma capillary creates the need for tools to perform quick and flexible systematic studies and to possibly give a feedback to the experimental team in the data analysis. The results and the methods described in this work are primarily aimed to aid the COMB experiment.

---

[1] partially funded by the Italian Minister of Research in the framework of FIRB- Fondo per gli Investimenti della Ricerca di Base, Project no. RBFR12NK5K.

Chapter 2

Accelerator and plasma physics models

For the study of plasma acceleration, the most used models are the kinetic and the fluid models. A brief review of their derivation and main features are reported and discussed, following mainly [36, 51, 52]. Since the regimes of electron plasma acceleration addressed by this thesis work involve relativistic velocities, their study involves the relativistic version of kinetic and fluid descriptions of plasmas and beams[1].

2.1 Kinetic modeling of multiparticle systems

Given a system composed of N interacting identical classical particles, e.g. electrons, if all the positions $\boldsymbol{x}_i(t)$ and momenta $\boldsymbol{p}_i(t)$ ($i = 1, ..., N$) were known, a single distribution function $\mathcal{F}(\boldsymbol{x}, \boldsymbol{p}, t)$ of the system could be defined. The extension to a multi-species system is straightforward, with the definition of a distribution function for each species and taking into account the inter-species interactions. The product of $\mathcal{F}(\boldsymbol{x}, \boldsymbol{p}, t)$ and the infinitesimal phase space volume $d^3x\, d^3p$ would yield the number of particles within that centered in the point $(\boldsymbol{x}, \boldsymbol{p})$ in the single particle phase space μ at time t. Such

---

[1] All the quantities involved in the following are defined in the laboratory frame if not otherwise specified and only effects predicted by special relativity are involved, thus no covariant notation is used, rendering the equations less elegant and general but maybe more physically straightforward. For a complete derivation of a covariant fluid theory from a covariant kinetic theory, see [53].

distribution function would be:

$$\mathcal{F}(\boldsymbol{x},\boldsymbol{p},t)=\sum_{i=1}^{N}\delta(\boldsymbol{x}-\boldsymbol{x}_i(t))\,\delta(\boldsymbol{p}-\boldsymbol{p}_i(t)). \tag{2.1}$$

In the hypothesis of conservation of the number of particles, the function $\mathcal{F}$ would evolve according to the equation:

$$\frac{\partial\mathcal{F}}{\partial t}+\nabla_{\boldsymbol{x}}\cdot\left(\frac{d\boldsymbol{x}}{dt}\mathcal{F}\right)+\nabla_{\boldsymbol{p}}\cdot\left(\frac{d\boldsymbol{p}}{dt}\mathcal{F}\right)=0, \tag{2.2}$$

where $\nabla_{\boldsymbol{x}}$ and $\nabla_{\boldsymbol{p}}$ denote the gradient operators along the position and momentum coordinates. When the interaction forces are constituted by Lorentz forces, in order to know the last term of Eq.(2.2), Maxwell equations with sources depending on $\mathcal{F}$ must be solved as well in a self-consistent way. Thus, integration of Eq.(2.2) is equivalent to solve the N-body electromagnetic problem in the case of a typical plasma for plasma acceleration or a charged particle beam in an accelerator. Besides, the $\mathcal{F}$ function is a completely impractical description of such systems, since it would be impossible to know the mechanical state of all the particles involved, making infeasible any comparison between its predictions and measurements. Indeed macroscopic measurements on the system could not distinguish between many different possible microstates of the system. A more reasonable and manageable description of the system is thus obtained smoothing the distribution function with an average over this ensemble of macroscopically identical systems, often called the Gibbs ensemble [51, 54, 55]. As $\mathcal{F}$ describes the distribution of the particles in the 6-dimensional one-particle phase space μ, a state density function ρ can define the probability density to find the system in a given point of the $6N$-dimensional N-particle phase space Γ, representative of one of the microscopical states in the mentioned ensemble. The probability to find the system in an hypervolume $d^3x_1...d^3x_Nd^3p_1...d^3p_N$ centered in $(\boldsymbol{x}_1,...,\boldsymbol{x}_N;\boldsymbol{p}_1,...,\boldsymbol{p}_N)$ in the Γ space at time t is $\rho(\boldsymbol{x}_1,...,\boldsymbol{x}_N,\boldsymbol{p}_1,...,\boldsymbol{p}_N,t)d^3x_1...d^3x_Nd^3p_1...d^3p_N$. Coherently with this definition of ρ, its integral over the Γ space can be normalized to unity. Conservation of probability yields an evolution equation for ρ, similar to that of the function $\mathcal{F}$ but in the $6N$-dimensional N-particle phase space Γ, given by the continuity equation:

$$\frac{\partial\rho}{\partial t}+\sum_{i=1}^{N}\nabla_{\boldsymbol{x}_i}\cdot\left(\frac{d\boldsymbol{x}_i}{dt}\rho\right)+\sum_{i=1}^{N}\nabla_{\boldsymbol{p}_i}\cdot\left(\frac{d\boldsymbol{p}_i}{dt}\rho\right)=0, \tag{2.3}$$

with the i-th particle position and momentum derivative given by its velocity and total force acting on it:

$$\begin{aligned} \frac{d\boldsymbol{x}_i}{dt} &= \boldsymbol{\beta}_i\, c = \frac{\boldsymbol{p}_i}{m_i\sqrt{1+\left(\frac{\|\boldsymbol{p}_i\|}{m_i c}\right)^2}} \\ \frac{d\boldsymbol{p}_i}{dt} &= \boldsymbol{F}_i, \end{aligned} \tag{2.4}$$

where m_i is the mass of the i-th particle. The term $\frac{d\boldsymbol{x}_i}{dt}$ in Eq.(2.3) can be carried outside the spatial gradient operator, and considering only electromagnetic forces expressed by Lorentz force equation (as in the cases of interest for this work) the term $\frac{d\boldsymbol{p}_i}{dt}$ can be carried out as well from the momentum gradient operator. Under these assumptions the continuity equation (2.3) can be simplified in the form of Liouville theorem:

$$\frac{\partial \rho}{\partial t} + \sum_{i=1}^{N} \frac{d\boldsymbol{x}_i}{dt} \cdot \nabla_{\boldsymbol{x}_i}\rho + \sum_{i=1}^{N} \frac{d\boldsymbol{p}_i}{dt} \cdot \nabla_{\boldsymbol{p}_i}\rho = 0. \tag{2.5}$$

Liouville theorem can be derived for any system whose particles' states evolution can be described by a Hamiltonian and Hamilton equations [56, 57]. Thus the theorem is valid to describe the evolution of a system of interacting particles subject to their internal forces or to external forces which can be included in a Hamiltonian, e.g. external magnetic focusing forces in an accelerator.

The ensemble average of $\mathcal{F}$ yields the one-particle distribution function $f_1 = \langle \mathcal{F}(\boldsymbol{x}, \boldsymbol{p}, t)\rangle$:

$$\begin{aligned} f_1(\boldsymbol{x},\boldsymbol{p},t) &= \int \mathcal{F}(\boldsymbol{x},\boldsymbol{p},t)\rho(\boldsymbol{x}_1,\boldsymbol{x}_2,...,\boldsymbol{x}_N,\boldsymbol{p}_1,\boldsymbol{p}_2,...,\boldsymbol{p}_N,t)d^3x_1...d^3x_N d^3p_1...d^3p_N = \\ &= N\int \rho(\boldsymbol{x},\boldsymbol{x}_2,...,\boldsymbol{x}_N,\boldsymbol{p},\boldsymbol{p}_2...,\boldsymbol{p}_N,t)d^3x_2...d^3x_N d^3p_2...d^3p_N. \end{aligned} \tag{2.6}$$

Each of the integrals performed on the delta functions samples the ρ function on a different particle index, but relabeling the indices and using the invariance of ρ with respect of the argument ordering a single integral multiplied by N is obtained, as can be seen in Eq. (2.6). The scalar $f_1(\boldsymbol{x},\boldsymbol{p},t)d^3x\, d^3p$ represents the value, averaged over the Gibbs ensemble, of particles that can be found in the hypervolume $d^3x\, d^3p$ centered in $(\boldsymbol{x},\boldsymbol{p})$ in μ space at time t. The average value of the distribution function defined on the N particles times the distribution function defined on the remaining $N-1$ particles yields the 2-particle density function f_2, with $f_1(\boldsymbol{x},\boldsymbol{x'},\boldsymbol{p},\boldsymbol{p'},t)d^3xd^3x'd^3pd^3p'$ representing the average product of the number of particles that can be found in the ipervolumes $d^3x\, d^3p$

and $d^3\boldsymbol{x'}d^3\boldsymbol{p'}$ centered in the points $(\boldsymbol{x},\boldsymbol{p})$ and $(\boldsymbol{x'},\boldsymbol{p'})$ in μ space at time t:

$$\begin{aligned} f_2(\boldsymbol{x},\boldsymbol{x'},\boldsymbol{p},\boldsymbol{p'},t) &= \\ &= \frac{N!}{(N-2)!}\int \rho(\boldsymbol{x},\boldsymbol{x'},\boldsymbol{x}_3,...,\boldsymbol{x}_N,\boldsymbol{p},\boldsymbol{p'},\boldsymbol{p}_3,...,\boldsymbol{p}_N,t)d^3x_3...d^3x_Nd^3p_3...d^3p_N. \end{aligned} \tag{2.7}$$

The procedure can be repeated, obtaining the k-particle distribution function f_k specifying k couples position-momentum, with the function ρ integrated over the remaining $N-k$ position-momentum variables and proper multiplying factors. Every distribution function f_k contains more information than the lower order distribution functions. An evolution equation for each f_k can be obtained integrating (2.5) over the $N-k$ position-momentum variables. The set of the N evolution equations constitutes the Bogoliubov–Born–Green–Kirkwood–Yvon hierarchy (BBGKY) hierarchy [51, 54, 55]. For the one-particle distribution f_1, the evolution equation reads:

$$\frac{\partial f_1}{\partial t} + \boldsymbol{\beta}_1\, c\cdot\nabla_{\boldsymbol{x}_1}f_1 + \int \boldsymbol{F}_{1-2}\cdot(\nabla_{\boldsymbol{p}_1}f_2)d^3x_2d^3p_2 = 0, \tag{2.8}$$

where $\boldsymbol{F}_{1-2}$ is the interaction force between the particles in $(\boldsymbol{x},\boldsymbol{p})$ and $(\boldsymbol{x'},\boldsymbol{p'})$. From Eq.(2.8) a feature of all the BBGKY hierarchy can be inferred: the evolution of the distribution function f_k depends on the distribution function of the upper order f_{k+1}. To close the system, and more often to consider only one of the N equations of BBGKY hierarchy, assumptions on the relation between f_1 and f_2 are introduced. In systems where the collisions play a non negligible role, the two-particle distribution function f_2 is often supposed to be the product of the one-particle distribution function plus a correlation term:

$$f_2(\boldsymbol{x},\boldsymbol{x'},\boldsymbol{p},\boldsymbol{p'},t) = f_1(\boldsymbol{x},\boldsymbol{p},t)f_1(\boldsymbol{x'},\boldsymbol{p'},t) + g(\boldsymbol{x},\boldsymbol{x'},\boldsymbol{p},\boldsymbol{p'},t). \tag{2.9}$$

In this hypothesis, the last term of Eq.(2.8), representing the average product of the interaction force F and the gradient along the first particle momentum of f_2, becomes:

$$\begin{aligned} &\int \boldsymbol{F}_{1-2}(\boldsymbol{x}_1,\boldsymbol{x}_2,\boldsymbol{p}_1,\boldsymbol{p}_2)\cdot\left[\nabla_{\boldsymbol{p}_1}f_2(\boldsymbol{x}_1,\boldsymbol{x}_2,\boldsymbol{p}_1,\boldsymbol{p}_2)\right]d^3x_2d^3p_2 = \\ &= \nabla_{\boldsymbol{p}_1}f_1(\boldsymbol{x}_1,\boldsymbol{p}_1)\cdot\int \boldsymbol{F}_{1-2}(\boldsymbol{x}_1,\boldsymbol{x}_2,\boldsymbol{p}_1,\boldsymbol{p}_2)f_1(\boldsymbol{x}_2,\boldsymbol{p}_2)d^3x_2d^3p_2 - \left(\frac{\partial f_1}{\partial t}\right)_{coll,s-s}, \end{aligned} \tag{2.10}$$

where the integral including the correlation term g has been denoted by $-\left(\frac{\partial f_1}{\partial t}\right)_{coll,s-s}$, since the correlations between f_1 and f_2 is related to collisions between particles of the same species (denoted with s). In other words, collisions make ρ and the forces $\frac{d\boldsymbol{p}_i}{dt}$ in the last term of Eq.(2.5) not statistically independent, and the contribution of their correlation can be incorporated in the term $-\left(\frac{\partial f_1}{\partial t}\right)_{coll}$. Inserting Eq.(2.10) into Eq.(2.8) and dropping out the index 1, Boltzmann equation is obtained:

$$\frac{\partial f}{\partial t} + \boldsymbol{\beta}\, c \cdot \nabla_{\boldsymbol{x}} f + \boldsymbol{F} \cdot \nabla_{\boldsymbol{p}} f = \left(\frac{\partial f}{\partial t}\right)_{coll,s-s}, \tag{2.11}$$

where $\boldsymbol{F}(\boldsymbol{x},\boldsymbol{p}) = \int \boldsymbol{F}_{1-2}(\boldsymbol{x},\boldsymbol{x'},\boldsymbol{p},\boldsymbol{p'}) d^3x'\, d^3p'$ is the ensemble averaged force acting on the particles in the μ space point $(\boldsymbol{x},\boldsymbol{p})$. Using the definition of material derivative in μ space $\frac{D}{Dt} = \frac{\partial}{\partial t} + \boldsymbol{\beta}\, c \cdot \nabla_{\boldsymbol{x}} + \frac{d\boldsymbol{p}}{dt} \cdot \nabla_{\boldsymbol{p}}$, Boltzmann equation can be written as:

$$\frac{Df\left[\boldsymbol{x}(t),\boldsymbol{p}(t),t\right]}{Dt} = \left(\frac{\partial f}{\partial t}\right)_{coll,s-s}, \tag{2.12}$$

showing that along the trajectory of a particle in $(\boldsymbol{x},\boldsymbol{p})$ space, f changes only because of collisions. The time sampling of the derivative on the left hand side of Eq. (2.12) is too coarse with respect to collision characteristic times, thus a collision between two particles would be graphically represented in μ space as an istantaneous apparent destruction of two particles in the collision point and the apparent creation of particles with the new momenta in other points of μ space, as sketched in Fig. 2.1. The change in f given by the collisions is analitically represented by the term on the right hand side of Eq.(2.12).

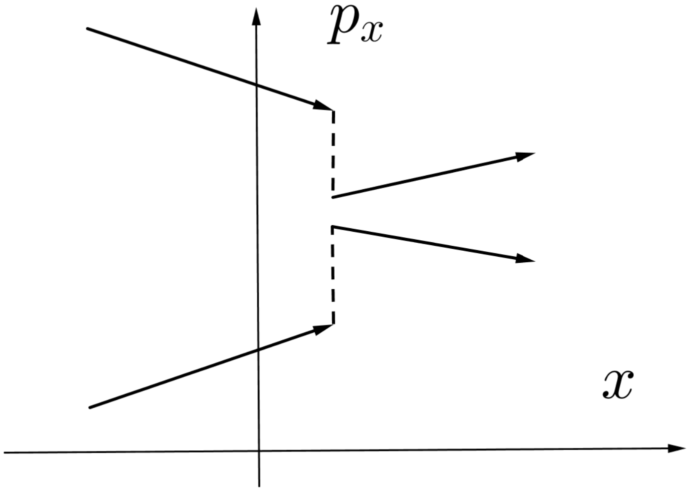

Figure 2.1: Representation of a binary collision in the phase space $x - p_x$.

2.2 Vlasov Equation and Vlasov-Maxwell system

For the physical mechanisms addressed in this work a kinetic description as the one illustrated in the previous Section is suitable to describe plasma and high energy beam particles. Besides, since the plasma frequency f_p is much greater than the highest collision frequencies (see Appendix A), on the timescales of interest for this thesis work the collisions between the particles can be neglected. Thus the correlation term in Eqs.(2.9) and the averaged one in Eqs.(2.15, 2.12) can be neglected, yielding the collisionless Boltzmann equation, or Vlasov equation:

$$\frac{\partial f}{\partial t} + \boldsymbol{\beta}\, c \cdot \nabla_{\boldsymbol{x}} f + \boldsymbol{F} \cdot \nabla_{\boldsymbol{p}} f = 0. \tag{2.13}$$

In the Vlasov approximation the density function f does not change along the trajectory of a particle in the single particle phase space μ. Formally, the left-hand side of Vlasov equation can be seen as a directional derivative in the hyperplane $(\boldsymbol{x}, \boldsymbol{p}, t)$ along the vectors tangent to particular curves in such hyperplane. The coordinates of these curves can be parametrized by time, i.e. $\boldsymbol{x}(t), \boldsymbol{p}(t)$, thus Vlasov equation can be rewritten as:

$$\frac{df(\boldsymbol{x}(t), \boldsymbol{p}(t), t)}{dt} = \left(1, \frac{d\boldsymbol{x}}{dt}, \frac{d\boldsymbol{p}}{dt}\right) \cdot \left(\frac{\partial f}{\partial t}, \nabla_{\boldsymbol{x}} f, \nabla_{\boldsymbol{p}} f\right) = 0. \tag{2.14}$$

Comparison with Eq.(2.13) yields the equations describing the curves along which the value of f does not change, i.e. the characteristics of Vlasov equation:

$$\begin{aligned} \frac{d\boldsymbol{x}(t)}{dt} &= \boldsymbol{\beta}\, c, \\ \frac{d\boldsymbol{p}(t)}{dt} &= \boldsymbol{F}, \end{aligned} \tag{2.15}$$

which turn out to be the single particle equations.

Since the ions have a mass greater with respect to the electrons at least by a factor ≈ 2000, their acceleration when subject to an electromagnetic force is smaller by a the same factor with respect to the acceleration of the electrons subject to the same force. Thus, in the timescales of interest of this thesis work the motion of the plasma ions can be neglected. They are then modeled as a uniform immobile background with constant uniform density n_0. For the sake of simplicity, the plasma is assumed composed of monoatomic ions, thus the charge equilibrium in any region is obtained when $n_e = n_0$. The extension to plasmas with atomic number $Z > 1$ can be easily derived.

In these hypotheses, $f(\boldsymbol{x},\boldsymbol{p},t)$, whose evolution is governed by Vlasov equation, will henceforth denote the distribution function of the plasma and high energy beam electrons, i.e. $f(\boldsymbol{x},\boldsymbol{p},t) = f_e(\boldsymbol{x},\boldsymbol{p},t) + f_b(\boldsymbol{x},\boldsymbol{p},t)$, where $f_e(\boldsymbol{x},\boldsymbol{p},t)$ and $f_b(\boldsymbol{x},\boldsymbol{p},t)$ denote, respectively the plasma electrons and the beam electrons distribution function. For the sake of coherence with this notation, fluid quantities with the subscript e and b will henceforth denote the quantities referred to the plasma electrons and the beam electrons.

To obtain a self consistent model of the system Vlasov equation must be coupled with the Lorentz force equation and Maxwell equations for the ensemble averaged fields, obtaining the Vlasov-Maxwell system. The electron charge density and current density can then be obtained from:

$$\begin{aligned} n(\boldsymbol{x},t) &= \int f(\boldsymbol{x},\boldsymbol{p},t)d^3p \\ \boldsymbol{J}(\boldsymbol{x},t) &= -e\langle\boldsymbol{\beta}\rangle_f c = -ec\int \boldsymbol{\beta} f(\boldsymbol{x},\boldsymbol{p},t)d^3p, \end{aligned} \tag{2.16}$$

where the symbol $\langle\boldsymbol{\beta}\rangle_f$ denotes the average normalized velocity at position and time $\boldsymbol{x}, t$, with the average operation defined on the distribution function f.

With the discussed approximations and notations, Vlasov-Maxwell system in the plasma takes the form

$$\begin{aligned} \frac{\partial f}{\partial t} + \boldsymbol{\beta} c \cdot \nabla_{\boldsymbol{x}} f - e\left(\boldsymbol{E} + \boldsymbol{\beta} c \times \boldsymbol{B}\right) \cdot \nabla_{\boldsymbol{p}} f = 0 \\ \nabla \times \boldsymbol{E} = -\frac{\partial \boldsymbol{B}}{\partial t} \\ \nabla \times \boldsymbol{B} = -\mu_0 ec\left(\int \boldsymbol{\beta} f d^3p\right) + \frac{1}{c^2}\frac{\partial \boldsymbol{E}}{\partial t}. \end{aligned} \tag{2.17}$$

In the next Section it is shown that from the first of Eqs.(2.17) the continuity equation

$$-e\frac{\partial n}{\partial t} + \nabla \cdot \boldsymbol{J}(\boldsymbol{x},t) = 0 \tag{2.18}$$

can be derived; Equation (2.18), coupled with the curl equations in Eq.(2.17), yields the divergence equations for the electromagnetic fields:

$$\begin{aligned} &\nabla \cdot \boldsymbol{E} = \frac{e}{\varepsilon_0}\left(n_0 - \int f d^3p\right) \\ &\nabla \cdot \boldsymbol{B} = 0. \end{aligned} \tag{2.19}$$

In the next Sections some applications of the Vlasov-Maxwell system aimed to model plasmas for plasma acceleration and particle beams in an accelerator are shown.

2.3 Fluid modeling of particle beams and plasmas

When the difference of momentum of different particles in the same infinitesimal space volume d^3x is not relevant the kinetic description of the system in μ space by $f(\boldsymbol{x}, \boldsymbol{p}, t)$ contains more information than needed. The relevant information in those cases can be condensed in physical quantities closer to the physical intuition, as density, temperature and pressure of the system in a specified region of the physical space. These coarse grained quantities are obtained averaging the properties of the particles at the same point but with different momentum, as shown in the shaded area of Fig. 2.2. The model obtained with this averaging constitutes the fluid description of the considered gas or plasma [51, 52].

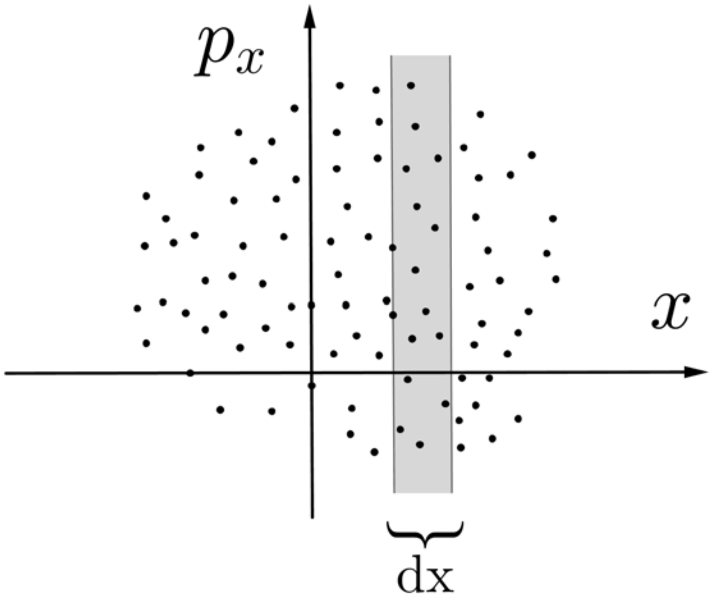

Figure 2.2: 1D fluid averaging: the fluid quantities at coordinate x are obtained averaging over the particles in the interval $(x, x + dx)$ in the shaded area.

The physical quantities involved in the fluid description are the first moments of the distribution function in the momentum space and their evolution is described by moments of Vlasov equation in the momentum space. The m-th moment of the distribution function in the momentum space is:

$$\int \underbrace{\boldsymbol{p} \otimes ... \otimes \boldsymbol{p}}_{\text{m times}} f(\boldsymbol{x}, \boldsymbol{p}, t) d^3 p, \tag{2.20}$$

where the symbol $\otimes$ indicates the tensor product. The zeroth-order moment ($m = 0$) represents the particle density (or the number of particles per unit volume) of the system. As assumed in the previous Section, for the description of an electron plasma accelerator the electron distribution function f can be defined as the sum of the distribution functions f_e and f_b referred to the plasma and the beam electrons, thus the obtained density will be the sum of the particle density of the plasma and beam electron fluids:

$$n_e(\boldsymbol{x}, t) + n_b(\boldsymbol{x}, t) = \int f(\boldsymbol{x}, \boldsymbol{p}, t) d^3 p = \int f_e(\boldsymbol{x}, \boldsymbol{p}, t) d^3 p + \int f_b(\boldsymbol{x}, \boldsymbol{p}, t) d^3 p \tag{2.21}$$

Analogously the first order moment ($m = 1$) represents the density of momentum of the fluid system, divided by the species mass. The momentum density can be split in the product of the fluid particle density times the fluid momentum. The separated moments on the two distribution functions yield the momentum densities of the plasma and beam electron fluid species:

$$\begin{aligned} n_e(\boldsymbol{x}, t)\boldsymbol{p}_e(\boldsymbol{x}, t) &= \textstyle\int \boldsymbol{p} f_e(\boldsymbol{x}, \boldsymbol{p}, t) d^3 p, \\ n_b(\boldsymbol{x}, t)\boldsymbol{p}_b(\boldsymbol{x}, t) &= \textstyle\int \boldsymbol{p} f_b(\boldsymbol{x}, \boldsymbol{p}, t) d^3 p. \end{aligned} \tag{2.22}$$

with the fluid momentum satisfying the related relativistic relations with the fluid quantities γ and $\boldsymbol{\beta}$:

$$\begin{aligned} \boldsymbol{p}_e(\boldsymbol{x}, t) &= m_e \gamma_e(\boldsymbol{x}, t) \boldsymbol{\beta}_e(\boldsymbol{x}, t) c, \\ \boldsymbol{p}_b(\boldsymbol{x}, t) &= m_e \gamma_b(\boldsymbol{x}, t) \boldsymbol{\beta}_b(\boldsymbol{x}, t) c; \\ \gamma_e(\boldsymbol{x}, t) &= \sqrt{1 + (\|\boldsymbol{p}_e(\boldsymbol{x}, t)\| / m_e c)^2}, \\ \gamma_b(\boldsymbol{x}, t) &= \sqrt{1 + (\|\boldsymbol{p}_b(\boldsymbol{x}, t)\| / m_e c)^2}; \\ \boldsymbol{\beta}_e(\boldsymbol{x}, t) &= \tfrac{\boldsymbol{p}_e(\boldsymbol{x}, t)}{m_e c \gamma_e(\boldsymbol{x}, t)}, \\ \boldsymbol{\beta}_b(\boldsymbol{x}, t) &= \tfrac{\boldsymbol{p}_b(\boldsymbol{x}, t)}{m_e c \gamma_b(\boldsymbol{x}, t)}. \end{aligned} \tag{2.23}$$

The moments of Vlasov equations in momentum space yield the fluid equations in Eulerian description [58, 59]. The zeroth order moment is:

$$\int \left(\frac{\partial f}{\partial t} + \boldsymbol{\beta}\, c \cdot \nabla_{\boldsymbol{x}} f + \boldsymbol{F} \cdot \nabla_{\boldsymbol{p}} f \right) d^3p = 0, \tag{2.24}$$

where $f(\boldsymbol{x}, \boldsymbol{p}, t) = f_e(\boldsymbol{x}, \boldsymbol{p}, t) + f_b(\boldsymbol{x}, \boldsymbol{p}, t)$. The partial derivation with respect of time and the nabla operator in position space can be carried out of the integral in the momentum space. The integral of the last term vanishes, using the integration by parts and the vanishing of f at infinite values of momentum (reasonable hypothesis also in non-relativistic regimes). The result of the averaging is the continuity equation for the sum $n(\boldsymbol{x}, t)$ of the beam electron density $n_b(\boldsymbol{x}, t)$ and plasma electron density $n_e(\boldsymbol{x}, t)$:

$$\frac{\partial n}{\partial t} + c \nabla_{\boldsymbol{x}} \cdot (\boldsymbol{\beta} n) = 0. \tag{2.25}$$

The continuity density shows a feature common to all the moments of Vlasov equation: the evolution of a moment of the distribution function depends on a moment of higher order, e.g. the evolution of the density depends also on the fluid velocity, related to the second order moment of f. As with the BBGKY hierarchy, a closure of the fluid equations is needed, typically in the form of an equation of state which relates the fluid quantities involved in the fluid equations. The choice of this equation depends on the hypotheses which suit better to the studied phenomena [53, 58, 59]. To study high energy beam dynamics in typical plasmas for plasma acceleration, the cold fluid hypothesis is a reasonable truncation scheme. This holds as long as the thermal velocity of the particles is negligible with respect to all relevant wave phase velocities. The thermal components of velocity, which in hot fluid approximation give rise to the second order moments quantities of pressure and temperature, are thus supposed equal to zero. Consequently fluid pressure and temperature are considered null, and in the momentum equation the only forces appearing are the electromagnetic forces. Such truncation scheme corresponds to a trivial equation of state, fixing to zero the pressure of the system. In the case of plasma acceleration the oscillations are mostly driven by the excited EM fields, thus neglecting the pressure term in the momentum equation is a reasonable approximation. When thermal effects cannot be neglected, the choice of an equation of state to retrieve the same dispersion relation for relativistic waves from both Vlasov equation and the fluid equations is not straightforward [60].

Taking the first moment of Vlasov equation in momentum space in the cold fluid approximation, with simplifications similar to the those used to derive Eq.(2.25), subtracting Eq.(2.25), using the identities $\nabla_{\boldsymbol{p}}\boldsymbol{F} = \nabla_{\boldsymbol{p}}\left(\boldsymbol{E} + \boldsymbol{\beta}\, c \times \boldsymbol{B}\right) = 0$ and $\frac{\partial p_i}{\partial x_j} = \delta_{ij}$ [2], multiplying by the species mass and dividing by the density, the cold fluid momentum equation in Eulerian form is obtained:

$$\frac{\partial \boldsymbol{p}}{\partial t} + \boldsymbol{\beta}\, c \cdot \nabla_{\boldsymbol{x}}\boldsymbol{p} = -e\left(\boldsymbol{E} + \boldsymbol{\beta}\, c \times \boldsymbol{B}\right). \tag{2.26}$$

Maxwell equations with fluid source terms and Eq.(2.26) constitute the cold fluid model:

$$\begin{aligned}
\frac{\partial \boldsymbol{p}}{\partial t} + \boldsymbol{\beta}\, c \cdot \nabla_{\boldsymbol{x}}\boldsymbol{p} &= -e\left(\boldsymbol{E} + c\boldsymbol{\beta} \times \boldsymbol{B}\right) \\
\nabla \cdot \boldsymbol{E} &= \frac{e}{\varepsilon_0}\big(n_0 - n_e - n_b\big), \\
\nabla \cdot \boldsymbol{B} &= 0, \\
\nabla \times \boldsymbol{E} &= -\frac{\partial \boldsymbol{B}}{\partial t}, \\
\nabla \times \boldsymbol{B} &= -\mu_0 e c\big(n_e\boldsymbol{\beta}_e + n_b\boldsymbol{\beta}_b\big) + \frac{1}{c^2}\frac{\partial \boldsymbol{E}}{\partial t},
\end{aligned}$$

where the subscript b refers to the beam quantities. The continuity equation (2.25) is implied in the model, since it can be obtained taking the divergence of the fifth equation and substituting the second equation of the system (2.27). The momentum $\boldsymbol{p}$ is the sum of the fluid momentum of the beam and of the plasma electrons. Thus, the first of Eqs.(2.27) could in principle be decomposed in two momentum equations for the two electron species. In the next Chapter, within the approximation of the model described there, only the momentum equation for the plasma electrons is considered, since the beam distribution is considered rigid.

2.4 Particle beam acceleration and beam quality preservation

The different velocities of high energy beam particles play a significant role in their most common applications [61, 62]. A charged particle beam is as much desirable for applications as much as its particles are compressed in a region of space, have similar

---

[2] the last identity holds in cartesian coordinates, but the final result in the last equality of Eq.(2.26) is the same in other coordinate systems.

energy and similar directions in momentum. For this reason a fluid description is not suitable to describe the quality of a high energy beam. A kinetic description is required instead. A distribution function $f_b(\boldsymbol{x}, \boldsymbol{p}, t)$ can describe the beam particle distribution in the phase space, but it still contains too much information for a concise expression of the beam quality. Statistical integrated parameters are defined, starting from f_b to provide an overall description of the whole beam or of the single accelerated bunches. For the purpose of this thesis work the most important integrated parameters are beam emittance, average energy, energy spread and brightness. In this Section their definition and some main properties are discussed.

The typical reference system used in the study of particle acceleration is sketched in Fig. 2.3. The curvilinear coordinate z indicates the position of the beam centroid along the design trajectory. The particle position $\boldsymbol{r}$ along the accelerator is specified by z and the displacement with respect of the design trajectory, x and y. In the case of linear accelerators the curvature radius of the design trajectory $\rho(z)$ is assumed equal to infinite. Referring to the positions and momenta with respect to this reference system a distribution function $f_b(x, y, z, p_x, p_y, p_z, t)$ of the beam particles can be defined. It is convenient to normalize to unity the integral of the distribution function over the beam phase space:

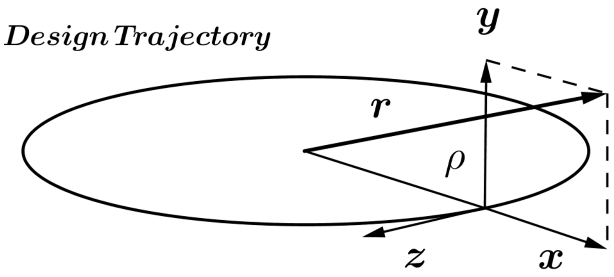

Figure 2.3: Reference system for the particle trajectory in a particle accelerator.

$$\int f_b(x, y, z, p_x, p_y, p_z, t) dx dy dz dp_x dp_y dp_z = 1. \tag{2.27}$$

In the hypothesis of absence of coupling between longitudinal and transverse phase planes and of coupling between the two transverse planes, it is conventient to decompose the distribution function as the product of three different distribution functions, i.e.

$$f_b(x, y, z, p_x, p_y, p_z, t) = f_x(x, p_x, z, t) f_y(y, p_y, z, t) f_z(z, p_z, t). \tag{2.28}$$

Such a factorizations allows to study the transverse and longitudinal evolution of the beam during its motion in the accelerator. The beam rms normalized emittance [63–65] on the transverse plane $x - p_x$ is defined starting from the rms displacements and momenta and the covariance of the distribution function $f_x(x, p_x, z)$:

$$\sigma_x^2(z,t) = \langle x^2 \rangle = \int x^2 f_x(x,p_x,z,t)dxdp_x \tag{2.29}$$

$$\sigma_{p_x}^2(z,t) = \langle p_x^2 \rangle = \int p_x^2 f_x(x,p_x,z,t)dxdp_x \tag{2.30}$$

$$\sigma_{x,p_x}(z,t) = \langle xp_x \rangle = \int xp_x f_x(x,p_x,z,t)dxdp_x. \tag{2.31}$$

The transverse covariance is negative when the beam particle trajectories are mainly converging towards the axis and positive when they are mainly diverging. A particle beam with high rms momentum spread or rms width with respect to the design orbit is less desirable for applications, as it is a beam that is highly diverging or too wide. Such transverse quality requirements can be summarized as a low value of the normalized rms emittance parameter $\varepsilon_{n,rms}$, defined by:

$$\varepsilon_{n,rms} = \frac{1}{m_e c}\sqrt{\sigma_x^2\sigma_{p_x}^2 - \sigma_{x,p_x}^2}, \tag{2.32}$$

where the momentum is normalized by $m_e c$ for an electron beam. The same definition applies for the emittance on the transverse plane $y - p_y$ with the substitution of the quantities with respect of y axis in Eq.(2.32). The emittance along the $x - p_x$ plane is related to the area occupied by the beam in that plane, this is often the definition used to quantify the beam emittance in place of the rms definition in Eq.(2.32). There are also other definitions of emittance [63–65], but the beam quality behavior with respect of nonlinear collective effects and the disorder in the transverse particle distribution in the phase space can be best summarized in the definition of rms emittance than with other definitions [63, 64, 66], thus in this work the term emittance refers to the rms emittance. The rms emittance is frequently defined in terms of the positions and the divergence $x' = \frac{dx}{dz} =$ of the particles. The momentum along the x axis for ultrarelativistic particles (i.e. with velocity $\frac{dz}{dt} \approx c$) is expressed in terms of x' as:

$$p_x = m_e\gamma\beta_x c = m_e\gamma\frac{dx}{dt} = m_e\gamma\frac{dx}{dz}\frac{dz}{dt} = m_e\gamma x'\beta_z c, \tag{2.33}$$

as shown in Fig. 2.4. Under the paraxial approximation $\beta_x \approx \beta$ the transverse mo-

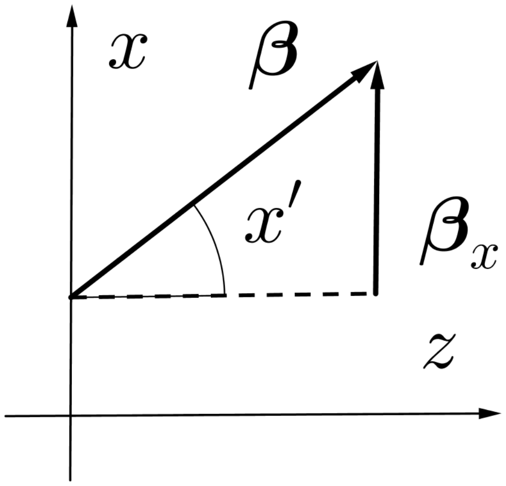

Figure 2.4: Divergence of a particle trajectory along the x axis.

mentum can be written as $p_x = px' = m\gamma\beta x'c$ and the normalized emittance is given by:

$$\epsilon^2_{n,rms} = \sigma^2_x \sigma^2_{\gamma\beta x'} - \sigma^2_{x,\gamma\beta x'}. \tag{2.34}$$

Another common definition of emittance is that referred to as the rms geometrical emittance ε_g:

$$\epsilon^2_g = \sigma^2_x \sigma^2_{x'} - \sigma^2_{xx'}. \tag{2.35}$$

Interest in normalized emittance in conventional accelerators is motivated by its conservation along the beamline when the beam is subject to Hamiltonian forces. From a mechanical point of view, in presence of acceleration at relativistic velocities, the area occupied by the beam in the phase space $x - p_x$, related to the normalized emittance, is conserved as consequence of Vlasov equation [3], while the area occupied in the trace space $x - x'$, corresponding to the geometrical emittance, is instead not conserved. Radiation emission, nonlinear space charge forces, wake fields created by the interaction with a metallic accelerating cavity are examples of phenomena which do not conserve the normalized emittance. A more exhaustive list of phenomena which cause variations of the normalized emittance can be found in [63, 65, 67]. Formally, in presence of Hamiltonian forces the transverse phase space whose area is conserved refers to the position x and canonical momentum $P_x = p_x - eA_x$. Nevertheless in an accelerator the magnetic

---

[3] In particle accelerator literature the incompressibility of the phase space volume of the beam is often stated as deriving from Liouville's theorem. This is not strictly correct: as discussed in the previous Sections, Liouville's theorem refers to the conservation of the density of states in a 6N-dimensional phase space [67].

fields are mainly transverse, thus the vector potential $\boldsymbol{A}$ is mainly longitudinal. With the proper gauge condition its transverse components times the electron charge can be set to negligible values with respect to transverse mechanical momentum, which under the same assumption nearly equals the transverse canonical momentum, i.e. $P_x \approx p_x$.
In many applications, as radiation sources, beams with low emittance as well as low energy spread in the beam particles is required [61, 62]. In plasma accelerators a low energy spread is mandatory to have low normalized emittance [68, 69], as can be inferred by substituting the definition of relative energy spread σ_E

$$\sigma_E^2 = \frac{\sigma_{\beta\gamma}^2 - \langle\beta\gamma\rangle^2}{\langle\gamma\rangle^2} \tag{2.36}$$

in the definition of normalized rms emittance (Eq. (2.34)):

$$\epsilon_{n,rms}^2 = \langle\gamma\rangle^2\sigma_E^2\sigma_x^2\sigma_{x'}^2 + \langle\beta\gamma\rangle^2(\sigma_x^2\sigma_{x'}^2 - \sigma_{x,x'}^2). \tag{2.37}$$

The geometrical emittance ε_g of the beam is found in the last term of the right hand side of Eq.(2.37). In a conventional accelerator the first term in the right hand side of Eq.(2.37) is negligible, thus the normalized emittance corresponds to the geometrical emittance times the average beam energy. One of the main issues of beam quality preservation in plasma accelerators is that they produce beams with higher energy spread than conventional accelerators. As can be inferred from Eq.(2.37), even a small-sized and low-divergent beam can grow to high normalized emittance if the energy spread grows up to not negligible values.
A low beam emittance is also important to obtain a high beam brightness B, defined as [63, 65]:

$$B = \frac{2I}{\varepsilon_x\varepsilon_y}. \tag{2.38}$$

Short particle bunches and thus high current bunches and low emittance values are needed to maximize the brightness. High values of brightness are required for high quality radiation sources [61, 62].

2.5 Beam envelope equations

As can be intuitively inferred from Eq.(2.34) the emittance characterizes the collimation of a particle beam, as well as its transverse dimension. The exact relation between the emittance and the beam size is expressed in the beam envelope equations. The computation of the second derivative of the rms beam size, or envelope $\sigma_x(z)$ with respect to z and the substitution of the emittance definition yields the envelope equation [65, 70, 71]. Denoting the derivation with respect of z with the prime symbol, under the paraxial approximation the envelope equation reads as

$$\sigma_x'' + \frac{p'}{p}\sigma_x' - \frac{\langle xF_x\rangle}{\sigma_x\beta cp} = \frac{\varepsilon_{n,rms}^2}{\gamma^2\sigma_x^3}. \tag{2.39}$$

All the forces to which the beam is subject are included in the average term $\langle xF_x\rangle$. In a conventional accelerator the more relevant forces included are the external forces, often represented by focusing forces (e.g. provided by solenoids or quadrupoles) and the internal Coulombian repulsion forces between the beam particles, called the space charge forces [72]. A Debye length (see Appendix A, [65]) associated to a point inside the beam can be defined:

$$\lambda_D = \sqrt{\frac{\gamma^2\varepsilon_0 k_B T_b}{e^2 n_b}}, \tag{2.40}$$

where γ is the average Lorentz factor of the beam, k_B is the Boltzmann constant, n_b is the local beam density and $T_b = \gamma m_e\langle v_\perp^2\rangle$ is the local beam temperature ($\langle v_\perp^2\rangle$ is the rms perpendicular velocity spread). When the Debye length defined inside the beam is much smaller than the beam size the average fields effects prevail on the binary collisions'. In this case smooth functions can be used to study the space charge fields, which can be added to the external forces which affect the beam behavior.

At relativistic energies the longitudinal space charge forces are negligible with respect to the transverse ones, thus only the latter are included in the envelope equation. Denoting the defocusing transverse space charge forces as $F_{x,sc}$ and the transverse external forces $F_{x,ext}$, Eq. (2.39) becomes:

$$\sigma_x'' + \frac{p'}{p}\sigma_x' - \frac{\langle xF_{x,ext}\rangle}{\sigma_x\beta cp} = \frac{\varepsilon_{n,rms}^2}{\gamma^2\sigma_x^3} + \frac{\langle xF_{x,sc}\rangle}{\sigma_x\beta cp}. \tag{2.41}$$

The emittance can be recognized in Eq.(2.41) as one of the driving terms causing beam expansion. At typical energies and beam rms sizes of plasma accelerators the emittance term largely prevails on the space charge term [71] (emittance-dominated regime), making the former the only driving term in Eq.(2.41):

$$\sigma_x'' + \frac{p'}{p}\sigma_x' - \frac{\langle x F_{x,ext} \rangle}{\sigma_x \beta c p} = \frac{\varepsilon_{n,rms}^2}{\gamma^2 \sigma_x^3}. \tag{2.42}$$

A bunch injected in a focusing channel with an initial transverse rms size σ_x equal to the equilibrium value computed (when possible) from Eq.2.41 or near that value and with $\sigma_x' = 0$ (condition often referred to as beam at waist) in order to minimize its envelope (often called also betatron) oscillations is said to be matched to that channel. A good matching of a bunch can prevent it to be subject to instabilities which cause a growth of emittance.

Chapter 3

The basic underlying physics: fluid 1D model

The witness bunch achievable maximum energy strongly depends on the wave in which it is placed in the plasma channel. Usually in conventional accelerators the witness bunch weakly interacts with the accelerating or deflecting wave by locally changing the wave form, i.e. beam loading the field. In plasma accelerators the witness bunch can strongly change and interact with the field in which it is transported. A full self-consistent model of plasma acceleration would take into account in every instant the field generation by the driving beam and the witness bunch and their mutual interaction. Nevertheless, as it is shown in this Chapter, many qualitative and quantitative considerations can be inferred only by taking into account the field generated by a given distribution of bunches in a plasma channel within a fluid framework.

3.1 Nonlinear wave equation

In most cases of interest for PWFA, the characteristic oscillation velocities are much greater than the velocities associated with thermal motion, hence the cold fluid model Eqs.(2.27) provides a valid tool for qualitative estimates of the excited field. In its derivation the ion motion was neglected in the timescales of interest, thus the relevant equations are the electron fluid momentum equation and Maxwell equations, in which the ions are distributed with uniform density n_0:

$$\begin{aligned}
\frac{\partial \mathbf{p}_e}{\partial t} + \boldsymbol{\beta}_e c \cdot \nabla \mathbf{p}_e &= -e(\mathbf{E} + \boldsymbol{\beta}_{\boldsymbol{e}} c \times \mathbf{B}) \\
\mathbf{p}_e &= \frac{m_e \boldsymbol{\beta}_e c}{\sqrt{1 - \|\boldsymbol{\beta}_e\|^2}} \\
\nabla \cdot \mathbf{E} &= \frac{e}{\varepsilon_0}(n_0 - n_e - n_\mathrm{b}) \\
\nabla \cdot \mathbf{B} &= 0 \\
\nabla \times \mathbf{E} &= -\frac{\partial \mathbf{B}}{\partial t} \\
\nabla \times \mathbf{B} &= -e\mu_0 \left(n_e \boldsymbol{\beta}_e c + n_\mathrm{b} \boldsymbol{\beta}_\mathrm{b} c\right) + \frac{1}{c^2}\frac{\partial \mathbf{E}}{\partial t},
\end{aligned} \tag{3.1}$$

where the subscripts b, e refer respectively to the beam and the plasma electron quantities. Phisically n_b could represent either a single driving bunch, a sequence of properly spaced driving bunches or their combination with a witness bunch. If the study is restricted to one dimension, under the following assumptions, the system of equations can be reduced to a single second order ordinary differential equation [3, 5, 13, 34]. Since in PWFA the driving beam is initially ultrarelativistic, for a simplified model the bunch velocity can be taken equal to the speed of light, i.e. $\beta_b = 1$ and its shape considered as not altered during the propagation. Choosing z as the direction of propagation, if the bunch(es) can be considered rigid, i.e. do not significantly modify their shape during the propagation in the plasma, the source term n_b and thus all the physical quantities are function of only the comoving variable $t - z/c$. This approximation also allows to decompose the electron momentum equation in two momentum equations for the two electron species (those belonging to the beam and those belonging to the plasma background). Since the beam is considered rigid, only the electron momentum equation remains to be solved. In order to adimensionalize the resulting equations, all physical quantities can be rewritten in terms of the coordinate $\tau = \omega_p(t - z/c)$, where $\omega_p = \sqrt{\frac{n_0 e^2}{m_e \varepsilon_0}}$ is the electron plasma frequency. Combining Eqs.(3.1) under these hypotheses and defining the quantity $x = \gamma_e(1 - \beta_e)$ we obtain:

$$\frac{d^2 x(\tau)}{d\tau^2} = \frac{1}{2}\left(\frac{1}{x^2(\tau)} - 1 + 2\alpha(\tau)\right), \tag{3.2}$$

where the normalized beam density has been used:

$$\alpha(\tau) = \frac{n_\mathrm{b}(\tau)}{n_0}. \tag{3.3}$$

Once this nonlinear ordinary differential equation for x is integrated, the evolution of the other physical quantities can be derived using Eqs.(3.1):

$$n_e(\tau) = \frac{n_0}{1 - \beta_e(\tau)}, \tag{3.4}$$

where $\beta(\tau)$ can be derived inverting the definition of $x(\tau)$;

$$E(\tau) = -\frac{m_e \omega_p c}{e} \frac{dx(\tau)}{d\tau}, \tag{3.5}$$

from which the quantity x is inferred as proportional to the electrostatic potential. Convenient initial conditions to integrate Eq.(3.2) are $x(0) = 1$ and $x'(0) = 0$, corresponding to plasma electrons initially at rest and with zero acceleration.

This simple model derived with strong hypotheses can give an insight on the wake generation mechanisms, allowing to study the variations in the excited field obtained changing the driver shape, length and peak density. The model provided by Eq.(3.2) takes also into account the fluid nonlinearities in wake excitation. In the hypothesis $\alpha(\tau) \ll 1$, Eq.(3.2) expanded in series near the equilibrium point $x = 1$ up to the first order can be considered, obtaining the equation for small plasma oscillations at frequency ω_p:

$$\frac{d^2 x(\tau)}{d\tau^2} + x(\tau) = 1 + \alpha(\tau) \tag{3.6}$$

In this case the differential equation is linear, analytically solvable for arbitrary shapes of $\alpha(\tau)$, e.g. with the use of Laplace transform and Green's functions. Increasing $\alpha_{peak} = max(\alpha)$ with symmetric bunches shorter than the plasma wavelength $\lambda_p = 2\pi c/\omega_p$ - a frequent case of interest for PWFA - the transition from the linear regime to the weakly nonlinear regime, finally to the nonlinear regimes with $\alpha_{peak} \gg 1$. Only in the linear regime the solutions to Eq.(3.2) can be found for arbitrary driver shapes, while in weakly nonlinear and fully nonlinear regimes numerical integration is needed, because analytical solutions can be found only for very simple driver shapes, as in [34]. A standard 4th order Runge-Kutta explicit integration scheme is sufficient to integrate the model differential equation up to many plasma wavelength in a few seconds on a laptop computer. The discussed model can be used to study the dependence on driver shape of parameters involving longitudinal field magnitude, like the accelerating gradient and the Transformer Ratio [13]. Beam loading can also be studied, including the witness density in the source term $\alpha(\tau)$.

3.2 Plasma oscillations regimes

The parameter α_{peak}, by definition (Eq.(3.3)) quantifies the perturbation in the plasma density introduced by the bunch. Its relation to plasma oscillation regimes is shown in Figs. 3.1, 3.2, 3.3 and 3.4 (from [13]), where the results of the integration of Eq.(3.2) through a 4-th order Runge-Kutta scheme are reported, with a Gaussian driver as driving term, i.e. $\alpha(\tau) = \alpha\, e^{-\tau^2/2\sigma_\tau^2}$, $\sigma_\tau = 0.25$. In the linear regimes, i.e. $\alpha \ll 1$, both the electron density and the electric field in the driver wake are sinusoidal, with oscillation frequency ω_p, as shown in Fig. 3.1. In the weakly nonlinear regime, $\alpha \lesssim 1$, the electric field oscillations start to change towards a sawtooth shape (Figs. 3.2 and 3.3), until in the fully nonlinear regimes $\alpha \gg 1$ they have a full sawthooth form (Fig. 3.4). In the weakly nonlinear regime peaks of electron density start to appear, while in the fully nonlinear regime the electron density has a nearly constant value except for periodic impulsive peaks in correspondence of which the electric field changes sign.

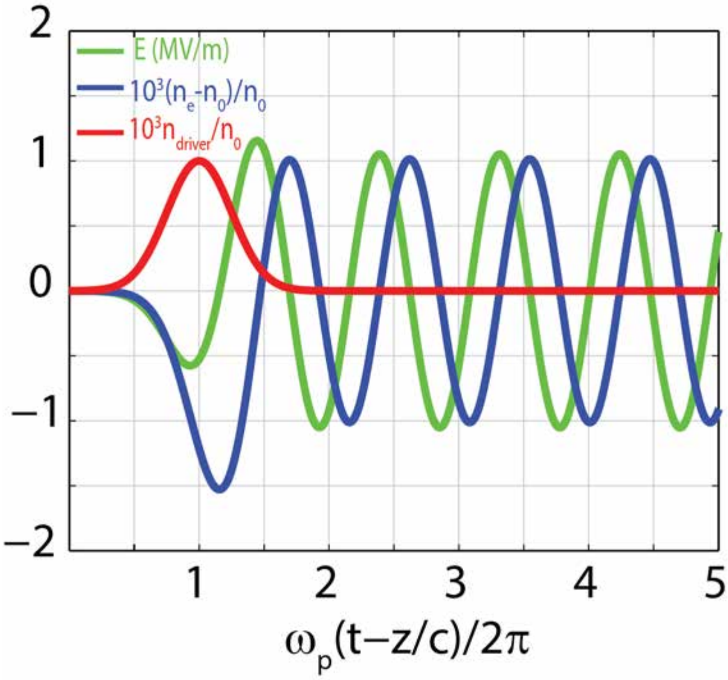

Figure 3.1: Linear regime of the oscillations, with $\alpha = 10^{-4}$. The red line represents the normalized bunch density profile n_b/n_0, the blue line represents the normalized background density perturbation from the equilibrium density $(n_e - n_0)/n_0$, the green line represents the Electric field E. Figure from [13].

The results in the fully nonlinear regime provide a qualitative, 1D representation of the bubble regime, in which the electron density is null in the bubble behind the driver and has high peaks between the bubbles. From Eq.(3.4) it can be inferred that in this fluid

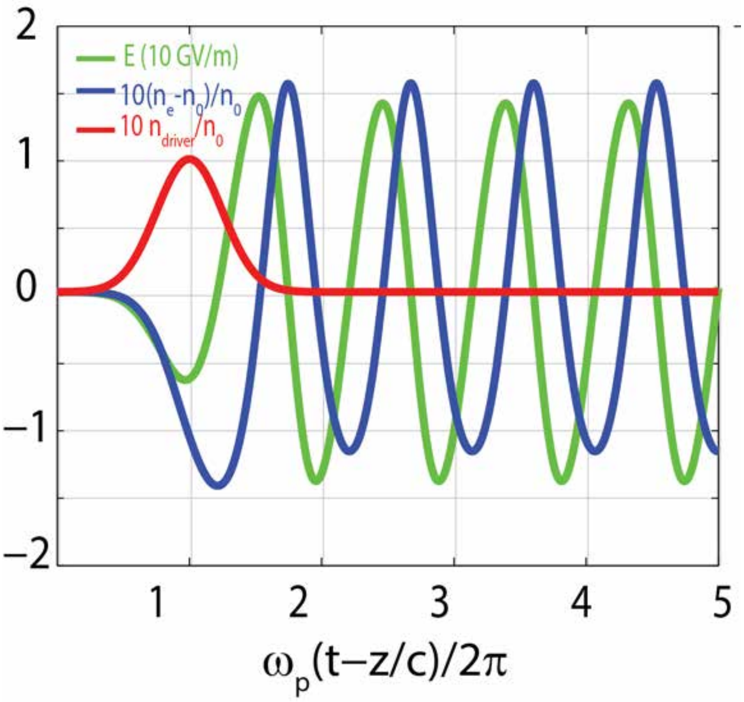

Figure 3.2: Transition to weakly nonlinear regime of the oscillations, with $\alpha = 10^{-1}$. The red line represents the normalized bunch density profile n_b/n_0, the blue line represents the normalized background density perturbation from the equilibrium density $(n_e - n_0)/n_0$, the green line represents the Electric field E. Figure from [13].

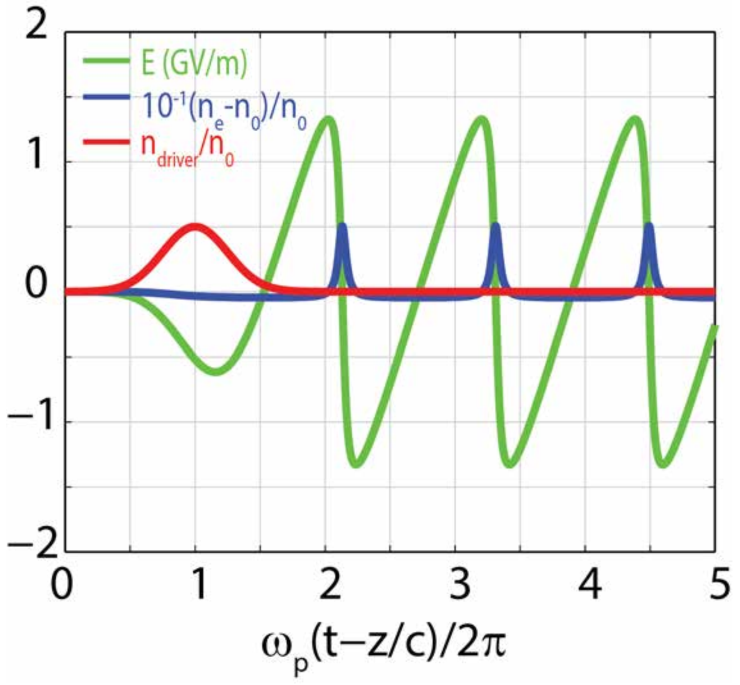

Figure 3.3: Weakly nonlinear regime oscillations, with $\alpha = 0.5$. The red line represents the normalized bunch density profile n_b/n_0, the blue line represents the normalized background density perturbation from the equilibrium density $(n_e - n_0)/n_0$, the green line represents the Electric field E. Figure from [13].

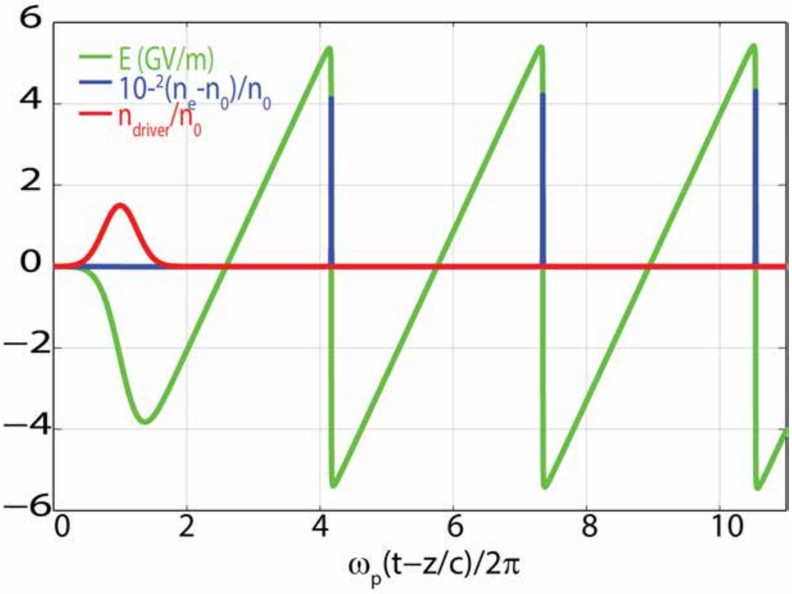

Figure 3.4: Nonlinear regime of the oscillations, with $\alpha = 1.5$. The red line represents the normalized bunch density profile n_b/n_0, the blue line represents the normalized background density perturbation from the equilibrium density $\left(n_e - n_0\right)/n_0$, the green line represents the Electric field E. Figure from [13].

1D model the lowest reachable electron density is $n_0/2$. With a kinetic model. e.g. a 1D Particle in Cell code, a full depletion of the plasma electrons in the bubble regions can be correctly predicted.

The transition from the linear regime can be analyzed also in the frequency domain. In the linear regime, the only frequency component is the one at $\omega_p/2\pi$. Increasing α, and thus the nonlinearity of the plasma response, two effects occur in the frequency domain. The first one is the appearance of higher harmonics, that progressively change the wave shape towards a sawtooth profile. In correspondence of the peaks in the plasma electron density, the plasma frequency has a temporary upshift, and the electric field changes sign abruptly. The second nonlinear effect is the lengthening of the wave period, thus the downshift of the principal harmonic from the value of ω_p, due to the increased inertia of the plasma relativistic electrons.

3.3 Cold wave breaking limit

A 1D cold fluid description allows to estimate the maximum sustainable field in a plasma for plasma acceleration. This maximum field is defined as the threshold value beyond which the fluid model loses its validity because the wave folds on itself. This phenomenon, called wave breaking, involves many plasma electrons with significantly different velocities interacting in small regions. Thus, when the wave is broken a kinetic description is required to correctly describe the new regime. In the nonrelativistic case the wave breaking mechanism can be seen directly from the nonlinear plasma fluid momentum equation, for simplicity in absence of external forces:

$$\frac{\partial v}{\partial t} = -v\frac{\partial v}{\partial x}. \tag{3.7}$$

The nonlinear term $-v\frac{\partial v}{\partial x}$ determines the local rate of change of velocity $\frac{\partial v}{\partial t}$. In Fig. 3.5 the sign of the local velocity derivative determines a progressive steepening of the wave can be inferred.

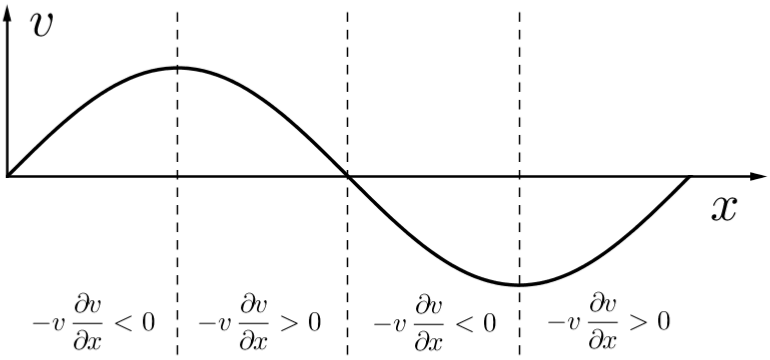

Figure 3.5: Sign of the nonlinear term in Eq.(3.7) in an initially sinusoidal velocity profile of a wave.

Equation (3.7) can intuitively be interpreted as a transport equation for the velocity, with advection velocity of a fluid element corresponding to the local velocity of the fluid itself. In this interpretation, fluid portions with higher velocities move within the wave envelope with a higher velocity than slower fluid elements. As the wave amplitude increases, the steepening becomes unstable as the wave crests tend to collapse on the wave itself as sketched in Fig. 3.6. Note that in plasma acceleration the relativistic form of the momentum $p = mc\beta(1-\beta^2)^{-1/2}$ adds an intrinsical nonlinearity in the fluid equations.

A condition for wave breaking can be obtained by observing that the fluid velocity value should be greater than the phase velocity of the wave so that the crests would surpass the wave envelope, and at some locations two different fluid velocities would exist, invalidating the fluid description. Physically the wave folding would generate turbulence, and the plasma wave would not be suitable for acceleration of particles in a

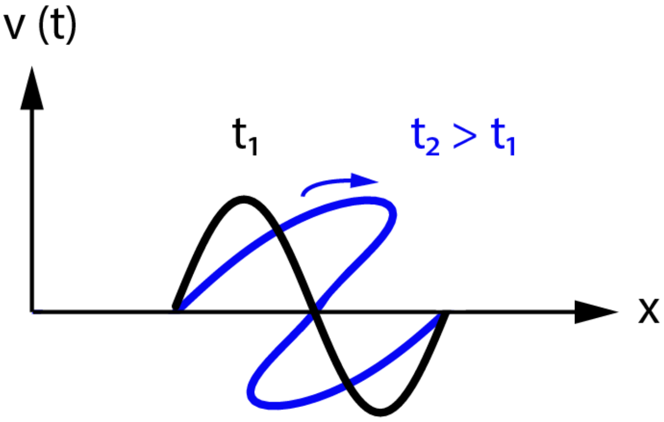

Figure 3.6: Envelope of the velocity during nonlinear wave propagation and wave breaking.

controllable way.

To roughly estimate the field at the wave breaking point the linearized form of the one dimensional momentum equation is considered in the nonrelativistic limit:

$$m_e \frac{\partial v}{\partial t} = -eE$$

With the ansatz of solutions in the harmonic form $\propto e^{i(k_p z - \omega_p t)}$, where $k_p = 2\pi/\lambda_p = \omega_p/v_{ph}$, Eq.(3.8) becomes:

$$-\, i\omega_p \, m_e v = -eE. \tag{3.8}$$

From Eq.(3.8) the value of the peak fluid velocity can be computed. Imposing the condition that its value does not exceed the wave phase velocity, which is equal to the driver (either laser or particle beam) velocity $v_{ph} = \beta_b c$, Eq.(3.8) yields

$$v = \left| \frac{eE}{m\omega_p} \right| \leq v_{ph}, \tag{3.9}$$

from which the cold weave breaking limit can be inferred:

$$|E| \leq \frac{m\omega_p v_{ph}}{e}. \tag{3.10}$$

With laser pulses and relativistic particle beams as drivers the phase velocity of the wave is assumed equal to c^1, yielding the estimate:

$$E_{WB} = \frac{m_e \omega_p c}{e} \approx 96\sqrt{n_0(cm^{-3})}. \tag{3.11}$$

The same estimate could have been performed considering the linearized divergence equation for E and imposing a complete electron depletion in the plasma:

$$\frac{\partial E}{\partial z} = \frac{e}{\varepsilon_0} n_0 \tag{3.12}$$

with the same ansatz of harmonic wave form.

Both derivations are inconsistent, primarily because they neglect the nonlinearity of wave breaking. This flaw is more evident in the second derivation since in the hypothesis of complete depletion from electrons, as in the bubble regime, the wave is highly nonlinear.

An estimate of the cold wave breaking limit which takes into account nonlinear relativistic effects starts from the model in Sec.3.1 [3, 5]. In the region behind the driver Eq.(3.2) reads

$$x''(\tau) - \frac{1}{2}\left(\frac{1}{x^2(\tau)} - 1\right) = 0, \tag{3.13}$$

which expresses the conservation of the quantity

$$\left(\frac{dx(\tau)}{d\tau}\right)^2 + \left(\frac{1}{x(\tau)} + x(\tau)\right). \tag{3.14}$$

From the definition of $x = \gamma(1-\beta)$ and the identity $1 + \beta^2\gamma^2 = \gamma^2$ it can be inferred that

$$\frac{1}{x} + x = 2\gamma, \tag{3.15}$$

Besides, when the derivative of x is zero the quantities associated to the plasma fluid velocity $c\beta$ has a minimum or a maximum and consequently the fluid relativistic factor γ has a maximum. Thus denoting the maximum value of γ during the oscillations with γ_m the quantity in Eq.(3.14) can be set to:

$$\left(\frac{dx(\tau)}{d\tau}\right)^2 + \left(\frac{1}{x(\tau)} + x(\tau)\right) = 2\gamma_m. \tag{3.16}$$

---

[1] In the case of laser pulses the wave velocity is corrected by the refraction index, thus the value c can be seen as an upper bound in the estimate of the wave breaking limit.

Using Eq.(3.5) and isolating the derivative of x from Eq.(3.16) the electric field can be found:

$$E(\tau) = \pm \frac{m\omega_p c}{e}\sqrt{2}\sqrt{\gamma_m - \gamma(\tau)}. \tag{3.17}$$

The sign indeterminacy comes from the fact that γ is function of the squared value of β. The Electric field maximum value is obtained in correspondence of $\gamma(\tau) = 1$ (fluid element at rest). Intuitively wave breaking occurs when the fluid velocity is greater than the wave phase velocity, equal to the driving beam velocity, thus the maximum sustainable electric field is found setting $\gamma_m = \gamma_b = (1 - \beta_b^2)^{1/2}$, obtaining the cold relativistic wave breaking limit:

$$E_{WB} = \frac{m\omega_p c}{e}\sqrt{2}\sqrt{\gamma_b - 1}. \tag{3.18}$$

The last passage is not fully consistent with the model, which assumes $\beta_b = 1$, thus an infinite relativistic factor γ_b. A fully consistent derivation of the wave breaking limit in Eq.(3.18) obtained maintaining a beam velocity smaller than c in the one dimensional form of Eqs.(3.1) can be found in [2, 4]. Wave breaking limits have been found also for warm plasmas, in the classical regimes [73] and in relativistic regimes [74, 75]. In [76] a unified 1D relativistic fluid model for arbitrary wave phase velocities and temperatures is presented, from which also the wave breaking limits in [4, 73–75] can be reproduced. Considering a wave phase velocity, which coincides with the bunch velocity $\beta_b c \neq 1$, in the relativistic cold fluid approximation the plasma electron density takes the form [4]

$$n_e = \frac{n_0}{1 - \frac{\beta}{\beta_b}}, \tag{3.19}$$

from which it can be seen that when the velocity of the fluid tends to the phase velocity of the wave, i.e. when $\beta \rightarrow \beta_b$, the density tends to infinity as it should be in wave breaking. In the simplified model derived in Section 3.1 this occurs when $\beta \rightarrow 1$ since it was assumed that $\beta_b = 1$.

3.4 Transformer Ratio

From an energy conservation point of view, the plasma channel acts as an energy transformer which converts the energy of a laser or particle beam in kinetic energy of the plasma electrons and in electromagnetic energy. Such electromagnetic energy of the plasma wave is converted in kinetic energy of the witness particles. This indirect energy exchange obviously involves efficiency challenges more relevant than conventional accelerators. The driver beam thus represents an energy supply for all the acceleration process. The ratio between the maximum energy gain for a test charge behind a driver particle beam and the driver energy can be estimated by the Transformer Ratio. Assuming that an electron driving beam (the same argument can be extended to beams of other particle species) with energy E_d is depleted of its energy by its own wakefield, the depletion L can be estimated as $L = E_d/eE_{dec}$, where E_{dec} is the maximum decelerating field amplitude in the beam (see Fig. 3.7). The distance L thus represents the effective

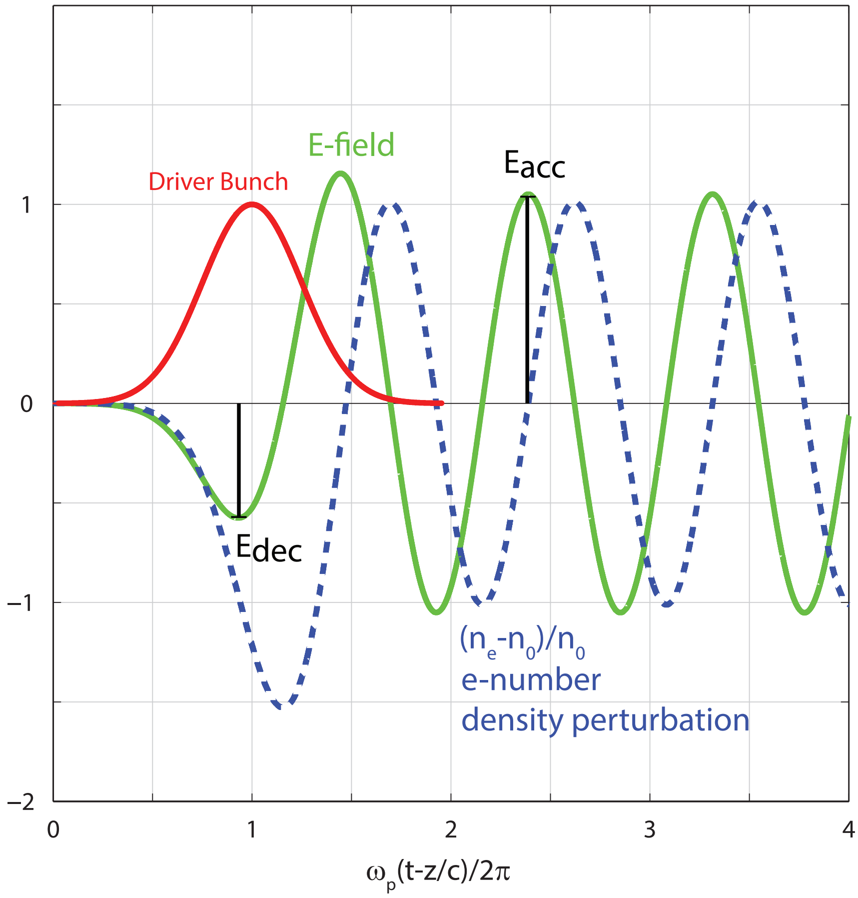

Figure 3.7: Fields involved in the definition of the Transformer Ratio in PWFA. The red line represents the normalized bunch density profile n_b/n_0, the blue line represents the normalized background density perturbation from the equilibrium density $(n_e - n_0)/n_0$, the green line represents the Electric field E. The black segments represent the maximum magnitude of the decelerating field inside the driver E_{dec} and the maximum magnitude of the accelerating field behind the driver E_{acc}. Adapted from [13].

distance along which the driver can provide energy to a test charge behind it. The maximum energy gain for a test charge e behind the driver can be estimated assuming to place it on the position with the maximum accelerating field behind the driver. Denoting the amplitude of this maximum accelerating field with E_{acc}, the maximum energy gain for the charge can be estimated as:

$$\Delta E = eE_{acc}L = \frac{E_{acc}}{E_{dec}}E_d = RE_d. \tag{3.20}$$

where the Transformer Ratio R (see Fig. 3.7) is defined:

$$R = \frac{E_{acc}}{E_{dec}}. \tag{3.21}$$

In a medium which can sustain only a monomodal electromagnetic oscillation, with a symmetric driver shape, a wakefield acceleration mechanism can have a maximum value of the Transformer Ratio equal to 2. This result was first proven in the case of conventional wakefield accelerators (see e.g. [77]), but it is valid also in the linear cold electrostatic regime of plasma acceleration, in which only the plasma frequency mode is sustained. In these hypotheses, to find the electric field in the linear regime, Eq.(3.6) can be considered. Introducing the variable $\tilde{x} = x - 1$, Eq.(3.6) can be written as a non-homogeneous harmonic oscillator differential equation:

$$\frac{d^2\tilde{x}(\tau)}{d\tau^2} + \tilde{x}(\tau) = \alpha(\tau). \tag{3.22}$$

With initial conditions corresponding to plasma initially at rest ($\tilde{x}(0) = 0$, $\frac{d\tilde{x}}{d\tau}|_{\tau=0} = 0$), the solution of Eq.(3.22) and the corresponding electric field are:

$$\begin{aligned} \tilde{x}(\tau) &= \int_{-\infty}^{\tau} \alpha(\tau')\sin(\tau - \tau')d\tau' \\ E(\tau) &= -\frac{m_e\omega_p c}{e}\frac{dx}{d\tau} = -\frac{m_e\omega_p c}{e}\frac{d\tilde{x}}{d\tau} = -\frac{m_e\omega_p c}{e}\int_{-\infty}^{\tau} \alpha(\tau')\cos(\tau - \tau')d\tau'. \end{aligned} \tag{3.23}$$

Following the same argument in [77], the limit of 2 for the Transformer Ratio in the linear regime can be proven from the second of Eqs.(3.23). Assuming a symmetric driver shape $\alpha(\tau)$, without loss of generality null except for the interval from $\tau = -T$ to $\tau = T$, the decelerating field within the driving bunch ($-T < \tau < T$) is

$$\begin{aligned} E(\tau) &= -\frac{m_e \omega_p c}{e} \int_{-T}^{\tau} \alpha(\tau') \cos(\tau - \tau') d\tau' = \\ &= -\frac{m_e \omega_p c}{e} \left[cos(\tau) \int_{-T}^{\tau} \alpha(\tau') \cos(\tau') d\tau' + sin(\tau) \int_{-T}^{\tau} \alpha(\tau') \sin(\tau') d\tau' \right]. \end{aligned} \tag{3.24}$$

The decelerating field at the center of the driver ($\tau = 0$) is

$$E(\tau) = -\frac{m_e \omega_p c}{e} \int_{-T}^{0} \alpha(\tau') \cos(\tau') d\tau' = E_{dec\,0}. \tag{3.25}$$

The field behind the driver ($\tau > T$) is

$$\begin{aligned} E(\tau) &= -\frac{m_e \omega_p c}{e} \int_{-T}^{T} \alpha(\tau') \cos(\tau - \tau') d\tau' = \\ &= -\frac{m_e \omega_p c}{e} \left[cos(\tau) \int_{-T}^{T} \alpha(\tau') \cos(\tau') d\tau' + sin(\tau) \int_{-T}^{T} \alpha(\tau') \sin(\tau') d\tau' \right]. \end{aligned} \tag{3.26}$$

Since the bunch shape $\alpha(\tau)$ is assumed symmetric, the second integral vanishes, thus the maximum accelerating electric field behind the driver is

$$E_{acc} = -\frac{m_e \omega_p c}{e} \int_{-T}^{T} \alpha(\tau') \cos(\tau') d\tau' = 2E_{dec\,0}. \tag{3.27}$$

If the maximum amplitude of the decelerating field is at the center of the driver, then $E_{dec\,0} = E_{dec}$ and the Transformer Ratio is $R = E_{acc}/E_{dec} = 2$. From Eq.(3.24), if the maximum decelerating field is not at $\tau = 0$, then $|E_{dec}| > |E_{dec\,0}|$ and $R = E_{acc}/E_{dec} < 2$, proving the limit of 2 for the Transformer Ratio in linear regimes with symmetric bunches. Given a driver shape $\alpha(\tau)$, Eq.(3.2) can be integrated and from Eq.(3.5) the electric field and consequently the Transformer Ratio can be computed. In Fig. 3.8 four different driver shapes are reported. The parameter σ and α in the Figure are respectively the half driver length (or the standard deviation for the Gaussian) and the peak driver density over the background density. Fig. 3.9 shows the Transformer Ratio of the symmeric driver shapes in the linear regime computed setting $\alpha = 10^{-4}$ and varying the bunch length. The proven limit of 2 in these conditions (linear regime and symmetric driver) can be inferred. The limit for the Transformer Ratio can be overcome using asymmetric drivers, e.g. a ramped bunch. In Fig. 3.10 the Transformer Ratio of a ramped bunch in the linear regime is shown.

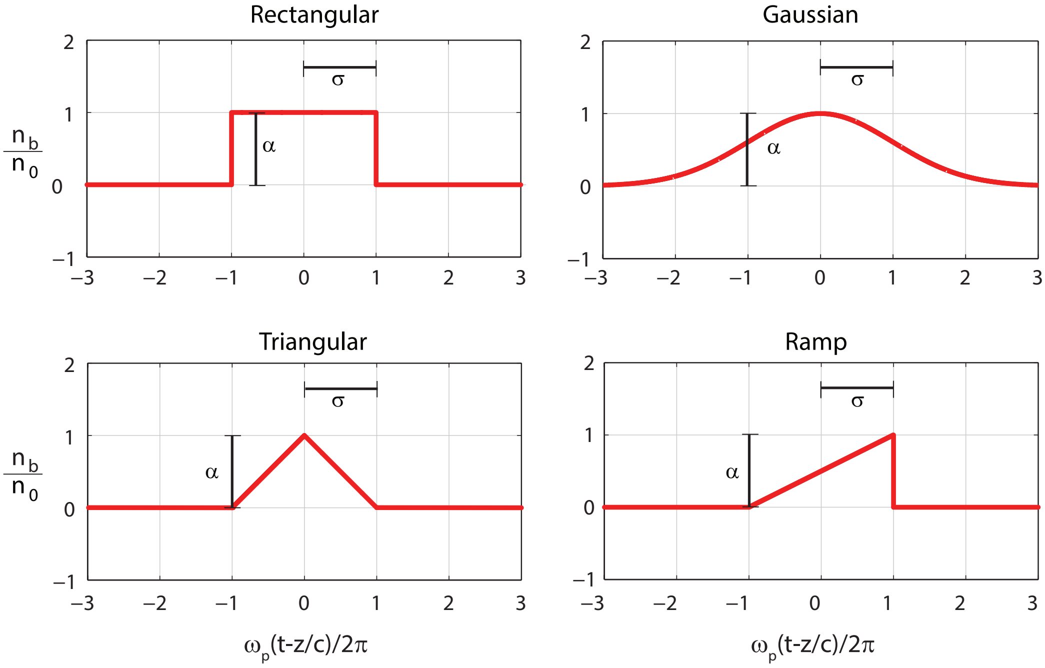

Figure 3.8: Driver bunch shapes used in the integration of Eq.(3.2) to compute te results in Figs. 3.9,3.10. Figure from [13].

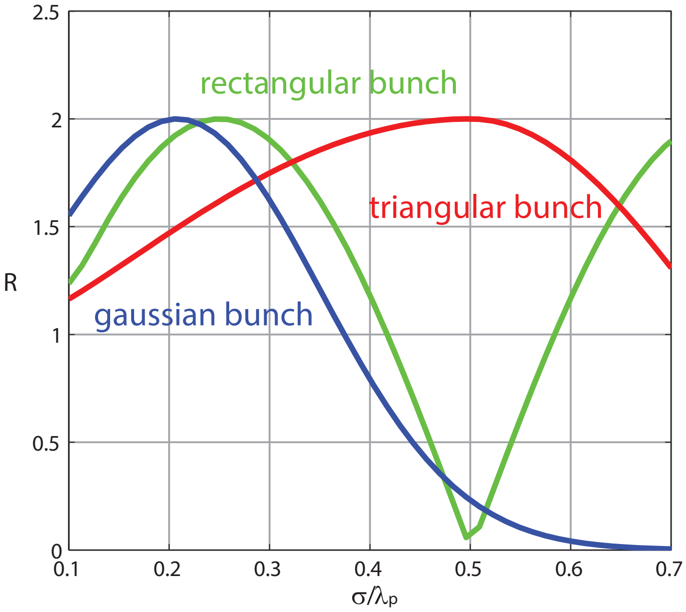

Figure 3.9: Transformer Ratio R of symetric driver bunches in linear regime ($\alpha = 10^{-4}$). Figure from [13].

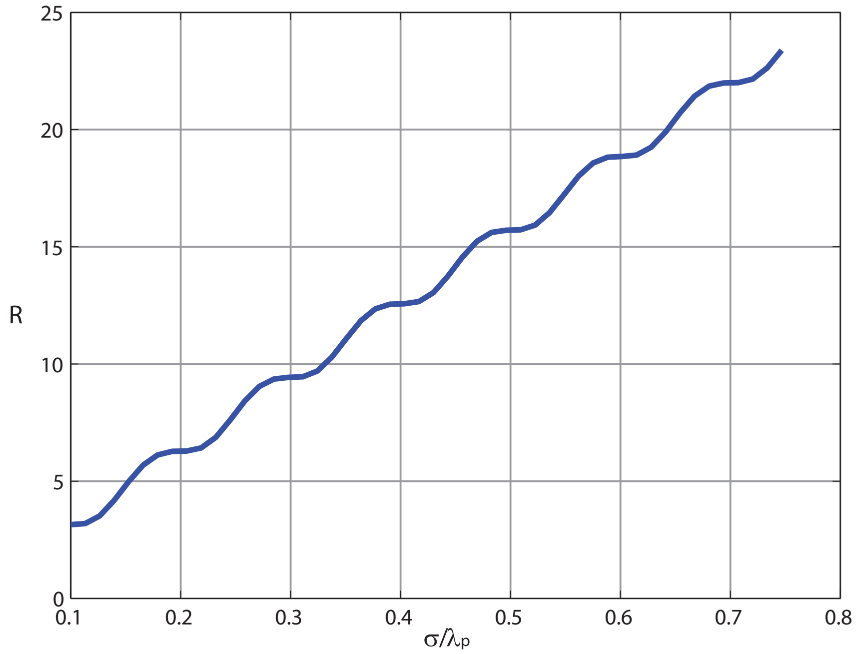

Figure 3.10: Transformer Ratio R of a ramped-profile driver bunch in linear regime ($\alpha = 10^{-4}$). Figure from [13].

Also in this regime Transformer ratios greater than 2 can be obtained with a long ramp. From an experimental point of view a tunable ramped bunch train is difficult to produce, thus to obtain high values of the Transformer Ratio it is more easy to use a train of driver bunches with a ramped envelope [19, 21], already proposed for conventional wakefield acceleration techniques [78, 79]. To overcome the Transformer Ratio limit with symmetric driver bunches the working regime must not be linear. In principle, with the model discussed in this Chapter, quick parametric studies on the best driver shapes for a high Transformer Ratio can be performed. In Fig. 3.11 Transformer Ratio maps for the driver shapes in Fig. 3.8 are reported, obtained varying the bunch length through the parameter σ and the nonlinearity parameter α. From these maps it can be inferred that the best strategy to obtain a high Transformer Ratio is to use a long ramp profile in the linear regime. Some considerations can be done on the Transformer Ratio. From its definition, it expresses the maximum energy gain for a single charge behind the driver, but the overall energy gain of a witness bunch will be less than that ideal value. Besides, driver configurations optimized with respect of the Transformer Ratio are not necessarily optimized with respect of the accelerating gradient [21]. With plasma channel lengths which are much smaller than the depletion length, to obtain high energy gains it is not convenient to reach a high Transformer Ratio, instead it is more

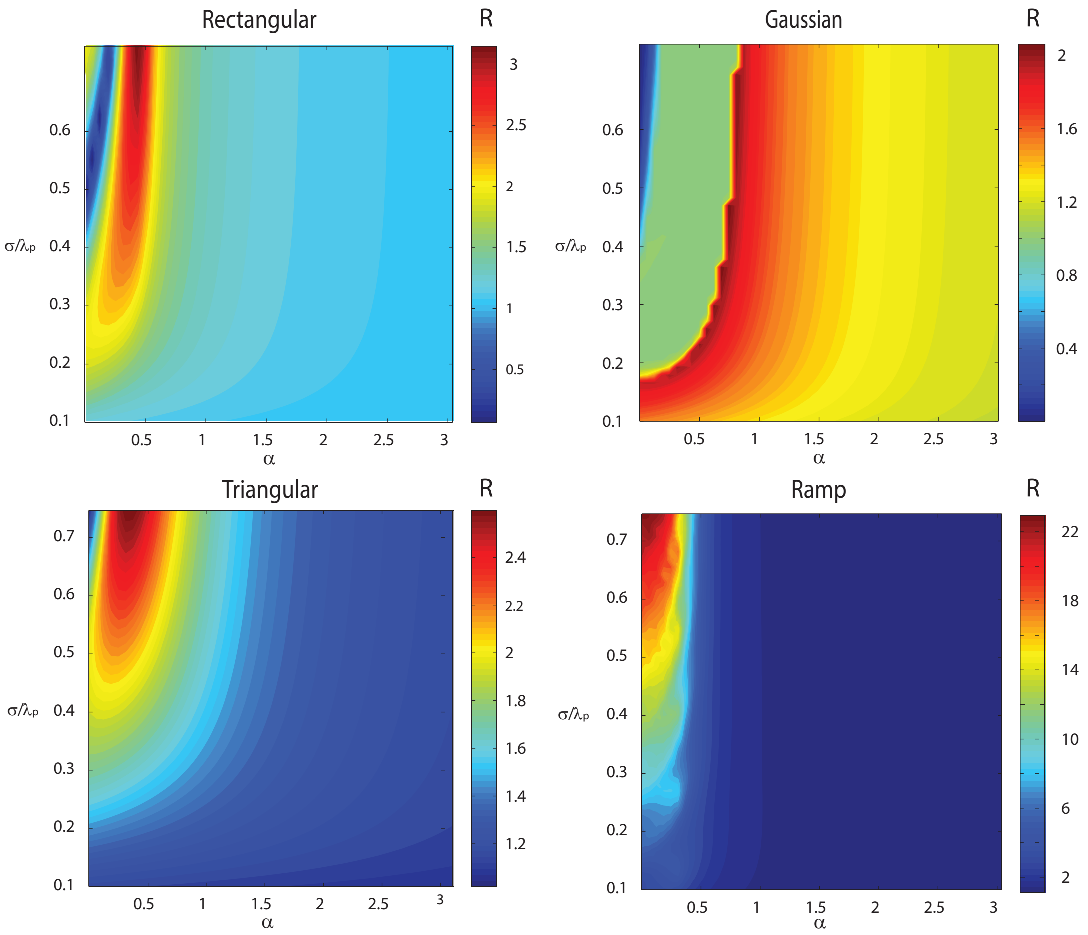

Figure 3.11: Transformer Ratio parametric maps for the driver shapes in Fig. 3.8. Figure from [13].

convenient to enhance the accelerating gradients. Finally, all the results concerning good driver shapes (i.e. form, length, peak density) with respect of the Transformer Ratio have been inferred from a 1D model with rigid bunch approximations. Even in 1D cases, the fully self-consistent bunch-plasma interaction (which can be studied e.g. with a Particle in Cell code) can reveal the side-effects of using certain driver shapes. For instance, the use of a long ramped bunch would likely lead to instabilities which would significantly change the driver shape during the propagation, invalidating the effectiveness of that particular configuration. Increasing the dimensions involved in the study, the electric field and thus the Transformer Ratio cannot be computed in arbitrary cases, and its values can be significantly different than in the 1D case. For these reasons the Transformer Ratio should be regarded only as a qualitative parameter concerning the efficiency of the energy transfer of a PWFA configuration, which neglect also the overall quality of the accelerated bunch (e.g. energy spread, emittance).

Chapter 4

Kinetic simulation of PWFA

The brief review of plasma acceleration models is completed in this Chapter, with the description of the kinetic simulation technique Particle in Cell (PIC). The results of 1D PIC simulations of plasma wakefield excitation are compared to numerical solutions of the 1D model presented in the previous Chapter. Such simple benchmark allows to discuss the comparison between kinetic and fluid PWFA simulations in different regimes of interest.

4.1 Particle in Cell simulation method

Since the first works on plasma simulations [80] it was clear that the details of the motion of all the particles of a real laboratory plasma are too many to be computed (this is true also now, with the contemporary supercomputing resources) and not all of them are necessary to catch the principal physical mechanisms. Fluid models and the derived fluid numerical codes constitute a powerful synthesis of the macroscopic plasma behavior, reducing the level of detail in the computation. However, in many studies of plasma physics, including the ones concerning plasma acceleration, a fluid description (and thus a fluid numerical code) may be unsuited to accurately study all the phenomena involved, requiring the use of a kinetic description. In the fluid description the system is reduced to a continuum, where the different velocities of particles in the same fluid element play no role. In the kinetic framework, the plasma modeling takes into account the velocity distribution of the particles composing the system.

The collective behavior is the most important feature exhibited by plasma particles which governs the physical mechanisms of plasma acceleration. As discussed in Appendix A, plasma collective behavior appears if the plasma extension is much greater than the Debye length λ_D, if the system is observed for time scales larger than ω_p^{-1} and if the number of particles in a Debye volume is high enough to have a coupling parameter (defined in Appendix A) $\Lambda \gg 1$. The tracking of a realistic number of particles which compose real plasmas in such space and time scales has been proved not to be necessary to reproduce plasma collective behavior in a kinetic framework. Among the kinetic techniques devised to simulate collective plasma behavior without computing the trajectory and the fields of a realistic number of particles, the Particle in Cell [35–37, 81] up to now is the most widely used. In this method the plasma is treated as an ensemble of finite-size computational particles. The computational particles provide a sampling of the distribution function of the whole sytem. Such particles move in a continuous phase space and their charge and current densities are wheighted on an Eulerian grid at every time iteration. The fields are then computed from Maxwell equations on the grid starting from the interpolated sources and finally the force on every particle is extrapolated from the grid, allowing to advance in time their positions and momenta in a Lagrangian way for the next iteration. This sequence of operations is repeated at each time step (see Fig. 4.1), self-costistently evolving the particles and the electromagnetic field states.

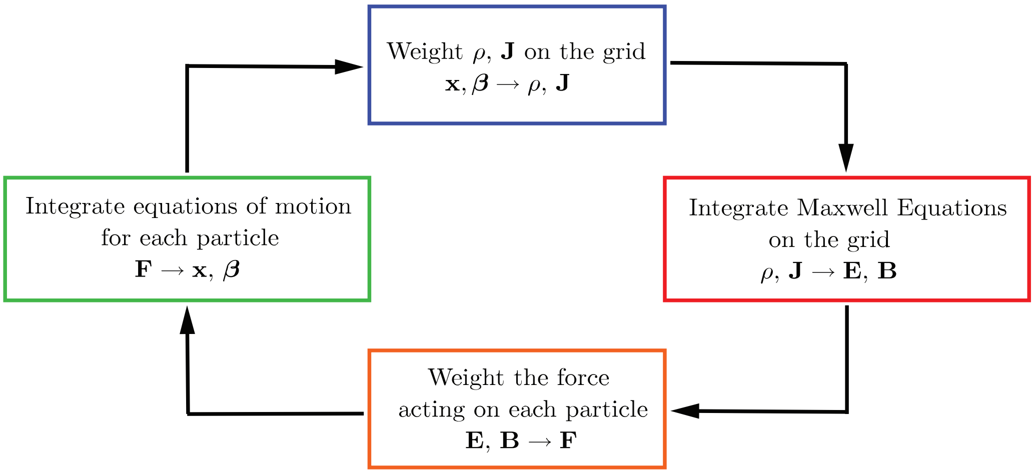

Figure 4.1: Time advancement in the Particle in Cell method.

In a strongly coupled system the noisy peaks in the trajectories of the particles are caused by the singularities of the forces between two particles. Since in a weakly coupled system these singularities are shielded by the presence of many particles in a Debye cube, collective behavior prevails on binary couplings. The same collective behavior typical of plasmas is reproduced in the PIC method using computational particles which create a Coulombian field in the region far from their position and a decreasing field in the region near their position, as shown in Fig. 4.2. Physically this kind of field is created by a finite size charge distribution, thus each computational particle in the PIC method represents a finite-size ensemble of physical particles with similar position and momentum. For this reason the computational particles are often called macroparticles.

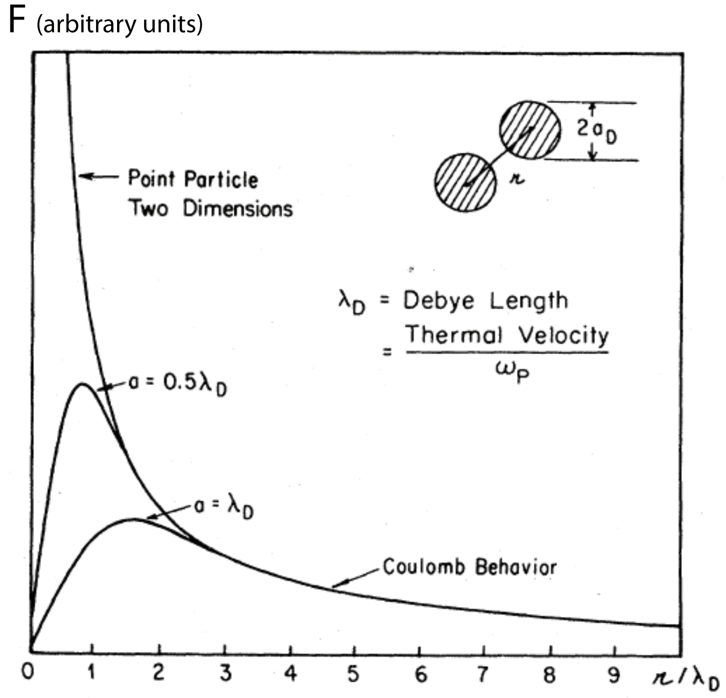

Figure 4.2: Force law F between finite-size particles in two dimensions for various sized particles. A Gaussian-shaped density profile was used. Adapted from [81].

In the next Sections 4.1.1, 4.1.2, 4.1.3, 4.1.4, the derivation and some details of the different steps of the method shown in the boxes of Fig. 4.1 are reviewed, following mainly [35, 37], where a more exhaustive discussion of the PIC method can be found.

4.1.1 Macroparticle equations of motion

A macroparticle in a PIC can be seen as a small portion of the phase space distribution of the system. Usually this portion has a Dirac delta extension in the momentum space, i.e.

$\delta(\boldsymbol{p}-\boldsymbol{p}_p(t))$, where $\boldsymbol{p}_p(t)$ is the momentum of the macroparticle. Such choice is physically consistent with the representation of many particles in a constant sized macroparticle, since particles with the same momentum tend to remain close in the phase space. On the contrary the macroparticle size in the position space is finite. The macroparticle charge is distributed on the grid by means of shape functions with compact support, usually in the form of spline functions $b_l\left(\frac{\boldsymbol{x}-\boldsymbol{x}_p(t)}{\Delta x_p}\right)$, where l is the order of the shape function, Δx_p is the width of the macroparticle shape and $\boldsymbol{x}_p(t)$ is the position of the macroparticle. Such shape functions represent the numerical charge density shape of the macroparticle. In Fig. 4.3 three spline functions in one dimension are represented. High order spline functions can be obtained through subsequent convolutions with the zeroth-order spline. Increasing the order of the shape functions smooths the numerical fluctuations in the charge and current densities associated with the sharp boundaries of the particles but requires more computational time to interpolate the macroparticle density on the grid. The distribution function of a macroparticle p of the species s can thus be written as:

$$f_{p,s}(\boldsymbol{x},\boldsymbol{p},t) = N_p b_l\left(\frac{\boldsymbol{x}-\boldsymbol{x}_p(t)}{\Delta x_p}\right)\delta(\boldsymbol{p}-\boldsymbol{p}_p(t)). \tag{4.1}$$

Normalizing the integral of b_l to unity, the integral over the momentum and position space of $f_{p,s}$ yields the number of particles N_p represented by the macroparticle p, which belongs to the species s. The distribution function of the whole system is thus represented by the sum of the distribution functions of each macroparticle, summing then the distribution functions of each species:

$$f(\boldsymbol{x},\boldsymbol{p},t) = \sum_{p,s} f_{p,s}(\boldsymbol{x},\boldsymbol{p},t). \tag{4.2}$$

When the electromagnetic forces $\boldsymbol{F}$ are given, as in the particle advancement of the PIC method, Vlasov equation is linear with respect of f. Thus, if the single macroparticle distribution functions $f_{p,s}$ satisfies Vlasov equation, i.e.

$$\frac{\partial f_{p,s}}{\partial t} + c\boldsymbol{\beta}\cdot\nabla_{\boldsymbol{x}} f_{p,s} + \boldsymbol{F}\cdot\nabla_{\boldsymbol{p}} f_{p,s} = 0, \tag{4.3}$$

then the sum of the macroparticles distribution functions, i.e. the whole system distribution function (Eq.(4.2)) also satisfies Vlasov equation. The nonlinearity of Vlasov equation is hidden in the dependence of $\boldsymbol{F}$ on the total distribution function f.

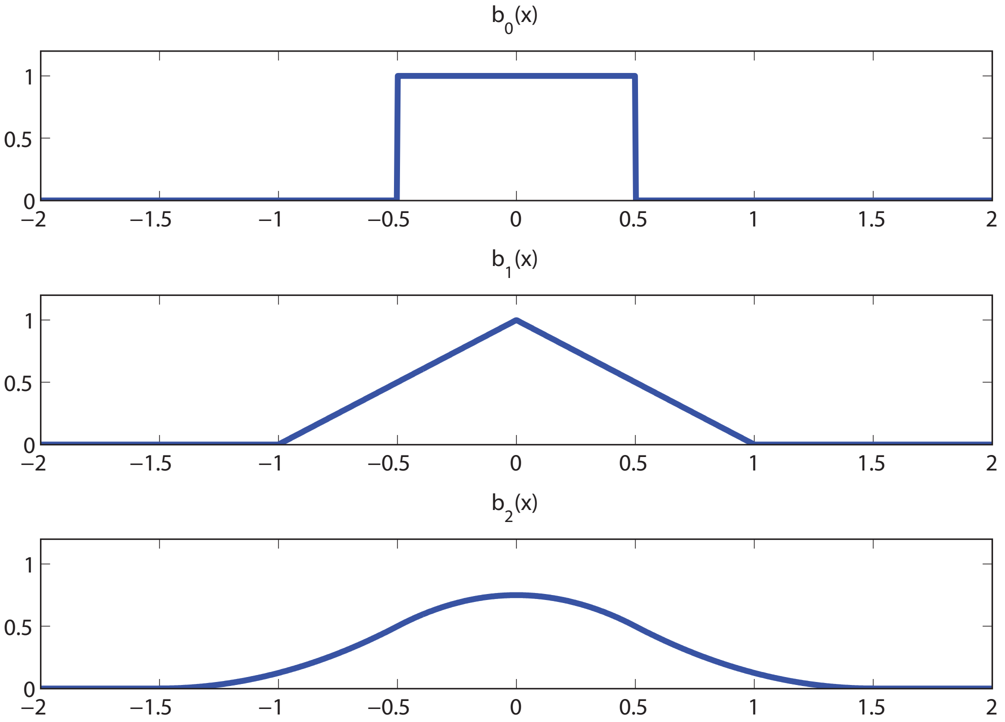

Figure 4.3: Spline functions in one dimension, $\Delta x_p = 1$.

The conservation of the number of particles in each macroparticle and its equations of motion can be derived from Eq.(4.3). Indeed, in principle N_p in Eq.(4.1) may vary with time, but with the hypothesis on $f_{p,s}$ given by Eq.(4.3) its value remains constant. Integrating Eq.(4.3) over the position and momentum space, the conservation of the number of particles in a macroparticle is obtained:

$$\begin{aligned}\int\int\left[\frac{\partial f_{p,s}}{\partial t} + c\boldsymbol{\beta}\cdot\nabla_{\boldsymbol{x}} f_{p,s} + \boldsymbol{F}\cdot\nabla_{\boldsymbol{p}} f_{p,s}\right] d^3x\, d^3p &= \\ = \frac{d\left(\int\int f_{p,s} d^3x\, d^3p\right)}{dt} &= \\ = \frac{dN_p}{dt} &= 0,\end{aligned} \tag{4.4}$$

where the vanishing of the distribution function at infinite values of position and momentum has been used to cancel the last two integrals of the first equation.

Multiplication of Eq.(4.3) by the vector $\boldsymbol{x}$ and integration over the position and momentum space gives

$$\int\int \boldsymbol{x}\left[\frac{\partial f_{p,s}}{\partial t} + c\boldsymbol{\beta}\cdot\nabla_{\boldsymbol{x}} f_{p,s} + \boldsymbol{F}\cdot\nabla_{\boldsymbol{p}} f_{p,s}\right] d^3x\, d^3p = 0 \tag{4.5}$$

The vanishing of $f_{p,s}$ at infinite values of momentum nullifies the last integral, yielding

$$\frac{d\left(\int\int \boldsymbol{x} f_{p,s} d^3x\, d^3p\right)}{dt} = \int \left[c\boldsymbol{\beta} \cdot \int \nabla_{\boldsymbol{x}} f_{p,s} \otimes \boldsymbol{x} d^3x\right] d^3p = \int\int c\boldsymbol{\beta} f_{p,s} d^3x\, d^3p. \tag{4.6}$$

The second integral has been evaluated by integration by parts, using the vanising of $f_{p,s}$ at infinite values of momentum[1]. With the definition of $f_{p,s}$ expressed in Eq.(4.1), the first and the final integral of Eq.(4.9) represent respectively the position $\boldsymbol{x}_p$ and the velocity of the macroparticle $c\boldsymbol{\beta}_p$, both multiplied by N_p. The first equation of motion of the macroparticle p is thus derived:

$$\frac{d\boldsymbol{x}_p}{dt} = c\boldsymbol{\beta}_p. \tag{4.7}$$

The second equation of motion for the macroparticle p is derived multiplying Eq.(4.3) by the vector $\boldsymbol{p}$ and integrating over the position and momentum space:

$$\int\int \boldsymbol{p}\left[\frac{\partial f_{p,s}}{\partial t} + c\boldsymbol{\beta} \cdot \nabla_{\boldsymbol{x}} f_{p,s} + \boldsymbol{F} \cdot \nabla_{\boldsymbol{p}} f_{p,s}\right] d^3x\, d^3p = 0. \tag{4.8}$$

The vanishing of $f_{p,s}$ at infinite values of position nullifies the second integral, yielding

$$\frac{d\left(\int\int \boldsymbol{p} f_{p,s} d^3x\, d^3p\right)}{dt} = \int \left[\boldsymbol{F} \cdot \int \nabla_{\boldsymbol{p}} f_{p,s} \otimes \boldsymbol{p} d^3x\right] d^3p = \int\int \boldsymbol{F} f_{p,s} d^3x\, d^3p. \tag{4.9}$$

The last equality has been obtained similarly as the second equality in Eq.(4.9). Dividing by N_p, the second equation of motion for the macroparticle p takes the form

$$\frac{d\boldsymbol{p}_p}{dt} = \boldsymbol{F}_p. \tag{4.10}$$

Thus, instead of solving directly Vlasov equation for the whole system or integrating the equations of motion of all the physical particles, the PIC method integrates $2N_m$ equations of motions, where N_m is the number of simulated macroparticles, given by Eqs.(4.7, 4.10). With the sampling of the distribution function f by the macroparticles involved in the PIC method, such equations constitute the characteristic curves equations of Vlasov equation. Any scheme used to integrate equations of motion can thus be used to integrate them (once the force acting on every macroparticle $\boldsymbol{F}_p$ is computed). A

---

[1] the identity $(\nabla_{\boldsymbol{x}} f_{p,s} \otimes \boldsymbol{x})_{i,j} = \delta_{i,j} x_i \frac{df_{p,s}}{dx_j}$, with $x_1 = x$, $x_2 = y$, $x_3 = z$ can be used for the calculation of the tensorial operations involved in cartesian coordinates. The final result in the last equality of Eq.(4.9) is the same in other coordinate systems.

second order scheme widely used for such purpose is the leap-frog scheme, with Boris method to perform the rotation of the macroparticle momentum vector by the magnetic field [35, 82] (recalled in Appendix B).

4.1.2 Weighting of the force on each macroparticle from the grid

The term $\boldsymbol{F}_p = \int\int \boldsymbol{F} f_s d^3x\, d^3p$ defines the force acting on the macroparticle. It can be seen as a convolution of the macroparticle distribution function (sampled at momentum $\boldsymbol{p}_p$ by the integration on the delta function in momentum) with the shape function b_l:

$$\boldsymbol{F}_p = \int\int \boldsymbol{F} f_{p,s} d^3x\, d^3p = \int b_l\left(\frac{\boldsymbol{x} - \boldsymbol{x}_p(t)}{\Delta x_p}\right) \boldsymbol{F}_{p,s}(\boldsymbol{x}, \boldsymbol{p}_p, t) d^3x. \tag{4.11}$$

The force on the macroparticle p of the species s can be computed from the electromagnetic fields:

$$\boldsymbol{F}_{p,s}(\boldsymbol{x}, \boldsymbol{p}_p, t) = q_s \left[\boldsymbol{E}(\boldsymbol{x}, t) + \frac{\boldsymbol{p}_p}{m_s \gamma_p c} \times \boldsymbol{B}(\boldsymbol{x}, t)\right], \tag{4.12}$$

where q_s and m_s are respectively the charge and the mass of a particle of species s. In a PIC code, the space is discretized on a grid. The fields are constant in each mesh cell. Denoting the k mesh cell region with $M_k = [\boldsymbol{x}_k, \boldsymbol{x}_k + \Delta\boldsymbol{x}]$, where the components of $\Delta\boldsymbol{x}$ are the mesh cell boundary length, Eq.(4.12) is reduced to the sum of the fields on a grid sampled by the shape functions:

$$\boldsymbol{F}_p(t) = \sum_k \int_{M_k} b_l\left(\frac{\boldsymbol{x} - \boldsymbol{x}_p(t)}{\Delta x_p}\right) q_s \left[\boldsymbol{E}(\boldsymbol{x}, t) + \frac{\boldsymbol{p}_p(t)}{m_s \gamma_p(t)} \times \boldsymbol{B}(\boldsymbol{x}, t)\right] d^3x. \tag{4.13}$$

Since the spline function b_l has compact support, the integrals not adjacent to the macroparticle vanish. In the PIC loop (Fig. 4.1) the weighting of the force from the grid consists in finding the location of the macroparticle in the grid and sum the convolution integrals of the fields with the spline functions on the cells adjacents to the macroparticle.

4.1.3 Integration of the electromagnetic fields

The fields $\boldsymbol{E}$ and $\boldsymbol{B}$ on the grid can be integrated from Maxwell Equations. The diversity of numerical methods concerning this step is vast as the literature describing it, ranging from explicit to implicit methods, time and frequency methods, finite difference, finite element or finite volume methods and many others (See e.g. [83]). One of the most used methods in an electromagnetic problem is the Finite Difference Time Domain (FDTD) method [84], reviewed briefly in Appendix B.

4.1.4 Weighting of charge and current densities on the grid

The sources of Maxwell Equations in the PIC scheme are the charge and current densities of the macroparticles, weighted on the grid with shape functions. The use of the same shape functions for both the force weighting and the charge deposition on the grid avoids the appearance of self forces of the macroparticles on themselves and conserves the momentum of the system [35]. In particular, using the same spline functions, the charge and current densities on the mesh cell k are computed as the sum of the spline functions centered on the macroparticles' positions.

$$\begin{aligned}\rho(\boldsymbol{x},t) &= \sum_p \int q_s f_s(\boldsymbol{x},\boldsymbol{p},t) d^3p = \sum_p q_s N_p b_l \left(\frac{\boldsymbol{x}-\boldsymbol{x}_p(t)}{\Delta x_p}\right) \\ \boldsymbol{J}(\boldsymbol{x},t) &= \sum_p \int q_s \boldsymbol{\beta}_p(t)\, c\, f_s(\boldsymbol{x},\boldsymbol{p},t) d^3p = \sum_p q_s N_p\, \boldsymbol{\beta}_p(t)\, c\, b_l \left(\frac{\boldsymbol{x}-\boldsymbol{x}_p(t)}{\Delta x_p}\right)\end{aligned} \tag{4.14}$$

To compute the charge and current densities in the mesh cell k, their mean value in the volume of the cell $V_k = \int_{M_k} d^3\boldsymbol{x}$ is computed:

$$\begin{aligned}\rho_k(t) &= \frac{1}{V_k}\int_{M_k} \rho(\boldsymbol{x},t) d^3x \\ \boldsymbol{J}_k(t) &= \frac{1}{V_k}\int_{M_k} \boldsymbol{J}(\boldsymbol{x},t) d^3x.\end{aligned} \tag{4.15}$$

As in the force weigthing from the grid, the integrals of the spline functions are null except for those computed in the cells adjacents to the macroparticles' positions on the grid. As hinted before, since the previous integrals reduce to the sum of integrals of the shape functions on the grid, high order spline functions reduce the numerical noise in the charge and current density and the extrapolated force, but requires more computational time to compute more complex integrals of the shape functions.

4.2 Fluid model vs PIC model

Kinetic models as the one used by the PIC method can fully take into account the interaction of differences in particle velocities. Besides, the fluid averaging of quantities over the particles' momenta loses predictivity when the number of particles in a region of space approaches zero. Fluid models thus cannot correctly reproduce purely kinetic effects, e.g. Landau damping [52, 85] and regimes in which the number of particles in a region of space is zero, e.g. the blowout regime. For these reasons and the fact that beam quality (e.g. in terms of emittance, energy spread) is defined through kinetic models, plasma acceleration studies usually employ PIC codes. The accuracy of PIC methods makes them slow with respect of fluid models with the same numbers of dimensions.

Although the fluid model discussed in Chapter 3 has been derived from strong assumptions, it helps to qualitatively study the basic mechanisms involved in wakefield excitation in PWFA. One advantage of this fluid model is its velocity: the integration of its equations with standard methods on a single core machine requires negligible time with respect of a 1D PIC code, which still requires time of the order of hours on a single core machine to perform simulations with the same driver parameters.

The validity of the 1D rigid fluid model discussed in Chapter 3 can be extended up to weakly nonlinear regimes including in Eq.(3.2) a phenomenological damping term [86]. Formally, the model is derived from Eq.(3.1) and the bunch rigidity assumption, thus no damping can be derived. The inclusion of the damping is only phenomenological, to account for kinetic damping effects. The modified model reads:

$$\frac{d^2x(\tau)}{d\tau^2} = \frac{1}{2}\left(\frac{1}{x^2(\tau)} - 1 - b\frac{dx(\tau)}{d\tau} + 2\alpha(\tau)\right), \tag{4.16}$$

where the damping coefficient b is finely tuned to qualitatively reproduce the PIC results. In Figs. 4.4, 4.5, 4.6 and 4.7 (from [86]) the comparison between the 1D rigid fluid model and the 1D PIC code PHIC by A. Macchi and A. Marocchino, using electron square bunches with $\sigma = 0.25\lambda_p$ as drivers. In the linear regime (Figs. 4.4, 4.5) no damping term is necessary, and the rigid fluid model results correctly reproduce the PIC results. Increasing the nonlinearity parameter α (the peak driver density over the background initial density) the two models start to diverge, and the damping term is necessary to extend the validity of the pure fluid model. Tuning the value of the damping coefficient to $b = 0.11$ a good qualitative agreement with the PIC is obtained up to the weakly nonlinear regime (Fig. 4.6). In the nonlinear regime (Fig. 4.7) the damped fluid model qualitatively reproduces the kinetic results for the first two oscillation cycles.

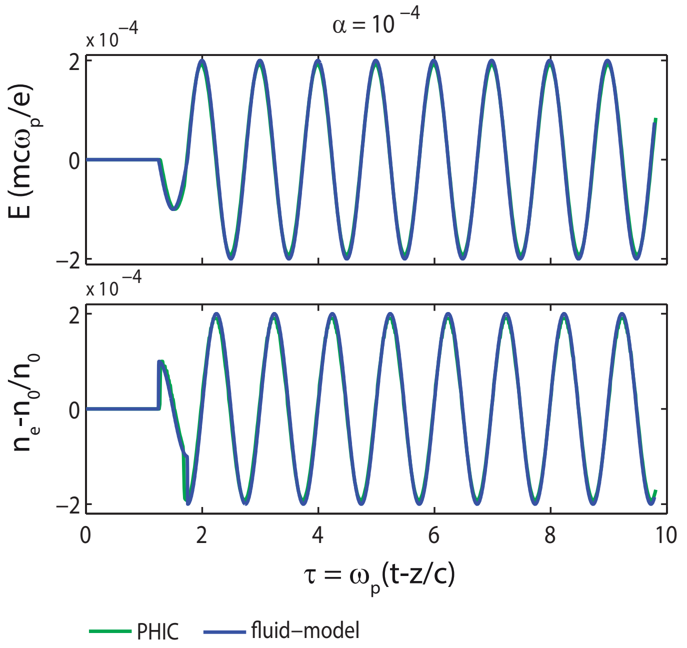

Figure 4.4: Comparison between the 1D rigid fluid model and 1D PIC, square bunches with $\sigma = 0.25\lambda_p$, $\alpha = 10^{-4}$. Top panel: electric field E; bottom panel: normalized perturbation of the background electron density from the equilibrium $(n_e - n_0)/n_0$. Green line: PHIC code simulation results; blue line: same physical quantities, computed through the fluid model. Image from [86].

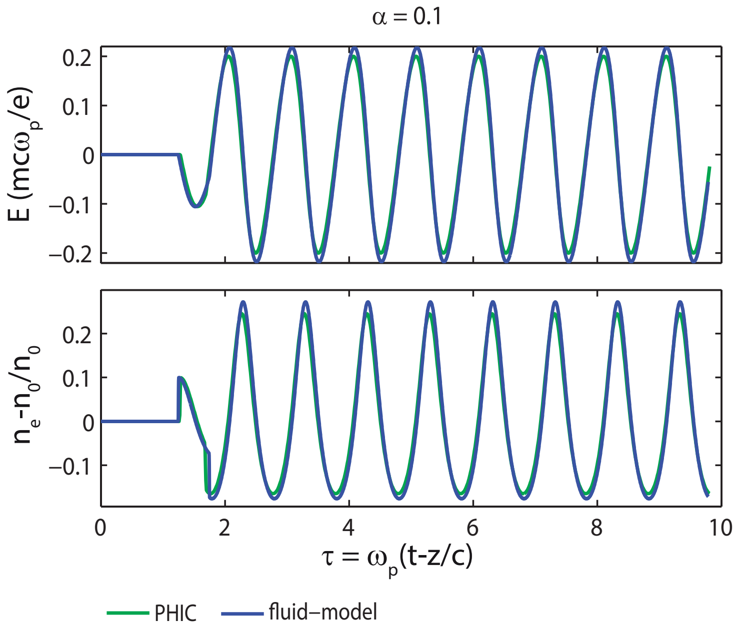

Figure 4.5: Same as Fig. 4.4, but with $\alpha = 10^{-1}$. Image from [86].

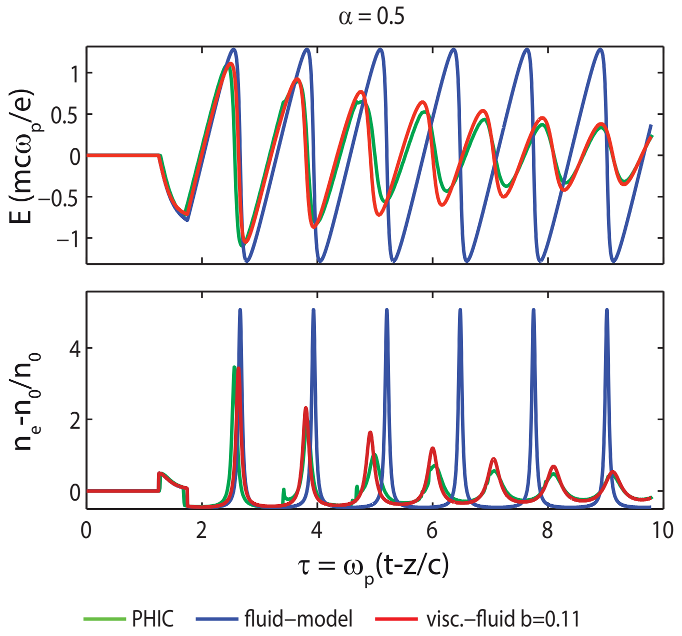

Figure 4.6: Comparison between the 1D rigid fluid model and 1D PIC, square bunches with $\sigma = 0.25\lambda_p$, $\alpha = 0.5$. Top panel: electric field E; bottom panel: normalized perturbation of the background electron density from the equilibrium $(n_e - n_0)/n_0$. Green line: PHIC code simulation results; blue line: same physical quantities, computed through the fluid model. The red line represents the results obtained through the addition of a damping term to the fluid model, with a damping coefficient $b = 0.11$. Image from [86].

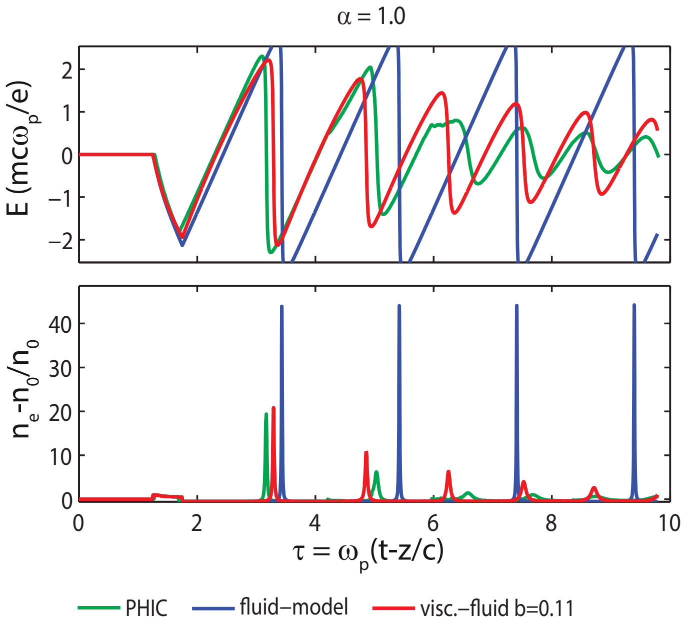

Figure 4.7: Same as Fig. 4.6, but with $\alpha = 1.0$. Image from [86].

Chapter 5

Architect: a hybrid kinetic-fluid model for PWFA

The hybrid kinetic-fluid code Architect is presented. Its model, numerical schemes, time scaling and the comparison with 3D fully kinetic simulations are discussed. Finally the main features of beam-driven plasma wakefields in more than one dimension are treated and shown to be reproduced by Architect simulations.

5.1 Motivations

Due to the significant amount of computational resources (i.e. number of cores and simulation time) required for standard parallelized 3D PIC simulations of typical experimental set-ups for plasma acceleration, many efforts have been devoted to perform faster simulations with retained accuracy. In particular, the codes using the quasi-static (QSA) approximation [38, 39] proved to significantly reduce the computational time required to simulate plasma acceleration involving driving laser pulses (e.g. WAKE [39, 40]), particle beams (e.g. LCODE [87, 88], HiPACE [43]) or both (e.g. QuickPIC [41, 42]) when the driver evolution is significantly slower than the wake evolution. The QSA allows to decouple the driver and the plasma evolution in highly relativistic regimes, requiring then a larger integration time-step. Apart from the high γ factors in the driver particles, another requirement for the QSA to ensure predictivity is the invariance of the system with respect of the comoving variable $\xi = z - v_{driver}t$. High spatial gradients in the plasma channel (e.g. a sharp capillary entrance) do not satisfy this condition, making QSA less accurate. The use of Graphic Processing Units (GPU) for PIC simulations proved to be a possible solution to reduce the required run-time as in the code PIConGPU [89].

To address the need for a quick simulation code for PWFA, the novel 2D hybrid kinetic-fluid code Architect has been developed to aid the design of plasma acceleration experiments in the weakly nonlinear regime [18], such as the COMB, planned at at SPARC_LAB facility [48] (see also Section 6.1). The code uses PIC methods to evolve electron bunches propagating along a plasma channel, and a fluid approach to evolve the background plasma electrons instead of fully kinetic methods. The separation of the two electron species evolved by the code is fictious, demanded by computational needs with no relevant physical consequences. The ions in the plasma channel are treated as a uniform immobile background.

The code provides an example of the interaction between kinetic and fluid models for two different species (i.e. beam and plasma electrons). One of the earliest examples of the hybrid fluid-kinetic approach for PWFA is provided by an earlier version of LCODE, where the QSA and further approximations to the fluid and macroparticle equations were added [44]. The quasistatic code QFluid [46, 90], used to study LWFA for the experiment ExIn planned at SPARC_LAB is another example of hybrid fluid-kinetic code for plasma acceleration. Architect has been developed to overcome some of the limitations of the QFluid version oriented to PWFA, primarily given by the quasistatic approximation, which does not allow to accurately study plasma channels with a longitudinal density which varies significantly over distances smaller than λ_p and the dynamics of particles which are slowed down to non relativistic velocities. Architect does not introduce approximations in the cold fluid equations and in the kinetic equations for particles except for the assumption of cylindrical simmetry. This and the possibility to correctly initialize the electromagnetic fields of the bunches allows to flexibly study the transition between the vacuum and the plasma capillary. The interaction between the kinetic and fluid models is provided by the electromagnetic fields integrated from the current densities of both the species, projected on the computational grid and the evolution of the two specied under the effect of the fields themselves, extrapolated from the grid.

The tratement of the plasma wake with a fluid model instead of a kinetic model considerably increases the speed of the code with respect of a fully kinetic code and does not need parallelization. The capability to have a fast running tool would not only serve for pure theoretical investigation but it will offer to the experimental team a feedback tool to help discriminate results during experimental runs.

5.2 Hybrid numerical schemes

The self-consistent model of Architect is given by Maxwell equations, the relativistic cold fluid equations and the beam macroparticle equations:

$$
\begin{aligned}
\partial_t \mathbf{B} &= -\nabla \times \mathbf{E} \\
\partial_t \mathbf{E} &= e\mu_0 c^3 \left(n_e \boldsymbol{\beta}_e + n_\mathrm{b} \boldsymbol{\beta}_\mathrm{b} \right) + c^2 \nabla \times \mathbf{B}, \\
\frac{\partial n_e}{\partial t} + \nabla \cdot \left(\boldsymbol{\beta}_e c n_e \right) &= 0, \\
\frac{\partial \mathbf{p}_e}{\partial t} + \boldsymbol{\beta}_e c \cdot \nabla \mathbf{p}_e &= -e(\mathbf{E} + \boldsymbol{\beta}_{\boldsymbol{e}} c \times \mathbf{B}), \\
\frac{d\mathbf{p}_\mathrm{p}}{dt} &= -e(\mathbf{E} + \boldsymbol{\beta}_\mathrm{p} c \times \mathbf{B}), \\
\frac{d\mathbf{x}_\mathrm{p}}{dt} &= \boldsymbol{\beta}_\mathrm{p} c,
\end{aligned}
\tag{5.1}
$$

where $\mathbf{E}$ is the electric field, $\mathbf{B}$ the magnetic field, c the speed of light, $\boldsymbol{\beta}_\mathrm{e}$ is the relativistic β for the background electrons $\boldsymbol{\beta}_\mathrm{p}$ the relativistic β for the electron bunch particles, $\mathbf{p}_e$ is the fluid relativistic momentum for electrons, n_e is the electron density and n_b the bunch density. For each single particle of the kinetic bunch(es) we identify a relativistic momentum, $\mathbf{p}_\mathrm{p}$, a relativistic beta, $\boldsymbol{\beta}_\mathrm{p}$, and a position, $\mathbf{x}_\mathrm{p}$. The first two equations are Faraday's law and Ampere's law respectively. The third and fourth equations are respectively the fluid mass conservation and the fluid momentum equations, referred to the plasma background electrons, treated as a single fluid. The fifth and sixth equations are the relativistic equations of motion, referred to each of the beam macroparticles. The model equations are integrated on a cartesian $r - z$ grid, with assuption of cylindrical symmetry. The sources for Ampere's law are the summed currents of the plasma background electrons and the beam electrons. The beam particles' positions and velocities are projected on the grid with PIC methods [35] to find the source terms $\mathbf{J}_b = n_\mathrm{b} \boldsymbol{\beta}_\mathrm{b} c$, while the fluid contribution is given by $\mathbf{J}_e = n_e \boldsymbol{\beta}_e c$ computed on the grid. The electromagnetic fields $\mathbf{E}$, $\mathbf{B}$ can then be found through a FDTD scheme [84], briefly reviewed in cartesian coordinates in Appendix B. The updated electromagnetic fields are used as forcing terms to advance both the beam particles in phase space and the fluid species' quantities. The equations of motion of the particles are integrated with a leap-frog scheme, using Boris algorithm for Lorentz force [35], reviewed in Appendix B. The advancement of the fluid quantities n_e, $\mathbf{p}_e$ by advection is performed through the shock capturing FCT scheme [91–93] to cacth the bubble-like features in the weakly nonlinear regime. The electromagnetic advance in the fluid momentum equation is performed through an operator splitting technique [53, 93]. These last steps give the updated particle positions and momenta and the updated fluid density and momentum on the grid, closing the loop (see Fig. 5.1), which is iterated through the simulation.

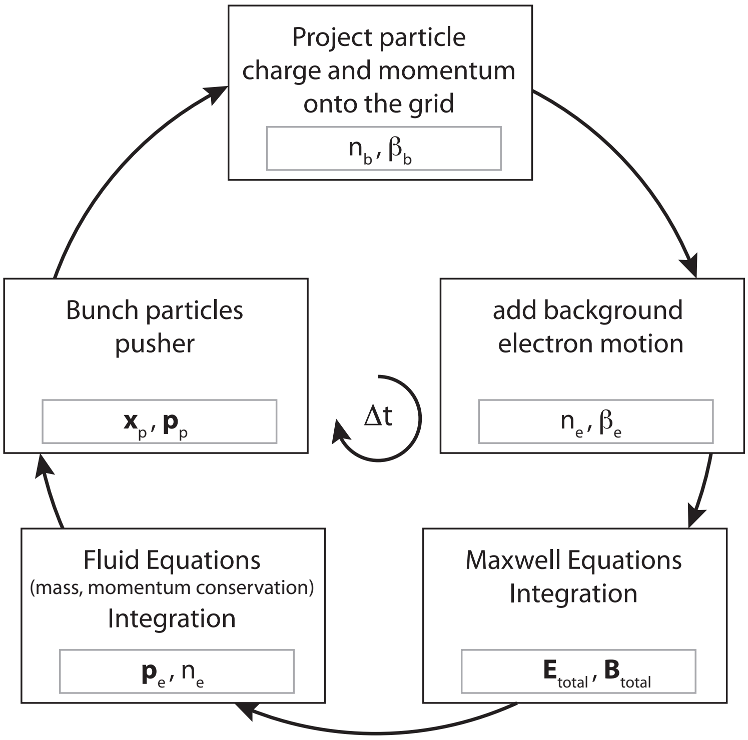

Figure 5.1: Temporal loop of Architect

The spatial centering of the physical quantities is summarized in Fig. 5.2. A more detailed representation of the code mesh is reported in Appendix C. The longitudinal direction of acceleration is the z axis. The electromagnetic quantities (fields and currents) are centered as in the Yee cell of the FDTD scheme (see Appendix B), while fluid quantities are cell-centered. The fluid grid is shifted radially by a quantity $\Delta r/2$ with respect of the Yee grid. The position of the electromagnetic grid avoids the singularity on axis in the radial derivative of E_z in cylindrical coordinates, involved in Ampere's law. Due to cylindrical symmetry, symmetry conditions are imposed on axis (r = 0), free flux conditions are imposed on the other edges. To save memory and simulation time the grid moves at speed c along the z axis, following the center of mass of the beam.

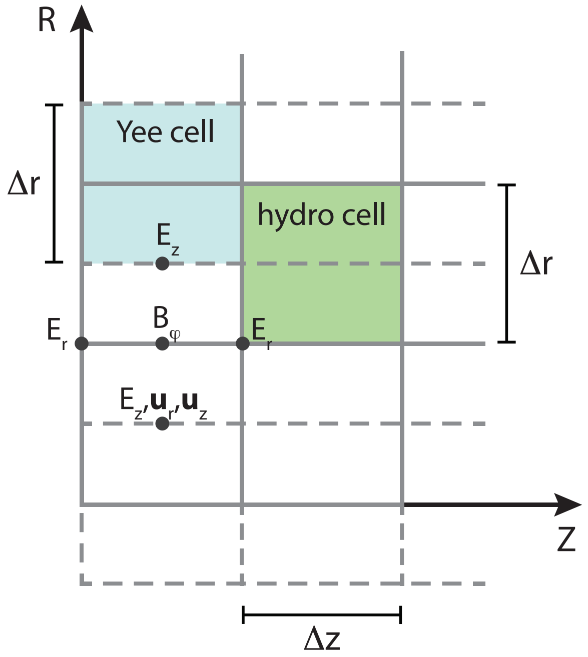

Figure 5.2: Schematic of physical quantity spatial centring. Figure from [94].

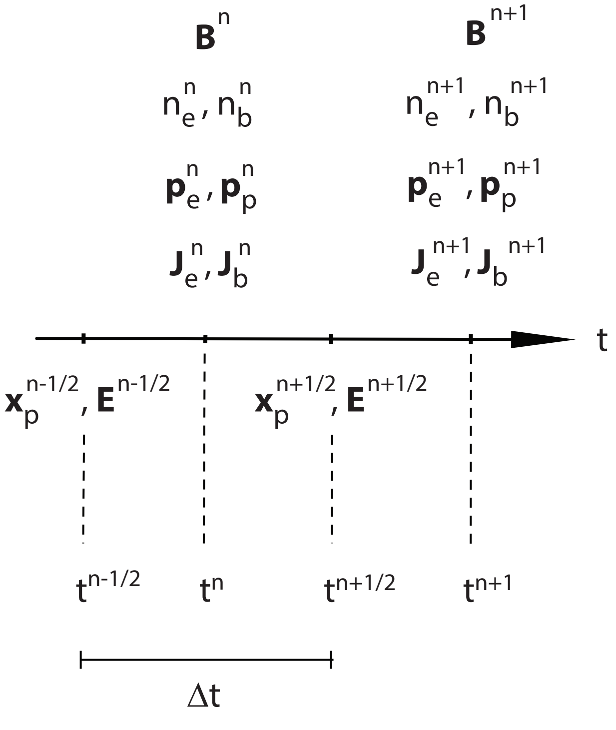

Figure 5.3: Schematic of physical quantities time centring.

The time centering of the physical quantities is shown in Fig. 5.3. The electromagnetic fields are shifted by a quantity $\Delta t/2$ as in the FDTD scheme, to obtain a second order accuracy in time as in a sort of electromagnetic leap-frog scheme (see Appendix B).

The different centering of the quantities implies the need of an interpolation between the old and the updated values in the routines of the code, as discussed in [35]. In Architect such interpolations are performed linearly between the two timesteps. The positions of the particles are interpolated between two timestep to obtain the position of the currents. The magnetic field in Lorentz law must be interpolated to perform a Boris rotation (recalled in Appendix B, see also [35]) and in the fluid advance.

5.2.1 Bunch field initialization

The FDTD scheme evolves the self-consistent field of the simulated system integrating the curl equations in the Maxwell equations set. Taking the time derivative of the divergence equations of the field and inserting the curl equations

$$\begin{aligned}\frac{\partial}{\partial t}\left(\nabla\cdot\mathbf{B}\right) &= \nabla\cdot\left(\frac{\partial\mathbf{B}}{\partial t}\right)=\nabla\cdot\left(-\nabla\times\mathbf{E}\right)=0\\ \frac{\partial}{\partial t}\left(\nabla\cdot\mathbf{E}-\frac{\rho}{\varepsilon_0}\right) &= \nabla\cdot\left(\frac{\partial\mathbf{E}}{\partial t}\right)-\frac{1}{\varepsilon_0}\frac{\partial\rho}{\partial t}=-\frac{1}{\varepsilon_0}\left(\nabla\cdot\mathbf{J}+\frac{\partial\rho}{\partial t}\right),\end{aligned}\tag{5.2}$$

it can be seen that the divergence of the $\mathbf{B}$ field and the quantity $\nabla\cdot\mathbf{E}-\frac{\rho}{\varepsilon_0}$ are constant as long as the curl equations for the field and the continuity equation hold.

While in many PIC applications using the FDTD scheme the fields can initially be set to zero (e.g. in case of initial neutrality of the plasma), in globally non neutral applications as plasma acceleration it is crucial to properly initialize the electromagnetic fields. In a PWFA application with initial plasma neutrality, the field initialization reduces to find the electromagnetic fields of the relativistic bunches. At present Architect allows to initialize the fields in a quick and accurate way, used also in the 3D PIC code ALaDyn [17].

In a typical PWFA scenario the electron beam is initially moving at speed $\beta_0 c$ along the longitudinal direction. The coordinates z', r' in a Lorentz frame comoving with the bunches are:

$$z'=\gamma_0(z-\beta_0 ct),\; r'=r,\tag{5.3}$$

where the unprimed quantities are referred to the laboratory frame. In paraxial approximation, i.e. transverse velocities negligible with respect of the longitudinal velocity, and low energy spread the magnetic field in the moving frame $\mathbf{B}'$ is zero and the vector potential in the same frame $\mathbf{A}'$ can be set to zero. Since under these assumptions the

Coulomb gauge $\nabla' \cdot \mathbf{A}' = 0$ holds in that frame, the electrostatic potential in the moving frame Φ' satisfies the Poisson equation

$$\left(\frac{\partial^2}{\partial z'^2} + \frac{1}{r'}\frac{\partial}{\partial r'}r'\frac{\partial}{\partial r'}\right)\Phi' = \frac{e}{\varepsilon_0}n'_{\mathrm{b}}, \tag{5.4}$$

where n'_{b} is the charge density in the moving frame. The Lorentz transformation of the charge density and of the potential four-vector yields

$$\begin{aligned} n_{\mathrm{b}} &= \gamma_0 n'_{\mathrm{b}} \\ \Phi &= \gamma_0 \Phi' \\ A_z &= \gamma_0 \frac{\beta_0}{c}\Phi' = \frac{\beta_0}{c}\Phi \\ A_r &= A'_r = 0. \end{aligned} \tag{5.5}$$

The transformations given by Eqs.(5.5) allow to finally write Poisson equation in Eq.(5.4) as

$$\left(\frac{\partial^2}{\partial z'^2} + \frac{1}{r'}\frac{\partial}{\partial r'}r'\frac{\partial}{\partial r'}\right)\Phi = \frac{e}{\varepsilon_0}n_{\mathrm{b}}. \tag{5.6}$$

Since the beam is translating with constant velocity $\beta_0 c$ along the z direction in the laboratory frame, all the physical quantities in that frame are functions of $z - \beta_0 ct = z'/\gamma_0$. Thus the derivatives of the quantities in the lab frame satisfy the following relations:

$$\begin{aligned} \frac{\partial}{\partial z'} &= \frac{\partial z}{\partial z'}\frac{\partial}{\partial z} = \frac{1}{\gamma_0}\frac{\partial}{\partial z} \\ \frac{\partial}{\partial t} &= \frac{\partial z'}{\partial t}\frac{\partial}{\partial z'} = -\gamma_0\beta_0 c\frac{\partial}{\partial z'}. \end{aligned} \tag{5.7}$$

The first of Eqs.(5.7) and the second of Eqs.(5.3) allow to write Eq.(5.6) as

$$\left(\frac{1}{\gamma_0^2}\frac{\partial^2}{\partial z^2} + \frac{1}{r}\frac{\partial}{\partial r}r\frac{\partial}{\partial r}\right)\Phi = \frac{e}{\varepsilon_0}n_{\mathrm{b}}. \tag{5.8}$$

The last equation can be discretized on the grid through finite differences to obtain a linear system with a band coefficient matrix. The solution of such system can be found with standard numerical techniques for linear algebra. Once the electrostatic potential in the laboratory frame Φ is found, the electromagnetic fields in the lab frame can be found, using Eqs.(5.7, 5.5):

$$\begin{aligned}
E_z &= -\frac{\partial\Phi}{\partial z} - \frac{\partial A_z}{\partial t} = -\frac{1}{\gamma_0^2}\frac{\partial\Phi}{\partial z} \\
E_r &= -\frac{\partial\Phi}{\partial r} \\
B_\varphi &= -\frac{\partial A_z}{\partial r} = -\frac{\beta_0}{c}\frac{\partial\Phi}{\partial r} = \frac{\beta_0}{c}E_r
\end{aligned} \tag{5.9}$$

The density of a Gaussian relativistic electron bunch and the corresponding transverse electric field computed by Architect with this technique are shown in Fig. 5.4. The central section in the transverse direction of the same electric field is shown in Fig. 5.5. In Architect the iterative method Successive Over Relaxation (SOR) (see e.g. [95]) is implemented to solve the above mentioned discretized Poisson equation. A version of the SOR method optimized for sparse matrices allows to intialize the electromagnetic fields in less than a minute on a single cpu even with much refined meshes.

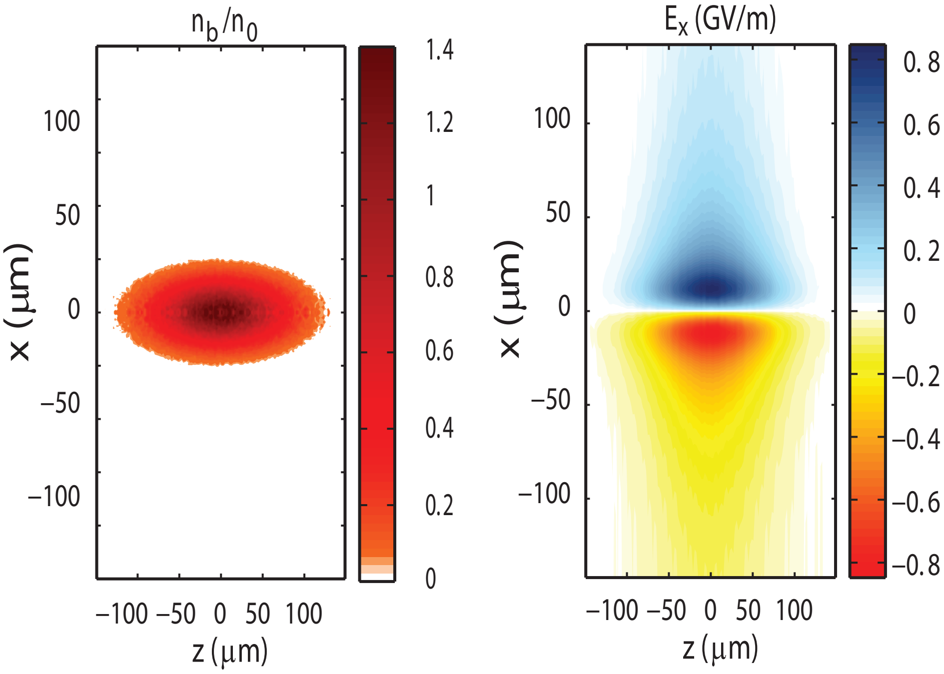

Figure 5.4: Left panel: Gaussian electron bunch density. Right panel: corresponding transverse electric field E_x computed with the initialization method implemented in Architect. The electron bunch parameters are $\sigma_z = 50\,\mu$m rms-length in the longitudinal propagation direction, $\sigma_x = \sigma_y = 8\,\mu$m rms-width in the transverse direction, charge $Q = 113$pC, $\gamma = 200$. The mesh resolution is $\Delta z = 1.25\,\mu$m, $\Delta r = 0.8\,\mu$m.

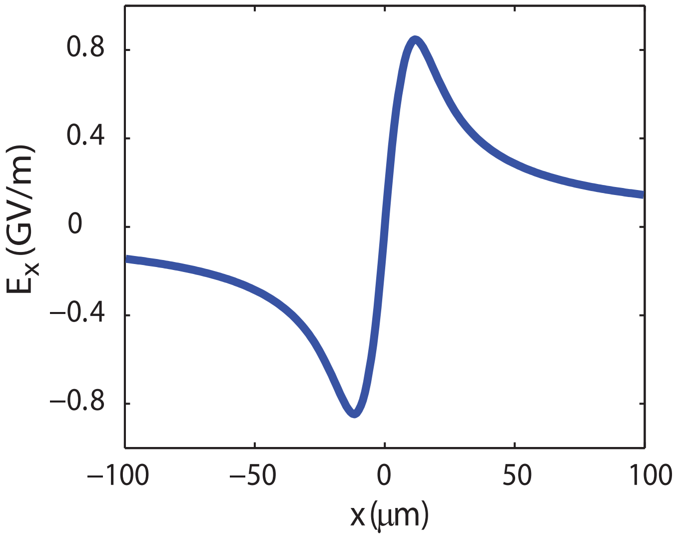

Figure 5.5: Central section of transverse electric field E_x of an electron bunch computed with the initialization method implemented in Architect. The electron bunch and mesh parameters are the same of Fig. 5.4.

5.3 Validation against code ALaDyn

Architect has been validated up to the weakly nonlinear regime against the full 3D PIC code ALaDyn [15–17]. Figure 5.6 shows the results of a comparison between the two codes. It refers to the propagation of a Gaussian bunch through a pre-ionized gas capillary with a uniform background density of n_0 =10^{16} cm^{-3} in the weakly nonlinear regime. The bunch rms-sizes are σ_z =50 μm, $\sigma_x = \sigma_y = 8$ μm and its normalized emittance is $\varepsilon_{n,x} = \varepsilon_{n,y} = 1$ mm-mrad. With a charge of $Q = 110$ pC the nonlinearity parameters have values $\alpha = 2.6$, $\tilde{Q} = 0.5$. ALaDyn PIC simulations have been performed with a resolution of 1 µm in the longitudinal direction and 0.4 µm in the transverse directions, for a total of 496 cells in z and 288 cells in (x, y). Simulations use 16 particles per cell for the capillary gas, 1.5×10^6 particles for the driver and 0.8×10^6 particles for the witness. A simulation totally computes for 41×10^6 cells and 660×10^6 particles. Architect simulations have been performed with the same grid resolution: 1 µm in the longitudinal direction and 0.4 µm in the transverse direction, for a total length of 533 cells in z and 140 cells in r. The longitudinal direction has been chosen to accomodate two bubbles at the rear of the driver, discretised with 800×10^3 particles.

The beam dynamics comparison is shown comparing two key integrated quantities: the bunch transverse rms size and the transverse emittance. Figure 5.6 summarizes the comparison. We observe that the hybrid code well reproduces both the oscillation phase and the bunch maximum compression. The maximum bunch expansion is overestimated

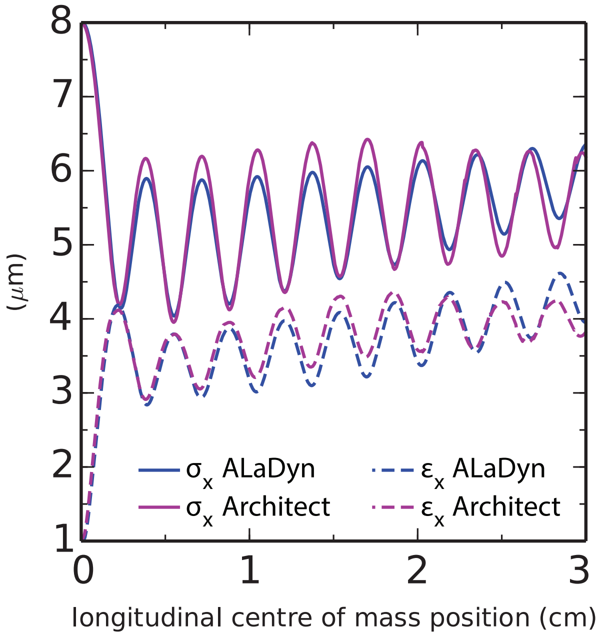

Figure 5.6: Driver bunch rms-transverse size and normalized emittance oscillation comparison. The blue lines (solid: σ_x; dashed: ε_x) have been obtained from an ALaDyn simulation, the magenta lines have instead been calculated with the hybrid code Architect. The initial bunch rms transverse size is $\sigma_x = 8$ μm with a 1 mm-mrad transverse normalized emittance, and it is injected into a capillary gas with a constant $n_0 = 10^{16}\text{cm}^{-3}$ background number density. Figure from [94]

by the hybrid code. The discrepancy is as small as 3% in an early phase at its maximum discrepancy is about 5%. We also observe that we have good agreement on the transverse bunch normalized emittance: normalized emittance oscillating phase and its series of maxima and minima are well reproduced by the hybrid code.

Another benchmark case depicts how Architect reproduces the characteristic fishbone shape of a long driver subject to head erosion during the propagation in the plasma channel. The initial driver parameters are: charge $Q = 113$ pC, rms-length $50\,\mu$m, rms-transverse size $8\,\mu$m, normalized emittance $\varepsilon_n = 1$ mm-mrad, energy $E = 100$ MeV, energy spread $\Delta\gamma/\gamma = 0.1\%$. ALaDyn simulations have been performed with a resolution of 1 µm in the longitudinal direction and 0.4 µm in the transverse directions, for a total of 456 cells in z and 288 cells in (x, y). The simulations use 8 particles per cell for the capillary gas and 1.5×10^6 particles for the driver. The simulation totally computes for 38×10^6 cells and 300×10^6 particles. Architect simulations have been performed with the same grid resolution: 1 µm in the longitudinal direction and 0.4 µm in the transverse direction, for a total length of 533 cells in z and 460 cells in r. Figures 5.7 and 5.8 show the plasma and bunch densities computed respectively by ALaDyn and Architect after the driver has traveled a distance of 0.1 cm.

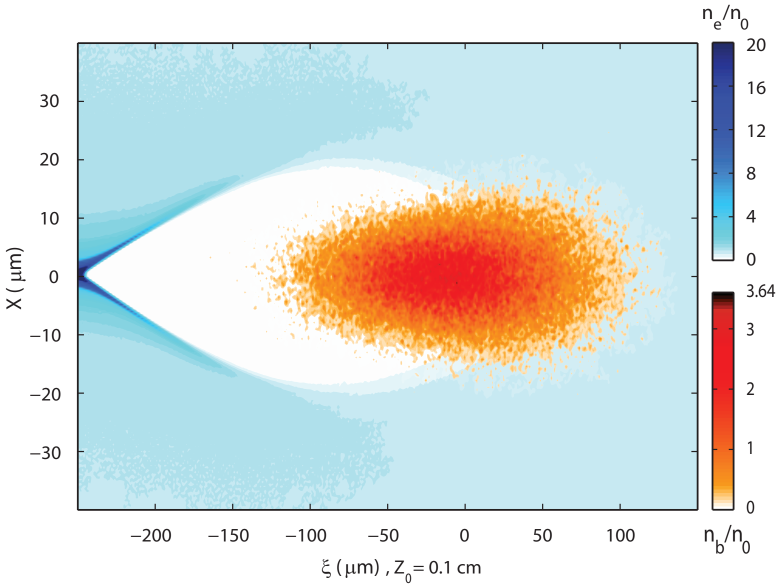

Figure 5.7: Background plasma (blue scale) and bunch (red scale) density colormap obtained from an ALaDyn simulation. The bunch has traveled a distance $Z_0 = 0.1$ cm. The horizontal axis shows the longitudinal distance $\xi = z - ct$ from the driver center of mass.

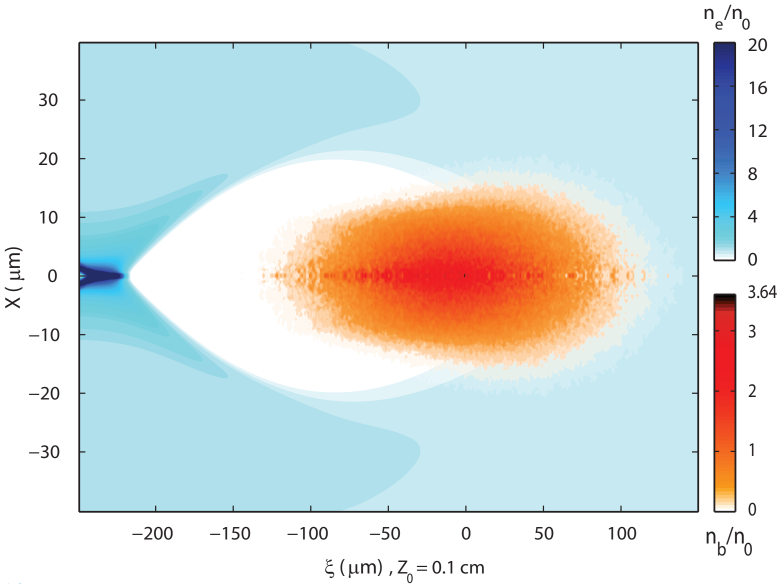

Figure 5.8: As in Fig. 5.7, but the densities are those computed by Architect. Using the cylindrical symmetry, the density in the $X < 0$ region has been obtained reflecting the density in the $X > 0$ region with respect to the $r = 0$ axis.

Figures 5.9 and 5.10 show the plasma and bunch densities computed respectively by ALaDyn and Architect after the driver has traveled a distance of 1 cm. The plasma channel has uniform background density $n_0 = 10^{16}\text{cm}^{-3}$. The bubble profile is well reproduced by the hybrid code, and the main features of the fishbone-like shape of the driver subject to head erosion after 1 cm are also catched.

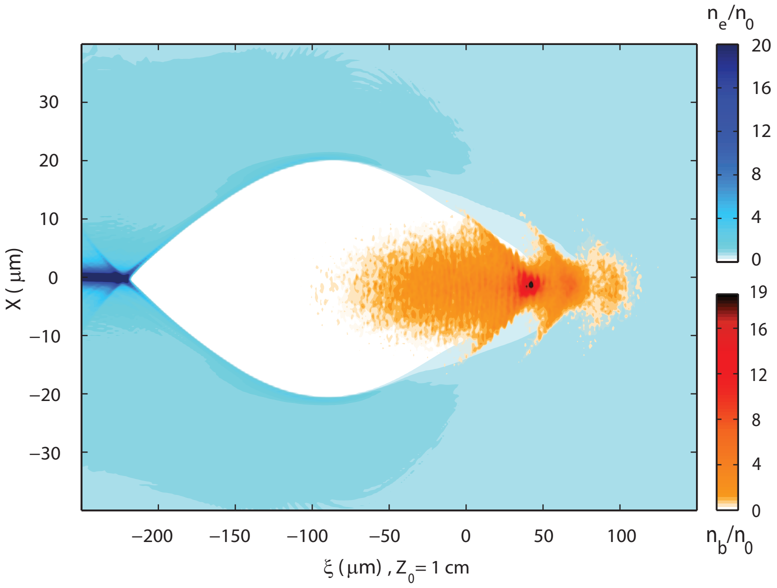

Figure 5.9: Background plasma (blue scale) and bunch (red scale) density colormap obtained from an ALaDyn simulation. The bunch has traveled a distance $Z_0 = 1$ cm. The horizontal axis shows the longitudinal distance $\xi = z - ct$ from the driver center of mass.

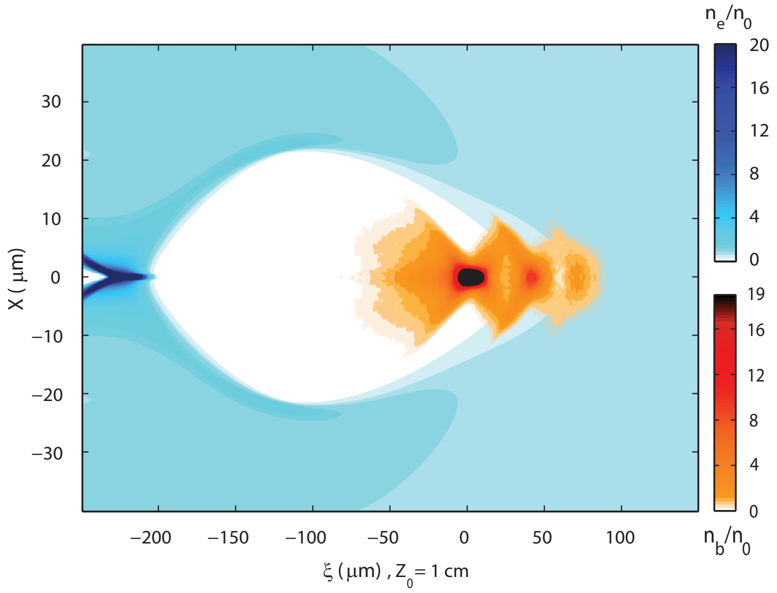

Figure 5.10: As in Fig. 5.9, but the densities are those computed by Architect. Using the cylindrical symmetry, the density in the $X < 0$ region has been obtained reflecting the density in the $X > 0$ region with respect to the $r = 0$ axis.

Figures 5.11, 5.12 show the longitudinal electric field on axis and radial electric field on a section perpendicular to the z axis at a distance $0.5\,\lambda_p$ from the driver center of mass, computed by the two codes after the driver has traveled a distance of 0.1 cm and 1 cm. The overestimate of the peak electric field by Architect in the rear of the bubble is caused by the excessive charge accumulation in that region; such high peak in the electron density is caused by the absence of thermal pressure in the cold fluid model used for the plasma. An upgrade of the model could include the thermal effects, improving the accuracy of the code predictions in nonlinear regimes where charge accumulation occurs.

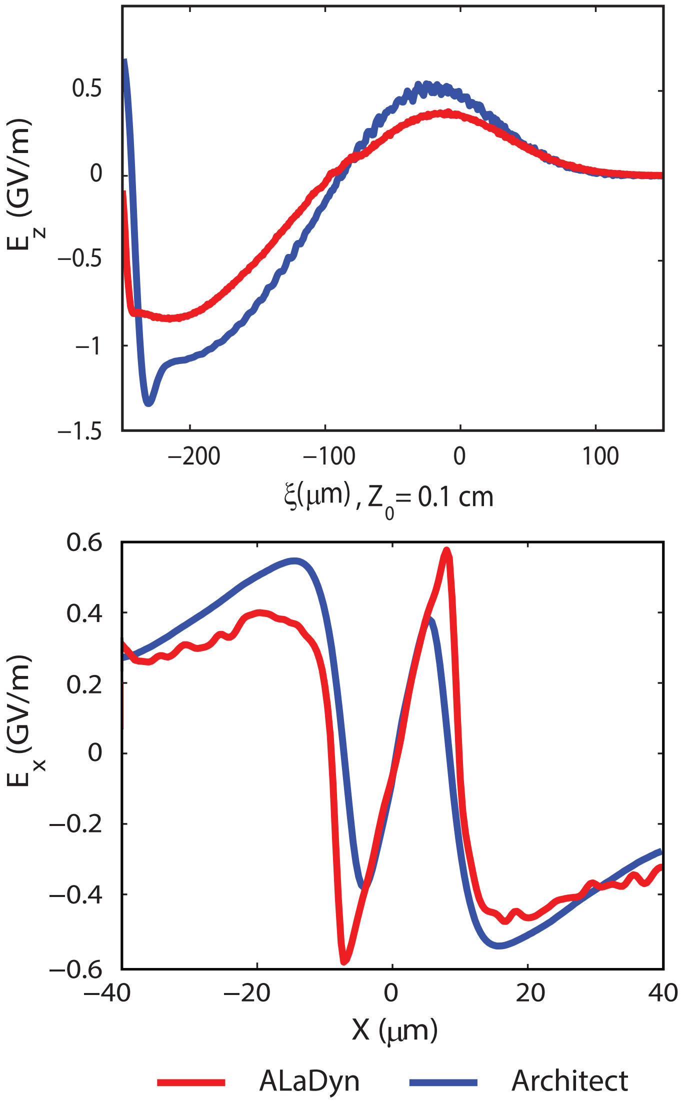

Figure 5.11: Electric fields comparison between Architect and ALaDyn at $Z_0 = 0.1$ cm. Top panel: longitudinal electric field E_z along the z axis. The horizontal axis is the longitudinal distance $\xi = z - ct$ from the driver center of mass. Bottom panel: transverse electric field E_x in a section perpendicular to the z axis, at distance $0.5\,\lambda_p$ from the driver center of mass. To represent the electric field computed by Architect in the $X < 0$ region, the field computed in the $X > 0$ region has been reflected with respect to the $r = 0$ axis and its sign has been changed, using the assumption of cylindrical symmetry.

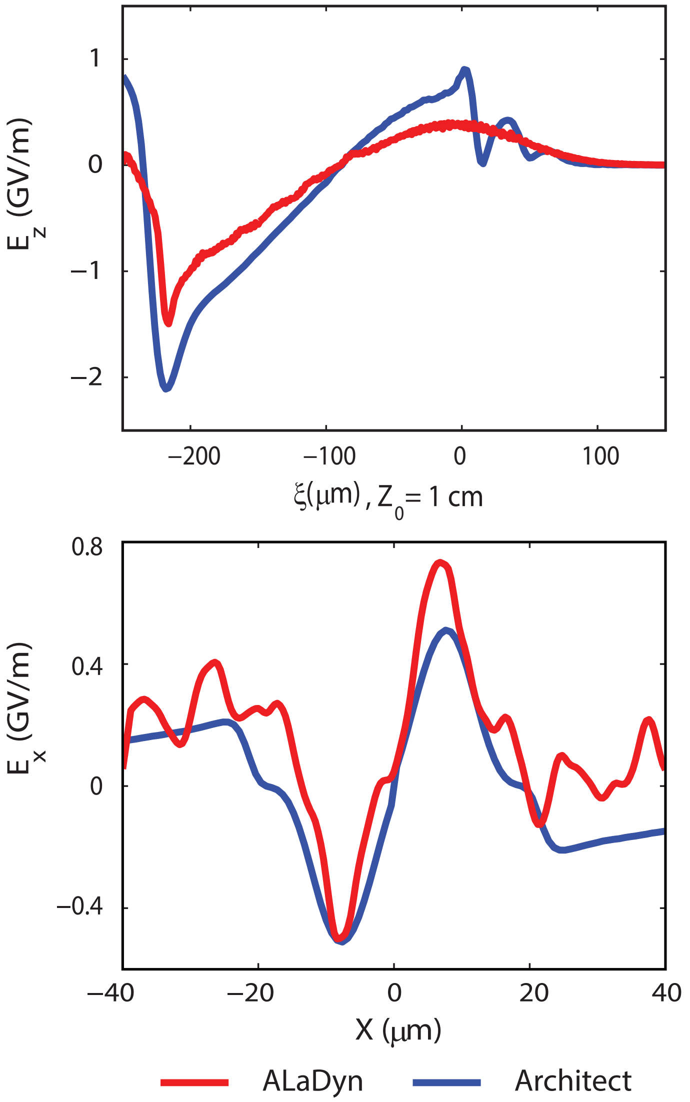

Figure 5.12: As in Fig. 5.11, but at $Z_0 = 1$ cm.

5.4 Simulation time scaling

To illustrate the simulation time scaling of Architect, the total simulation time of a series of run with a mesh composed of 533 cells in z and 460 cells in r, integration timestep $\Delta t = 0.44$ fs and different number of beam particles is shown in Fig. 5.13. The simulations to which the Figure refers have been run for a total distance of 1 cm inside the plasma channel. The reference simulation set-up is the one used for the results shown in Figs. 5.8, 5.10. The scaling highlights the influence of the beam particles on the total simulation time. The total run time scales linearly with the number of the particles even when the number of particles is five times smaller than the number of grid points.

Thus, for this choice of grid size, even with 50×10^3 beam particles the computation time needed for the integration of Maxwell equations and the fluid equations is negligible with respect to the time needed by the particle charge deposition and particle pushing routines. Thus, the total time needed for a 1 cm-simulation with acceptable agreement with a full-PIC code like the one shown in Fig. 5.10 (obtained using 300×10^6 particles) is less than 12 hours on a single processor.

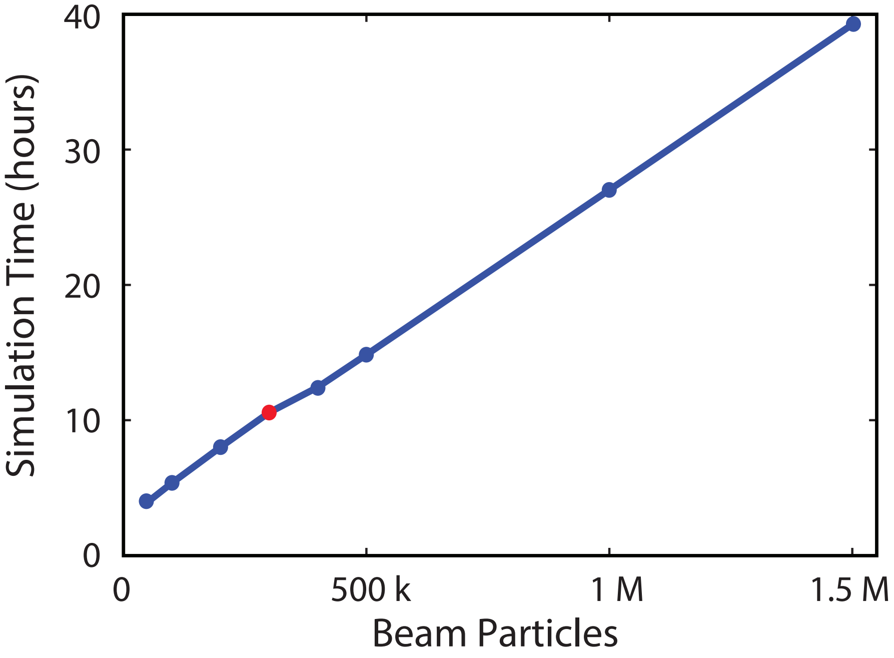

Figure 5.13: Architect simulation time on a single core vs number of bunch particles for a 1 cm run, with a mesh composed of 533 cells in z and 460 cells in r, integration timestep $\Delta t = 0.44$ fs. The point corresponding to the simulation of Figs. 5.7, 5.8, 5.9, 5.10, 5.11 and 5.12 is highlighted in red.

5.5 Plasma oscillations regimes in 3D

In three dimensions the conditions to determine the oscillation regime of the waves excited by a driver do not only involve the normalized peak density α as seen in 1D in Chap.3, but also the geometrical distribution of the perturbation caused by the driver to the initial plasma equilibrium. The geometrical features of the driver are accounted for by the parameter $\tilde{Q}$, also called normalized beam charge, defined as follows. Such parameter is the ratio between the number of beam electrons N_b and the number of plasma electrons in a cube of volume $k_p^{-3} = (\lambda_p/2\pi)^3$ with initial density n_0 [17, 18, 96], i.e.

$$\tilde{Q} = \frac{N_b k_p^3}{n_0}. \tag{5.10}$$

A uniformly distributed beam in the volume k_p^{-3} with $\alpha = 1$ would have $\tilde{Q} = 1$. Bunches with a multivariate Gaussian distribution, i.e. with density described by

$$n_b(x, y, z) = \alpha n_0 \frac{1}{(2\pi)^{3/2}\sigma_x\sigma_y\sigma_z} e^{-\frac{x^2}{2\sigma_x^2} - \frac{y^2}{2\sigma_y^2} - \frac{z^2}{2\sigma_z^2}} \tag{5.11}$$

have a particular experimental interest, since they are the easiest to produce and control. For such bunches the $\tilde{Q}$ parameter is equal to

$$\tilde{Q} = \alpha(2\pi)^{3/2}\sigma_z\sigma_x\sigma_y k_p^3 \tag{5.12}$$

In order for such a driver bunch to excite a wakefield and leave room for a witness bunch, its length must be much shorter than the plasma wavelength, i.e. $k_p\sigma_z \ll 2$. In addition the driver should be narrow, with $k_p\sigma_r \ll 1$, to avoid plasma return currents within the driver itself [14, 96]. In these conditions the driver volume is much smaller than k_p^{-3} and conditions for the parameters α and $\tilde{Q}$ corresponding to the different oscillation regimes can be identified. In the linear regimes both the conditions $\alpha \ll 1$ and $\tilde{Q} \ll 1$ hold. In weakly nonlinear regimes $\alpha > 1$ but $\tilde{Q} < 1$, while in strongly nonlinear regimes $\alpha > 1$ and $\tilde{Q} \gg 1$.

Figures 5.14, 5.15, 5.16 show the results of simulations performed with Architect of a bunch propagation in a uniform channel. They refer respectively to the linear, weakly nonlinear and nonlinear regimes, keeping the initial dimensions, emittance and energy of the bunch fixed. The plasma parameters, the bunch shape and initial energy and emittance were chosen from possible parameters for PWFA experiments at SPARC_LAB. The initial bunch rms transverse size is $\sigma_z = 50$ μm $\sigma_x = 8$ μm with a 1 mm-mrad transverse emittance and $\gamma = 200$, and it is injected into a capillary gas with a constant $n_0 = 10^{16} cm^{-3}$ background number density. The figures show the results after a propagation of $2\,\lambda_p$ inside the plasma channel, before a sensitive energy depletion of the driver. Increasing the bunch charge the plasma electron density and the fields in the driver wake change not only in magnitude but also in the shape with the rising of the nonlinear effects. Since the initial driver energy of the three simulations was kept fixed in the three simulations, the increase of the charge and thus of the magnitude of the fields tend to deform more the bunch under the effect of its own wake.

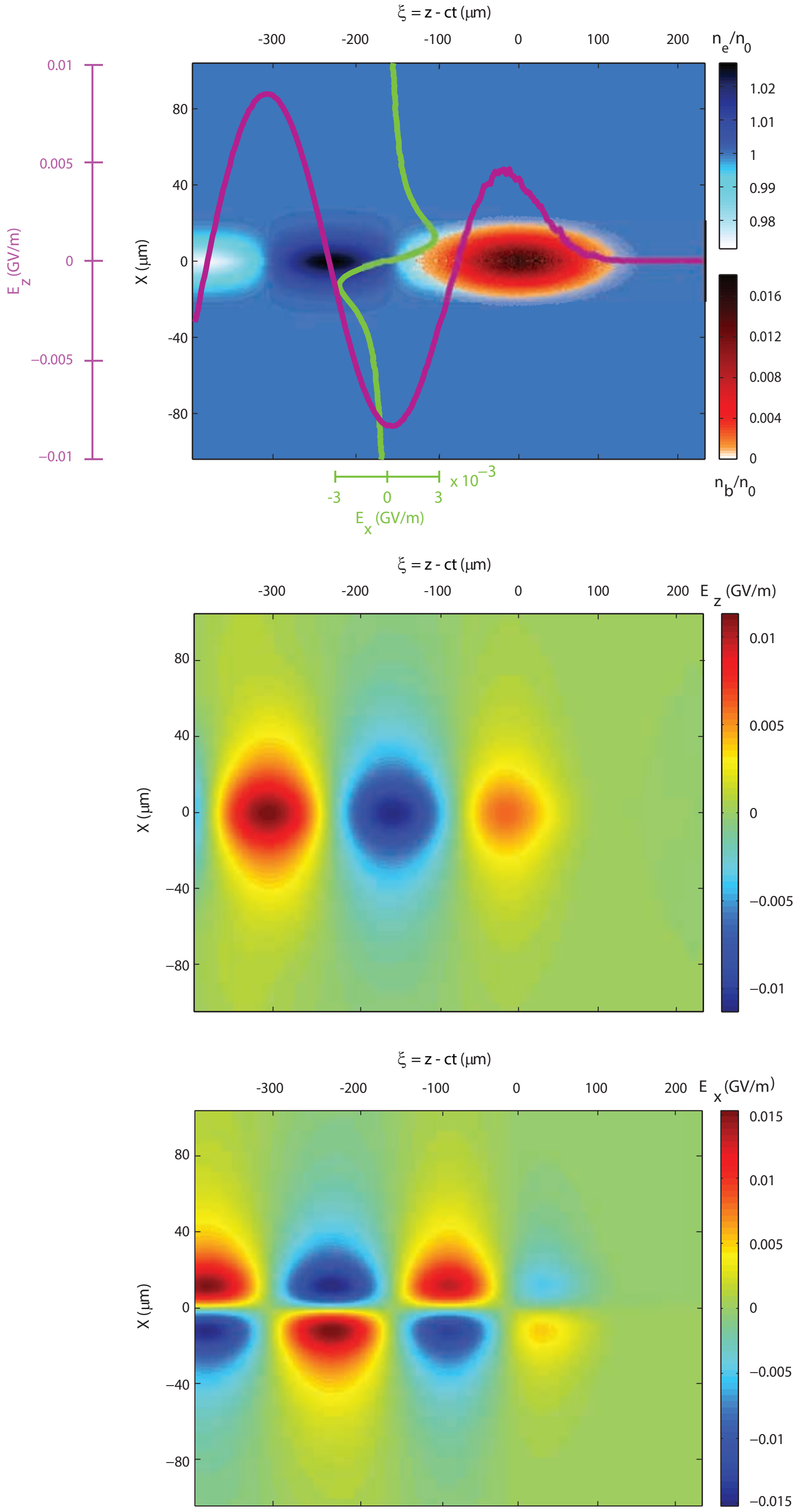

Figure 5.14: Architect simulation of beam propagation with $\tilde{Q} = 0.005$ (linear regime). Top panel: colormaps of plasma electron (blue scale) and beam (red scale) electron densities. Superimposed are the longitudinal electric field on axis (purple curve) and the x-component of the electric field in a section at distance $0.5\,\lambda_p$ after the driver (green curve). Medium panel: colormap of the longitudinal electric field. Bottom panel: colormap of the x-component of the electric field. The physical quantities in the region $X < 0$ have been obtained by reflection of the physical quantities with respect to the $r = 0$ axis, using the assumption of cylindrical symmetry. In the case of E_x the sign of the field has also been inverted in the region $X < 0$.

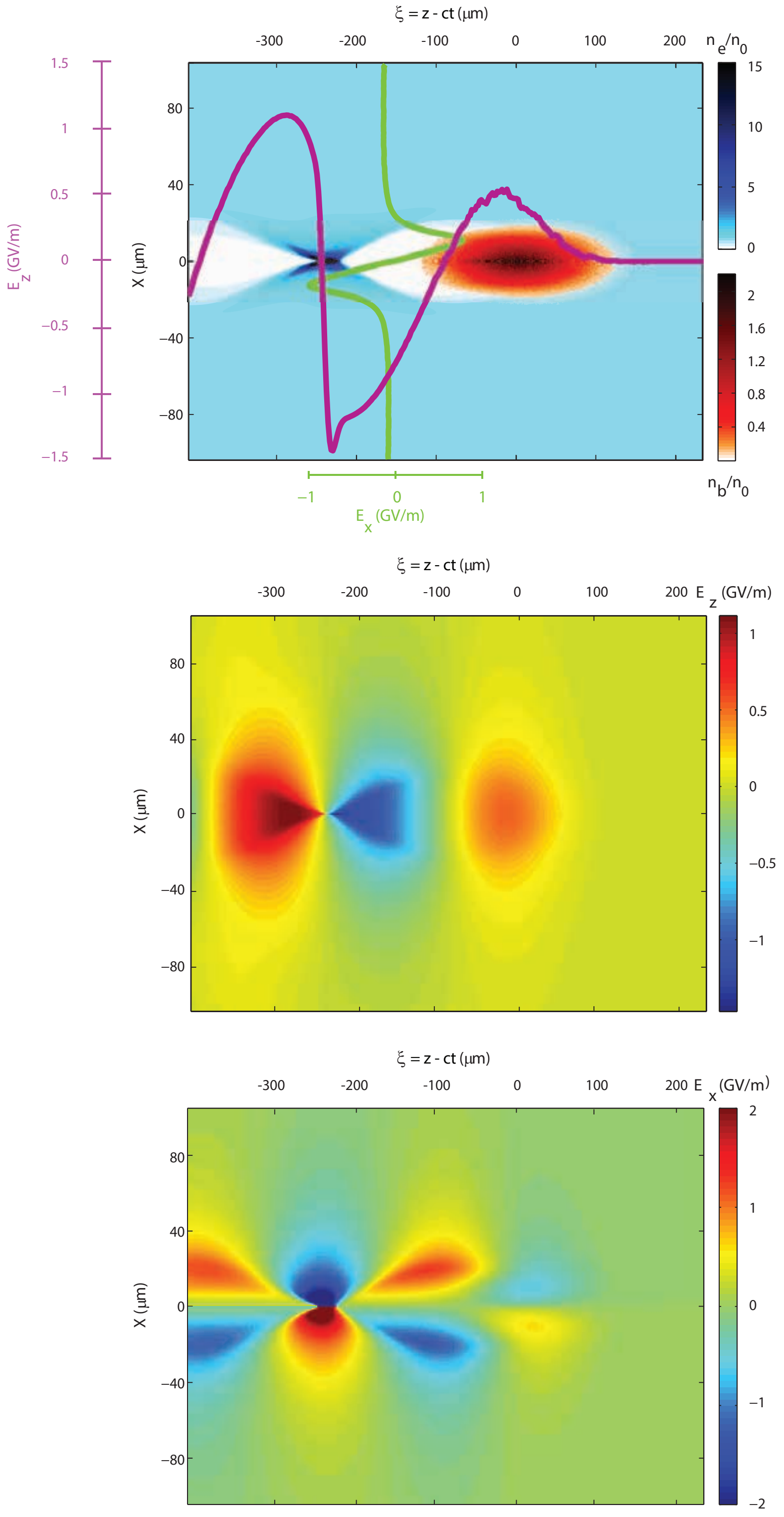

Figure 5.15: As in Fig. 5.14, but with $\tilde{Q} = 0.5$ (weakly nonlinear regime).

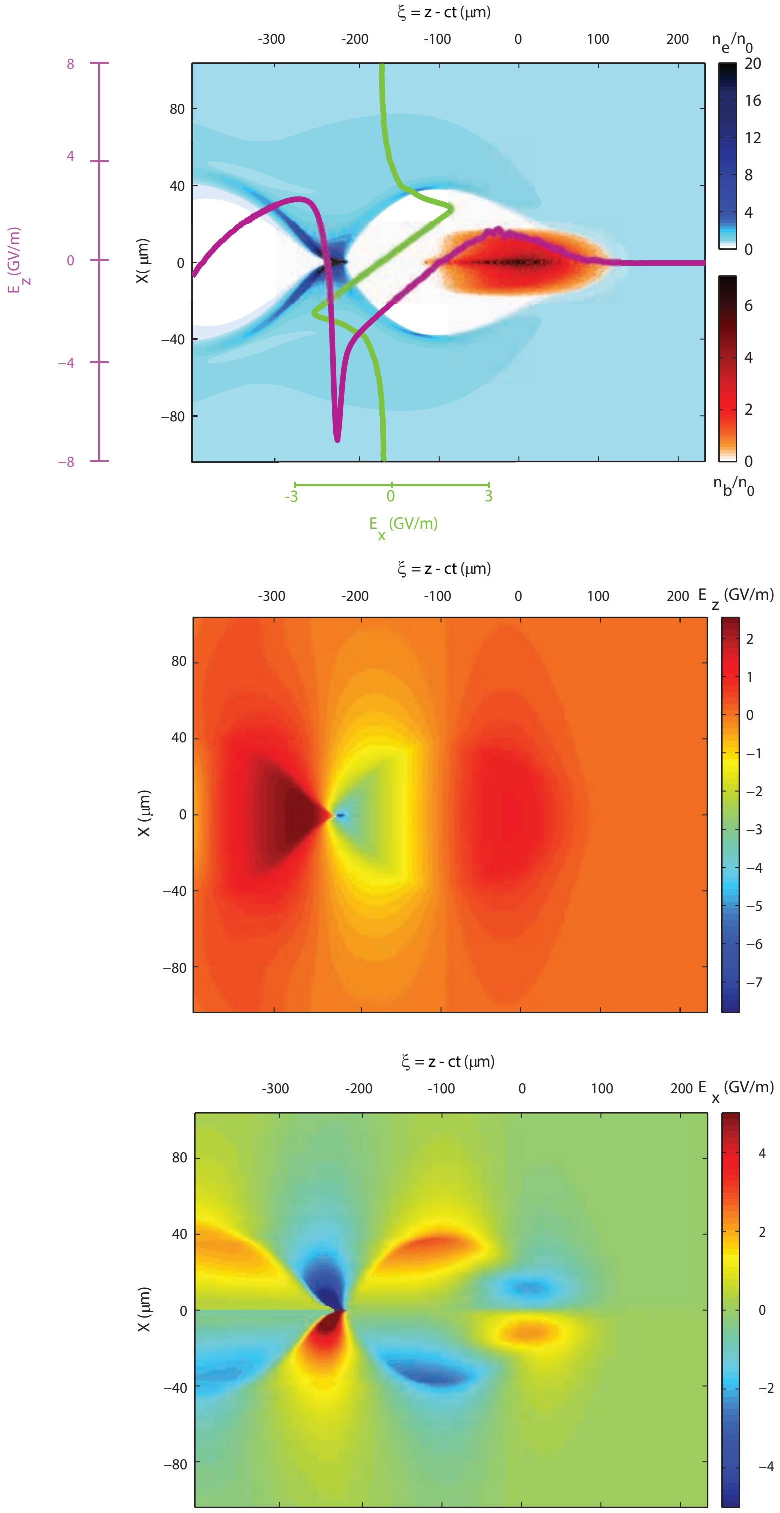

Figure 5.16: As in Fig. 5.14, but with $\tilde{Q} = 1.5$ (nonlinear regime).

In Section 3.2 it was shown than a limit of the 1D model is its impossibility to predict the complete depletion of electron in the region behind the driver. In more than one dimension both kinetic and fluid models can predict this effect [94], which is complete in a strongly nonlinear regimes called bubble or blowout regimes [14, 88]. Models for the plasma electron trajectories in the bubble region and in its surface, like in [97, 98] exist although they are mathematically involved and show disagreement with PIC simulations in the tail of the bubble. Intuitively, the focusing force of the positively charged region behind the driver pulls back the electrons pushed radially by the driver, closing the bubble. The electrons tend to overshoot, in turn creating a perturbation which could take the form of other bubbles if the wave behind the first bubble does not break (see Section 3.3). Some characteristics of the blowout regime made it very appealing for high energy PWFA. Namely these characteristics are the focusing forces linear with respect of radial distance from the center of the ion bubble, similar to those found in magnetic quadrupoles and the strong accelerating fields. Besides the width of the accelerating region behind the driver makes easier to accomodate a witness bunch. Drawbacks of the blowout regime are its low controllability due to the high nonlinearities and the high energy spread due high spatial variations of the accelerating field. This last feature could in principle be partially overcome with properly shaped witness to improve the beam loading, making the accelerating profile of the wave more flat (see e.g. [12]). It has been proposed the use of the weakly nonlinear regimes to obtain part of the controllability of the linear regimes and part of the good focusing properties and the high gradients of highly nonlinear regimes.

Chapter 6

Efficient PWFA design via Architect

Simple applications of the code Architect for the PWFA experiment COMB planned at SPARC_LAB facility are presented. The code is shown to be suited for systematic scans for driver matching, including the effects of different plasma channel density profiles. Finally the simulations of an electron bunch acceleration in a two-bunches case and in a multi-driver case are shown.

6.1 SPARC_LAB facility and the COMB experiment

SPARC_LAB (Sources for Plasma Accelerators and Radiation Compton with Lasers and Beams) [48] is an accelerator test facility in the INFN Laboratories of Frascati, born from the structures of the SPARC project [99]. The layout of the facility is depicted in Fig. 6.1. In the 12 m-long linear accelerator section electron beams can be produced from a high brightness photoinjector [100] and accelerated through the subsequent accelerating cavities up to 180 MeV. An upgrade to 200 MeV is forseen with the installation of accelerating cavities working in the C-band in place of the presently used cavities, working in the S-band. After the linac section the electron beam can be deviated by a magnetic dipole to one of the four beamlines, shown in Fig. 6.2. From the left the beamlines for Thomson scattering experiment [101], the externa injection LWFA experiment ExIn [90], THz source and diagnostics [102] and EOS diagnostics [103] and the 12 m-long undulator for Free Electron Laser (FEL) experiments [104–106] are shown.

Between the linac section and the FEL undulator the interaction chamber for COMB experiment will be placed. The interaction chamber will host a capillary made of the dielectric material acrylonitrile butadiene styrene (ABS), with a 1 mm-diameter circular section, ≈ 2 cm long. Inside the capillary a hydrogen gas will be injected, which will be ionized through a discharge between the edges of the capillary [50]. The plasma will have an initial density $n_0 = 10^{16}\mathrm{cm}^{-3}$, corresponding to a plasma wavelength of

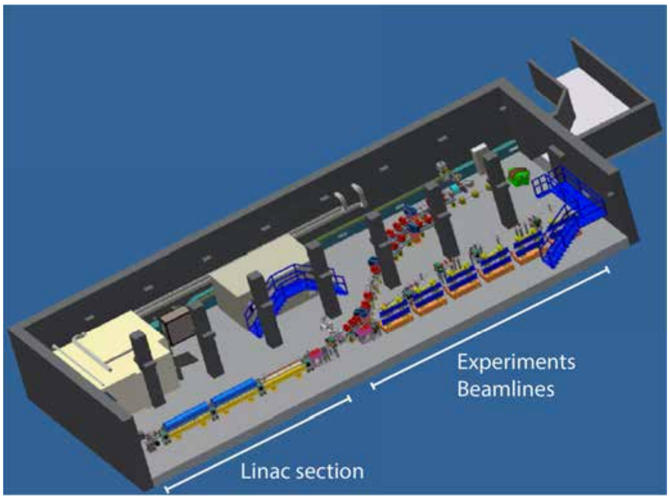

Figure 6.1: SPARC_LAB facility layout. Adapted from [48].

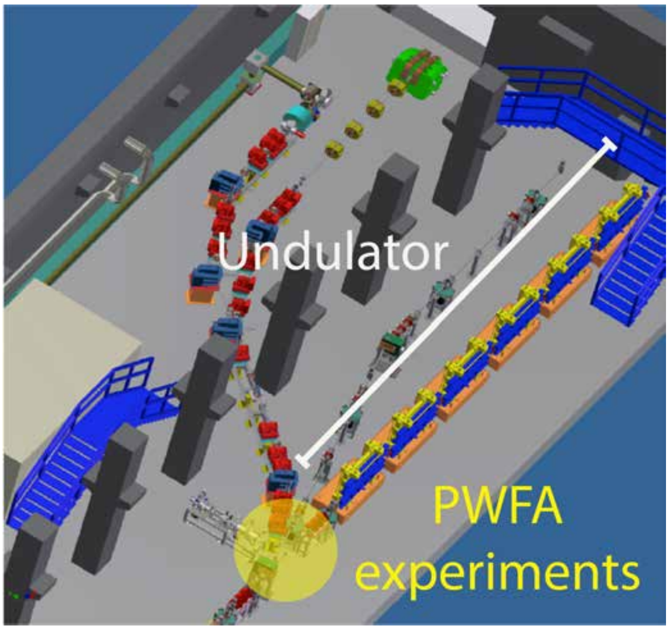

Figure 6.2: Beamlines of SPARC_LAB facility, highlighting PWFA interaction chamber site and the undulator for FEL physics experiments. Adapted from [48].

$\lambda_p = 334\,\mu$m, estimated initial pressure $P \approx 30$ mbar and estimated initial temperature $T \approx 4$ eV. The driver and witness bunches sequence will be produced in the photoinjector with proper spatial distance (order of λ_p between subsequent bunches) through the laser-comb with velocity technique [49]. The driver and witness bunches will be accelerated and focused in the conventional linac section until the injection in the plasma capillary. The experiment plans to resonantly excite plasma waves using three drivers of charge $Q \approx 100 - 200\,\mathrm{pC}$, rms-length $\sigma_z \leq 50\,\mu m$, rms-spot size $\sigma_r \leq 10\,\mu m$ at the capillary entrance, thus working in the weakly nonlinear regime ($\tilde{Q} \approx 0.5$, see Section 5.5). The witness bunch will have charge $Q \leq 50\,\mathrm{pC}$. Its dimensions will need to fit into the accelerating and focusing region of the bubble in which it will be injected, i.e. rms-length $\sigma_z \leq 10\,\mu m$ and rms-spot size $\sigma_r \leq 5\,\mu m$ at the capillary entrance. Both driver and witness bunches will be injected with a normalized emittance value of the order of $\varepsilon_n \approx 1$ mm-mrad, energy $E = 100$ MeV and an energy spread of $\Delta\gamma/\gamma = 0.1\%$. The goal of the experiment is to obtain an average accelerating gradient inside the plasma comparable and possibly greater than the ones obtainable with conventional acceleration techniques, and maintain a witness bunch quality, from the entrance to the exit from the capillary, comparable to the one obtainable with conventional accelerating techniques. A long term goal is to obtain a witness bunch quality acceptable to seed the free electron laser of the facility, i.e. normalized emittance of the order $\varepsilon_n \approx 1$ mm-mrad, energy spread $\Delta\gamma/\gamma \leq 1\%$. To obtain the described goals, detailed studies of the beam dynamics inside the plasma are necessary. The next sections of this chapter discuss simple applications of Architect for this purpose.

6.2 Driver matching conditions

As hinted in Section 2.5 the envelope equation

$$\sigma_x'' + \frac{p'}{p}\sigma_x' - \frac{\langle xF_{x,ext}\rangle}{\sigma_x \beta c p} = \frac{\varepsilon_n^2}{\gamma^2 \sigma_x^3} + \frac{\langle xF_{x,sc}\rangle}{\sigma_x \beta c p}. \tag{6.1}$$

can in principle be used to study the evolution of the envelope σ_x of a relativistic beam of average momentum p and normalized emittance ε_n^2 subject to external forces $F_{x,ext}$ and to its own transverse space charge forces $F_{x,sc}$. In a conventional accelerator envelope equations as Eqs.(6.1) (or Eq.(2.42) when the space charge forces are negligible with respect of emittance pressure) provide a powerful tool to assess the transverse beam evolution inside a beamline, since the expression of the external forces $F_{x,ext}$, representing the focusing magnets' forces, is known a priori from the lattice design. In plasma accelerators the focusing forces are not known a priori, except for calculations under strong approximations or under particular regimes. In the blowout regime of PWFA Eq.(2.42) can be used to study the evolution of a witness bunch surrounded by the focusing forces of the ion bubble [29, 71], assuming that the wakefield in the plasma does not change during the propagation in the channel. Under such assumption the external focusing forces are linear with respect to distance from the propagation axis and can be computed from Gauss law, which yields

$$F_{x,ext} = -kx, \; k^2 = \frac{e^2 n_0}{d\varepsilon_0}, \tag{6.2}$$

where $d = 2$ if the region uniformly filled with ions is approximated as a cylinder and $d = 3$ if it is approximated as a a sphere. In this case Eq.(2.42) becomes

$$\sigma_x'' + \frac{\gamma'}{\gamma}\sigma_x' + k_{ext}^2\sigma_x = \frac{\varepsilon_n^2}{\gamma^2\sigma_x^3}, \tag{6.3}$$

where

$$k_{ext}^2 = \frac{k^2}{\gamma m_e c^2} = \frac{e^2 n_0}{d\varepsilon_0 \gamma m_e c^2} = \frac{k_p^2}{\gamma d}, \tag{6.4}$$

Eq.(6.6) admits a stable solution, i.e. with no envelope (or betatron) oscillations, that reads

$$\sigma_x = \sqrt[4]{\frac{d}{\gamma}}\sqrt{\frac{\varepsilon_n}{k_p}}, \tag{6.5}$$

for a constant γ value. In the case of COMB, the propagation of the beam inside the plasma capillary is emittance-dominated, thus the space charge term is negligible with respect of the emittance pressure term. Equations (6.6, 6.2) can be used also in the weakly non linear regime as in COMB experiment, provided that the witness envelope remains confined in the part of the bubble-like region of the driver wake where the focusing forces can be considered linear. In such case the resulting envelope equation would read

$$\sigma_x'' + \frac{\gamma'}{\gamma}\sigma_x' + k_{ext}^2\sigma_x = \frac{\varepsilon_n^2}{\gamma^2\sigma_x^3}. \tag{6.6}$$

As discussed in [107], Eq.(6.6) gives not accurate predictions when referred to the driver envelope in PWFA. This because it is derived under assumption of bunch completely surrounded by the linear focusing forces, which is not the case of a driver bunch. Since the positively charged region forms roughly at half the length of the driver, its head will be eroded by the lack of focusing forces. A novel approach from [107] allows to use Eq.(6.6) to have some information about the driver matching. Let the driver bunch be conceptually sliced in ten parts, each of length σ_z , as shown in Fig. 6.3. The slices from 0 to 4, in the head of the driver, are subject to head erosion due to the lack of focusing forces. The rear of the bunch, where the bubble is formed, contains the slices from 5 to 9, which are thus collimated by the transverse fields of the bubble. In a typical driver for the COMB experiment the bubble starts to form from slice 5, approximately at the center of the driver, as highlighted in the figure. Eq.(6.6) can then be applied to the central driver slice.

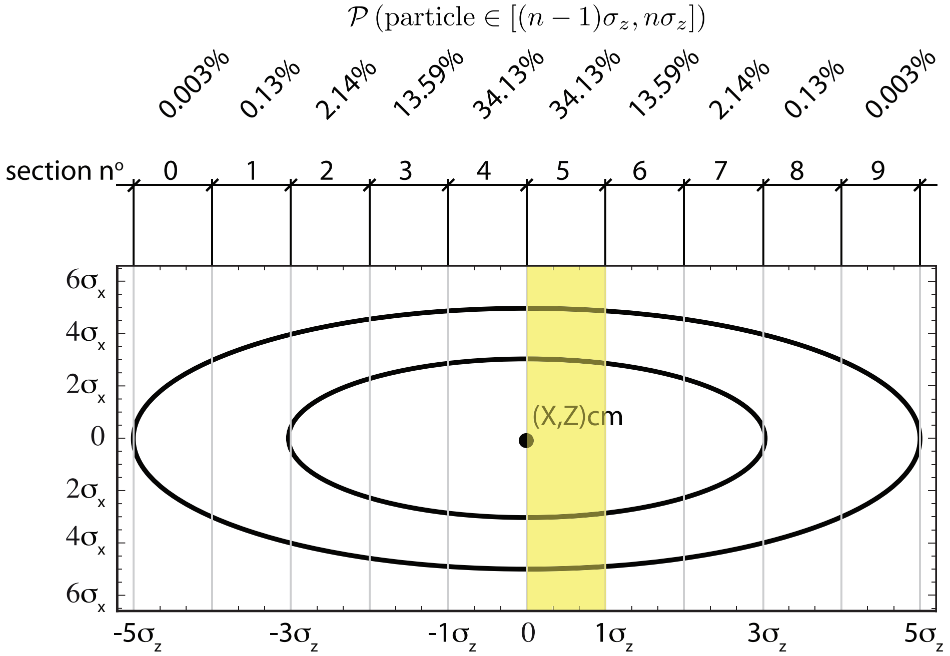

Figure 6.3: sliced diagram for a driver bunch travelling from right to left. The yellow highlighted slice is where, for our choice of driver parameters, the bubble originates. Figure from [107].

A case study for this concept consists in verifying the matching contidion for a COMB bunch with realistic parameters as $\sigma_z = 50$ μm, normalized emittance $\varepsilon_n = \varepsilon_{n,y} = 3$ mm-mrad, $\gamma = 200$, charge $Q = 170$ pC, propagating in a plasma channel of uniform density $n_0 = 10^{16}$ cm^{-3}. With the approximation of a cylindrical bubble Eq.(6.5) yields a matched transverse dimention of $\sigma_x = 4$ μm. Fig. 6.4, represents a series of Architec runs varying the transverse injection dimension σ_x from 3.9 μm to 4.4 μm. These dimensions refer to slice 5 transverse size, which is only a few percent different from the overall beam transverse size, thus the two sizes can be considered identical for sake of simplicity. Fig. 6.4 shows the increasing amplitude of the betatron oscillations when the rms size is changed from the theoretically computed equilibrium value of σ_x =4 μm.

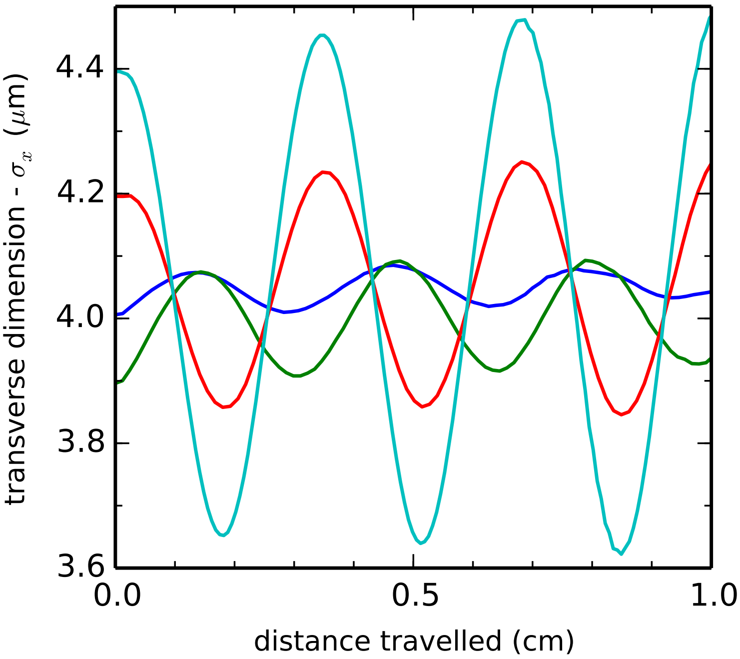

Figure 6.4: Transverse dimension -section 5 of Fig. 6.3- oscillations for bunch with different initial transverse size. Figure from [107].

6.2.1 Density ramps at plasma capillary entrance and exit

The plasma capillary model used in the simulations of Fig. 6.4 assumes a sharp transition between the vacuum and the capillary of uniform density n_0. A more realistic model can include a linear density ramp, in which in a distance L the plasma density increases from zero to n_0 at the capillary entrance. Such model could be used in the envelope equation inserting the proper expression of $n_0(z)$ in the k_{ext} term. The effect of ramp lengths L =1,2,3 λ_p on the matching condition found for sharp edge capillary model is shown in Fig. 6.5. The figure highlights that such a matching condition would be spoiled by any density ramp. The longer is the density ramp, the higher will be the amplitude of the resulting betatron oscillations. Possible solutions for this problem are the control with the highest possible accuracy of the density profiles especially at the capillary edge, or the use of a capillary ramp to gently bring the driver to the matching conditions as discussed in [108, 109].

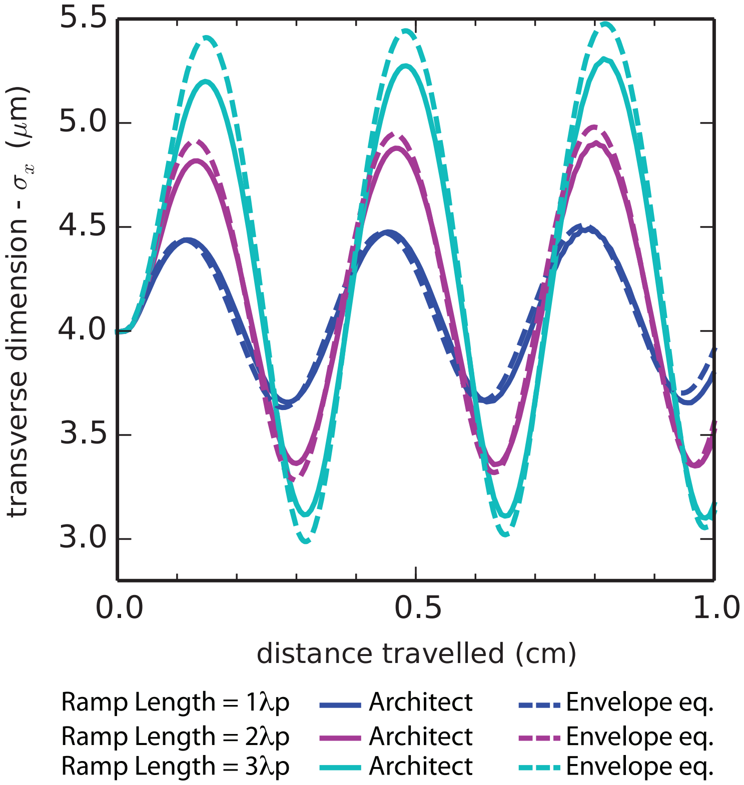

Figure 6.5: Transverse dimension -section 5 of Fig. 6.3- evolution for a bunch travelling through a linearly ramp profile at the capillary entrance with different lengths. Figure from [107].

The exit from the plasma channel constitutes a critical aspect of plasma acceleration. Plasma can spill from the capillary exit, as result of losses in the gas confinement system. Besides, focusing must be provided to a bunch exiting from the plasma to keep the desired compression. These reasons motivate investigations of the effects of a non-zero plasma density after the capillary exit. In Fig. 6.6 the effect of linear ramp lengths L =0,1,2,3 λ_p at the capillary exit on the matched case is shown. A ramp length of L =0 λ_p corresponds to sharp edge transition at the plasma channel end, placed at 1 cm from the channel injection point, and a free bunch expansion in vacuum after the capillary end. A density downramp at the capillary exit can thus slow the bunch expansion. Longer ramps induce a slower bunch expansion. The exiting bunch can be then focused by conventional magnetic lenses. Although the presence of the plasma induces a focusing force that slows down the bunch expansion, the bunch rms-size at fixed distance from the ramp end is greater when the ramp length increases. Indeed, before the ramp end is reached, the bunch has already started to expand while being subject to a decreasing focusing force traveling through longer ramps. To highlight this phenomenon, in Fig 6.7 the same results of Fig. 6.6 are shown, shifting the curves to have the distance from the end of the exit ramp on the horizontal axis.

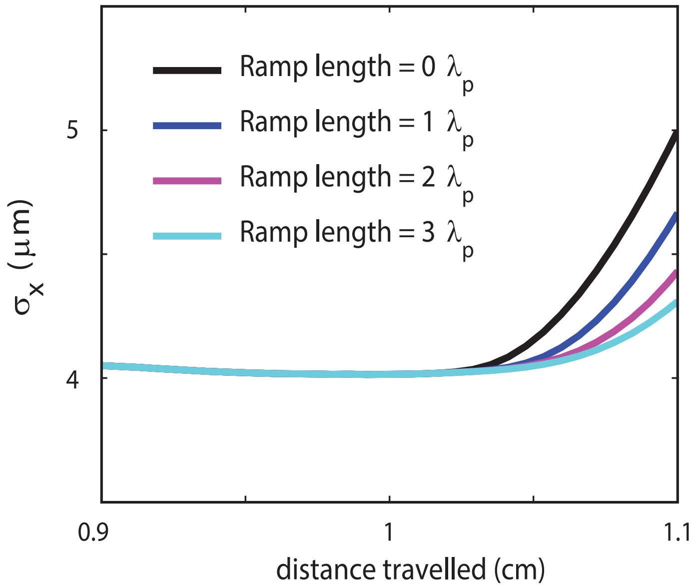

Figure 6.6: Transverse dimension -section 5 of Fig.6.3- evolution for a bunch travelling through a linearly ramp profile at the capillary exit with different lengths. For the sake of clarity only the evolution after 0.9 cm travelled in the plasma channel is shown.

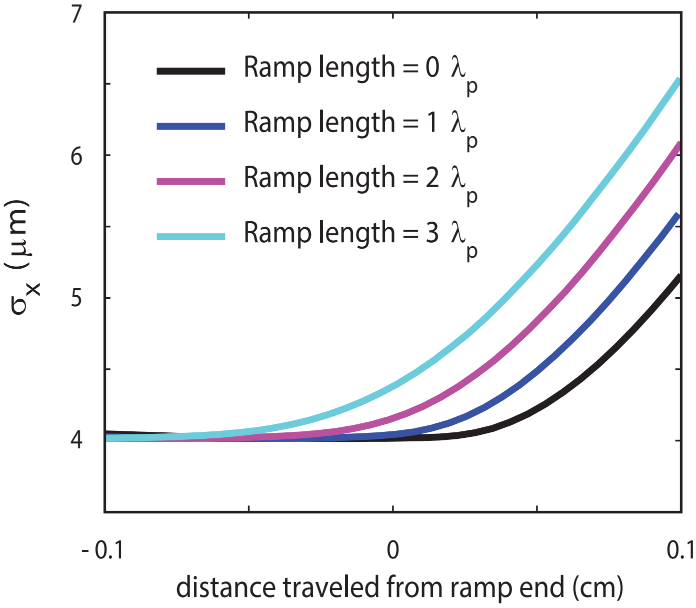

Figure 6.7: Transverse dimension -section 5 of Fig. 6.3- evolution for a bunch travelling through a linearly ramp profile at the capillary exit with different lengths. On the horizontal axis the distance from the end of the ramp at the capillary exit.

6.2.2 Radial parabolic profiles in the capillary density

Another realistic modification to the uniform density capillary model is the assumption of a radial variation of the plasma initial density. With this assumption and also assuming sharp edge transitions at the capillary entrance and exit, the model for the initial plasma electron density $n_e(z,r)$ can be written as:

$$n_e(z,r) = \begin{cases} \left(n_0 - n_{0_{Rc}}\right) \cdot \left(1 - \frac{r^2}{R_c^2}\right) + n_{0_{Rc}} & \text{if } z_{entrance} \leq z \leq z_{exit} \text{ and } r \leq R_c \\ 0 & \text{otherwise} \end{cases} \tag{6.7}$$

where R_c is the radius of the plasma channel, n_0 is the initial electron density at the channel center ($r = 0$), $n_{0_{Rc}}$ is the initial electron density at the channel boundary ($r = R_c$) and $z_{entrance}$, z_{exit} are the longitudinal position of the channel entrance and exit. In Fig.6.8 a), b), c) the effect of the radially parabolic profile is shown assuming a decreasing channel radius (and thus an increasing radial density gradient), respectively $R_c = 500, 250, 125$ μm. The reference case is a uniform density channel and an electron bunch matched to that channel, i.e. the matched case described in Section 6.2. We recall that the initial electron density on axis in that case was $n_0 = 10^{16}\,\text{cm}^{-3}$. An increase in the density at the channel boundary ($n_{0_{Rc}}/n_0 > 1$) with respect to the initial density on axis has a focusing effect, due to higher radial electric fields. Conversely a decrease in the density from the axis ($n_{0_{Rc}}/n_0 < 1$) has a defocusing effect.

In Fig. 6.8 a) it is shown that with $R_c = 500$ μm the oscillation amplitude changes in 1 cm are less than 0.02% with respect to the uniform density channel case if the initial density at the plasma channel boundary decreases by 100% from the axis value. Instead, with ratios $n_{0_{Rc}}/n_0 = 10, 30$ the envelope oscillations amplitude can be maintained nearly constant.

From Fig.6.8 b) it can be inferred that with $R_c = 250$ μm in 1 cm the oscillation amplitude changes rise to a maximum of 0.1% with respect to the uniform density channel case if the initial density at the plasma channel boundary decreases by 100% from the axis value. Density ratios of order $n_{0_{Rc}}/n_0 = 10, 30$ start to actually focus the bunch during the propagation.

Finally, in Fig. 6.8 c) is shown that with $R_c = 125$ μm the maximum oscillation amplitude changes arrive at a 0.35% level in 1 cm if the initial density at the plasma channel boundary decreases by 100% from the axis value. A ratio $n_{0_{Rc}}/n_0 = 30$ can reduce by 1% the mean value of the bunch envelope in 1 cm.

Channel profiles with radially increasing density could in principle be used to provide an additional focusing of plasma-accelerated bunches.

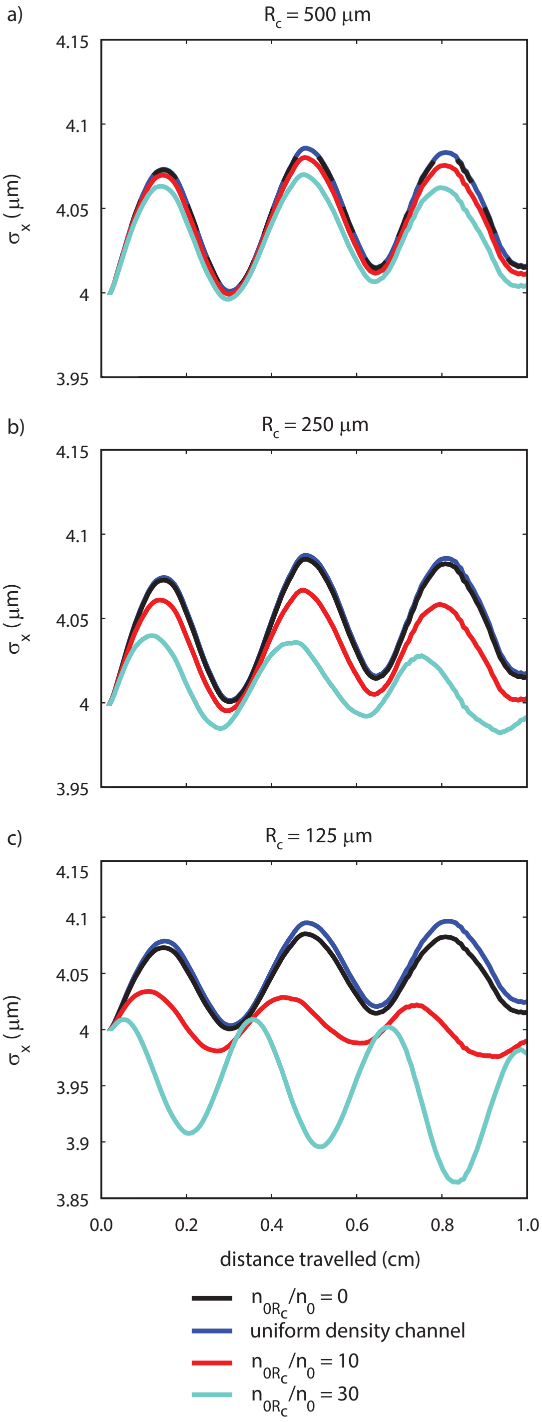

Figure 6.8: Transverse dimension -section 5 of Fig. 6.3- oscillations for bunch with different initial parabolic density profiles (Eq.6.7), varying the channel radius R_c and the initial electron density $n_{0_{R_c}}$ at the channel boundary ($r = R_c$). For the sake of clarity in the a) panel the black curve is dashed.

6.3 An acceleration example: two bunches case

As further example of Architect simulation with parameters of interest for SPARC_LAB facility a one-driver plus one-witness scenario is shown. The witness is injected at a distance 0.5 λ_p (167 µm) from the driver. With a driver charge of 170 pC the on axis peak accelerating field ($E_z(r=0)$) in the witness region is of 3 GV/m and a theoretical transformer ratio of R=3; the witness is instead 10 µm long and has a normalized emittance of ε_n =1 mm-mrad and a total charge of 20 pC. Its transverse dimension has been chosen as the matched one, σ_x =2.4 µm, using Eq.(6.5). The witness dimension is also bound to be well accomodated in the bubble formed by the driver, to avoid interactions with its edge. The witness in its longitudinal direction needs to be totally accommodated in the accelerating half-λ_p region. With some simple considerations on the bubble shape we might say that the rms witness length has to be smaller than $\lambda_p/6$, i.e. less than 20 µm (for n_0 =10^{16} cm^{-3}).

The witness-bunch travelling distance is chosen equal to 6 cm, from Fig.6.9 a) we notice the choice of a 6 cm long plasma permits an energy increase of 150% without loss bunch transverse quality. The witness is well matched and betatron oscillations decay reaching almost no amplitude towards the end of the travelling distance. The witness well conserved transverse and longitudinal shape are well depicted, with its overall surrounding environment, in Fig. 6.10. The transverse normalized emittance (Fig. 6.9 a)) does not have a significant degradation and reaches a maximum value of 1.1 mm-mrad at 3.7 cm and since this point it remains constant. The energy spread, $\Delta\gamma/\gamma$, Fig. 6.9 b), increases almost linearly from its nominal value of 0.1% to 9%, denoting an excessive beam loading (Fig.6.11). From Fig. 6.9 a) we can estimate that the effective overall accelerating field is 0.9 GV/m. Considering that the driver bunch loses a fourth of its initial energy the effective energy transfer ratio from the driver to the witness (effective transformer ratio) is 2.

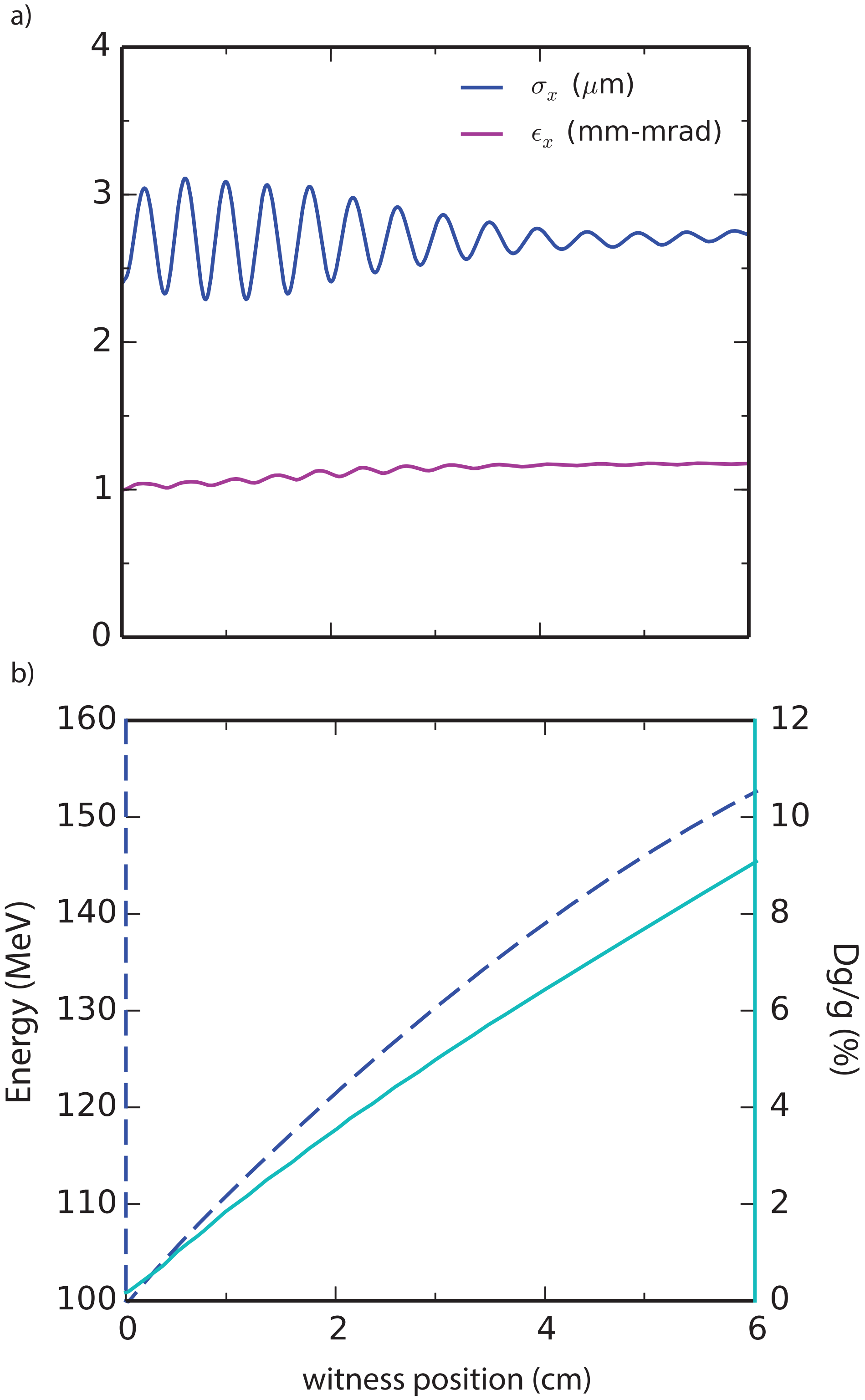

Figure 6.9: Witness-bunch integrated parameters in the case of one-driver of charge 170 pC and one-witness of charge 20 pC placed at 0.5 λ_p of distance. On panel a) rms-σ_x and transverse normalized emittance ε_x. On panel b) the energy -right y-axis- and the energy spread -left y-axis-. Image from [94].

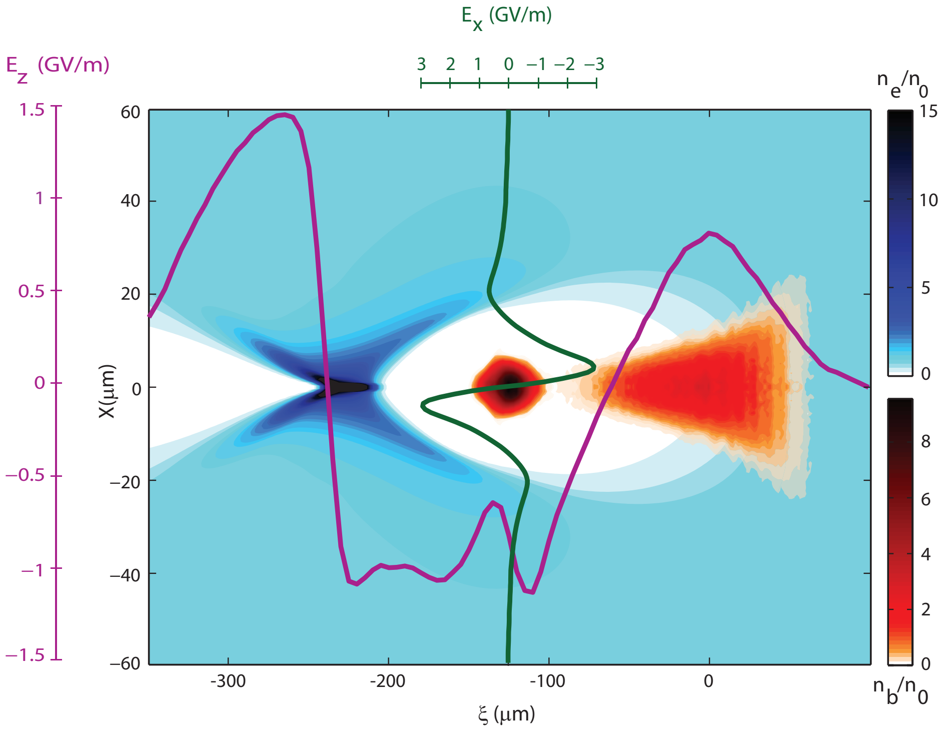

Figure 6.10: Bunch (red scale) and background (blue scale) density map for the case of one-driver plus one-witness, overlapped by on-axis longitudinal electric field on axis E_z (purple line) and by the transverse electric field E_x (green line) at the witness centre of mass position. ξ is the co-moving coordinate $z - ct$ with $ct = 3.47\,\text{cm}$. The density in the region $X < 0$ has been obtained reflecting the map in the $X > 0$ region using the cylindrical symmetry. The same procedure has been used for E_x, but reversing the sign in the $X < 0$ region. Adapted from [94].

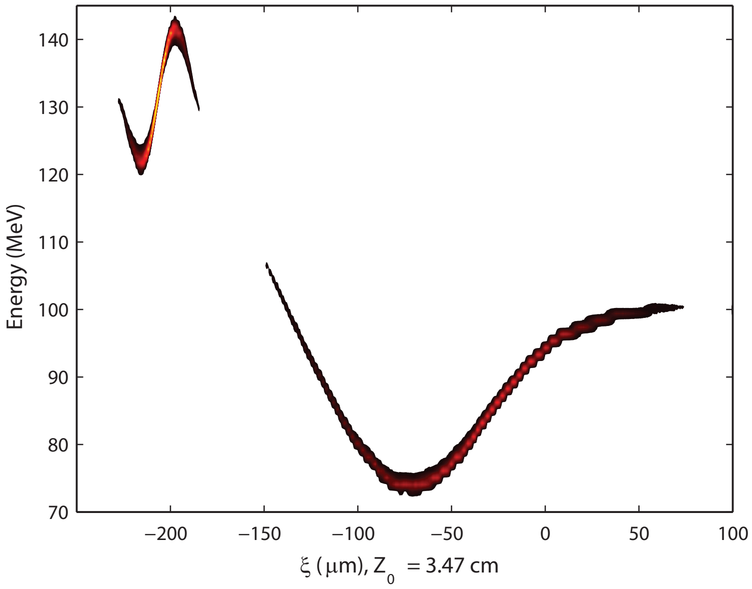

Figure 6.11: Longitudinal phase space distribution for both driver and witness. The witness suffers of an excessive beam loading. ξ is the co-moving coordinate $z - ct$ with $Z_0 = 3.47\,\text{cm}$. Adapted from [94].

6.4 Multibunch PWFA design

The first mechanisms of particle acceleration using the wake field behind a charged particle bunch were proposed for conventional RF accelerators [110, 111]. The maximum energy gains dictated by the limit of 2 for the value of the Transformer Ratio obtainable with symmetric bunches (see Section 3.4 and [77]) led to the study of driver shapes allowing the attainment of higher values of the Transformer Ratio. In particular, driver bunches with a ramped longitudinal shape were studied [112]. To overcome the difficulties in the generation of such bunches, the use of train of bunches with a ramped peak density envelope was proposed [78, 112, 113].

The use of a train of driving bunches was soon considered also by the plasma acceleration community working on the PWFA [19–21, 79]. Although the idea of obtaining higher accelerating fields increasing the number of drivers is appealing, its practical realization presents both experimental and theoretical difficulties. From an experimental point of view, any configuration of interest for a multiple driver scheme (found e.g. with a PIC simulation) implies the need to properly shape the bunch train, i.e. control the distance between the bunches and to transport them up to the injection point with the desired characteristics.

The wakefields excited in PWFA, either in a one-driver-one-witness and in a multi-bunch scheme, need to satisfy some requirements to obtain both high energy gains and high witness bunch quality. To obtain high energy gains the maximum accelerating fields must be sufficiently constant in time and smooth in their spatial profile, but also a good value of the Transformer Ratio (see Section 3.4) is necessary for the drivers to have a longer effective wake-excitation distance. High Transformer Ratio values imply low decelerating fields slowing down the driver, thus a long distance before the drivers lose their energy and a long distance in which the witness is subject to the accelerating fields. The shape of the radial fields which influence the witness are the main factors which influence its emittance evolution. Finally, it must be taken into account that the witness itself modifies the accelerating fields induced by the driver with its own wakefield. This distorsion in the fields induced by the witness, called beam loading, determines the final waveform of the accelerating field in the witness bunch position. Steep slopes in the beam-loaded accelerating field felt by the witness cause high energy spread and a growth of normalized emittance in the witness bunch. In a multibunch scheme the mentioned requirements must be satisfied by the total wakefields excited by drivers. Thus, the study of the wakefields induced by a train of bunches is essential in the design of a multibunch PWFA experiment like COMB.

Some considerations on the initial accelerating wakefield magnitude and waveform can be done using fluid 1D models with a rigid bunch approximation. These fluid models are equivalent to that presented in Chapter 3. In linear regimes multiple driver configurations of interest can be found also analytically by studying the superposition of the single bunches' wakefields, treating them as rigid during the propagation and assuming a rectangular charge density for each bunch [20, 21]. Since similar analytical calculations are less tractable with Gaussian charge densities, numerical integration allows to empirically study the wakefield excitation mechanisms. With the assumption of rectangular charge densities it can be shown that a resonant excitation of the wakefield can be simply obtained with a train of bunches with the same charge, separated by a distance of λ_p. In this configuration each bunch is placed on the decelerating phase of the wake of the previous bunch and the wakefields add up linearly. Since in this scheme both the peak accelerating field behind the drivers and the peak decelerating field inside the drivers linearly add, the trailing bunches are subject to a higher decelerating wake with respect to the previous drivers. Thus the energy transfer to the plasma waves is quicker in the trailing bunches than in the first bunches. This multiple driver scheme would be inefficient for the acceleration of a witness bunch. This inefficiency is quantified by the Transformer Ratio, which in this configuration is near to unity. Since in linear regime the plasma channel works as a monomodal accelerating cavity, the limit of 2 for the Transformer Ratio value for symmetric bunches holds also in PWFA, as shown in Section 3.4. A train of equal bunches satisfies the assumptions of this theorem. Instead, a ramped bunch train configuration, i.e. a sequence of bunches with ramped peak charge density, could in principle obtain higher values of the Transformer Ratio. Multibunch configurations with high values of the Transformer Ratio conversely achieve maximum gradients smaller than those obtainable with simple resonant wakefield excitation [20, 21]. Besides, as discussed in Section 5.5, the focusing fields of such configurations in the linear regimes would be nonlinear with respect to the radial distance from the channel axis, thus a witness bunch would expand and increase its emittance if subject to a wakefield in linear regimes. High values of the Transformer Ratio in a multibunch configuration potentially have high maximum energy gains, but do not guarantee a process of acceleration which maintains an acceptable witness quality.

The use of nonlinear regimes has the advantages of radially linear focusing fields and higher accelerating gradients, but the wakefields induced by Gaussian drivers cannot be found without numerical integration, even in the 1D case and with the rigid bunch assumption. Thus a high Transformer Ratio scheme must be found empirically (see [21]). Attempting to follow the same technique used in the linear regime, each driver should be injected in the accelerating phase of the preceeding driver wakefield, adjusting the charge to have each driver experience a nearly constant decelerating field. Also the distance between the drivers must be found empirically if the degree of nonlinearities and thus the oscillation wavelengths change with each driver.

Although the Transformer Ratio gives some insight in the maximum energy gains of PWFA, it does not take into account the deformation in the wakefields' waveform induced by the witness, i.e. the beam loading. Intuitively, if the particles with nearly same initial energy in different parts of the witness are subject to different magnitudes of the accelerating field, the final energy spread would be large. A witness bunch with length much smaller than the spatial scales in which the accelerating field changes significantly is subject to nearly the same field in each of its sections, minimizing the energy spread. Since realization and controlling of such ultrashort witness bunches is experimentally difficult, the problem of controlling the energy spread must be addressed through the proper shaping and placing of the witness bunch. An optimum witness with respect to beam loading would have a flat accelerating field profile along its length to keep the energy spread under control during the acceleration. Studies on beam loading found witness shapes with optimum beam loading properties in the linear regime [114] and in the blowout regime [115, 116] using the quasi static approximation. The results found in the non linear regime show good agreement with PIC simulations and hold also for Gaussian bunches. There are no similar results in the weakly nonlinear regime, in which the beam loading issue must be addressed empirically.

All the considerations above on the Transformer Ratio, the focusing fields and the beam loading do not take into account the evolution of the drivers during the process of wakefield excitation. The changes in the driver energy and shape influence the excited wakefields and changes in the wakefields influence the stability of the acceleration process.

To show the suitability of Architect to study multibunch schemes, the results of a simulation with a non optimized three driver scheme are presented. The drivers' dimensions at the injection in the capillary are: rms-length $\sigma_z = 35\ \mu$m, rms-spot-size $\sigma_x = 4\ \mu$m. The rms spot size corresponds to the matched beam transverse size corresponding to their normalized emittance $\varepsilon_n = 3$ mm-mrad, computed using Eq.(6.5). Such value of the normalized emittance has been chosen to make the emittance pressure and the plasma focusing force counterbalance each other, to induce an evolution of the drivers less subject to envelope oscillations which would spoil the witness quality through the oscillating wakefields. The driver bunches charge has been set to the values $Q = 30, 90, 150$ pC in order to have a peak charge densities with ratios $1, 3, 5$ respectively. The distance between the driver bunches has been set to 0.7 λ_p. The witness bunch, placed at a distance 0.5 λ_p after the last driver, has charge $Q = 20$ pC and its rms-length $\sigma_z = 8$ μm has been chosen to fit in the bubble created by the last driver, while its rms-spot-size $\sigma_x = 2.4$ μm has been chosen as the matched size, as for the drivers, corresponding to a normalized emittance of $\varepsilon_n = 1$ mm-mrad. All the bunches are injected with relativistic factor $\gamma = 200$ (Energy 100 MeV). For the sake of simplicity the plasma channel model has been chosen to have sharp edge transitions from vacuum to an uniform background density $n_0 = 10^{16}\,\mathrm{cm}^{-3}$. The mesh cell sizes of the simulation are $\Delta z = 1.16\,\mu$m along z and $\Delta r = 0.5\,\mu$m along r; the integration timestep has been set to $\Delta t = 0.66$ fs. The plasma and beam density after the first driver has traveled a distance of 0.1 cm from the capillary entrance are depicted in Fig. 6.12. The corresponding longitudinal electric field on axis E_z is shown in the same Figure. The unloaded value of the Transformer Ratio of the excited wakefields is 2. The witness evolution during the acceleration is shown in Fig 6.13. From Fig. 6.13 a) it can be inferred a final normalized emittance value of $\varepsilon_x = 2$ mm-mrad after 2.5 cm propagation in the plasma channel. From Fig. 6.13 b) it can be inferred an overall energy gain of $\Delta E = 15$ MeV in 2 cm and an overall energy gain of $\Delta E = 20$ MeV in 2.5 cm, corresponding to an average accelerating gradient $E_z = 800$ MV/m, with an energy spread that grows from an injection value $\Delta\gamma/\gamma = 0.1\%$ to the value $\Delta\gamma/\gamma = 1.7\%$. The parameters of the discussed multibunch configuration were chosen in order to keep the final energy spread under 2% and the final normalized emittance under 3 mm-mrad. A higher energy gain could be obtained empirically adjusting the drivers charge and injection distance to obtain a higher accelerating field. Such modification would probably decrease the resulting final witness quality. The attainment of higher energy gains, keeping under control the witness quality needs more investigation and parametric scans, which can be performed using Architect.

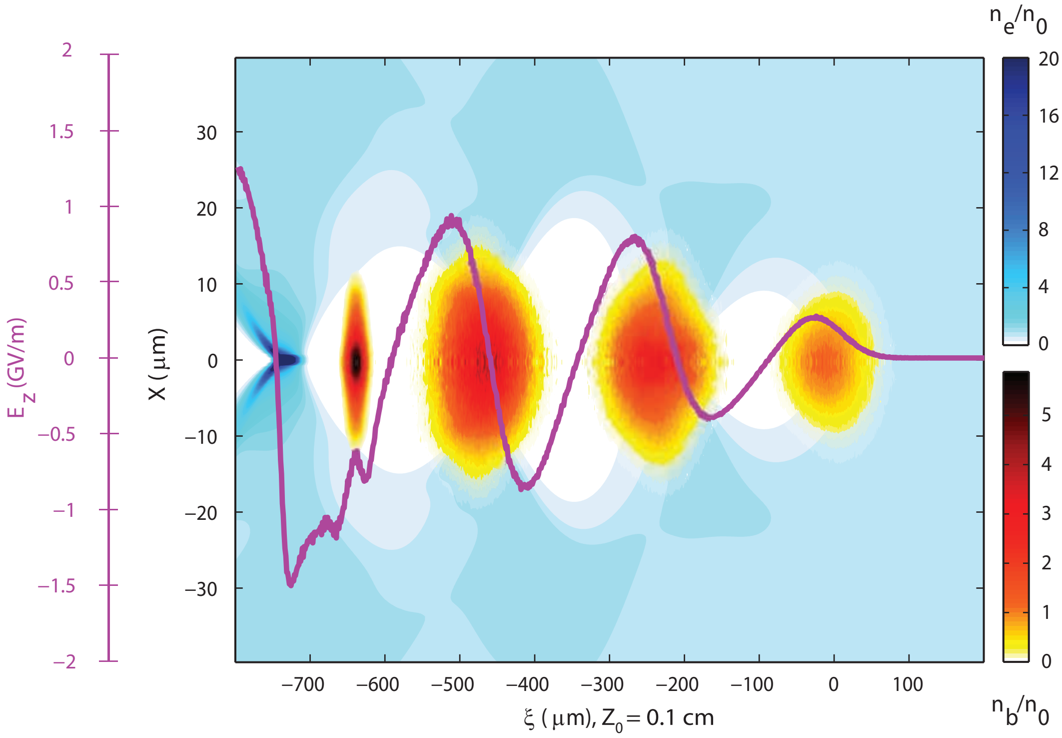

Figure 6.12: Colormap of beam (red scale) and background (blue scale) number density after a distance $Z_0 = 0.1$ cm from the capillary entrance. Superimposed is the longitudinal electric field on axis E_z (purple curve). The horizontal axis represents the distance from the first driver $\xi = z - ct$. The density in the region $X < 0$ has been obtained reflecting the map in the $X > 0$ region using the cylindrical symmetry.

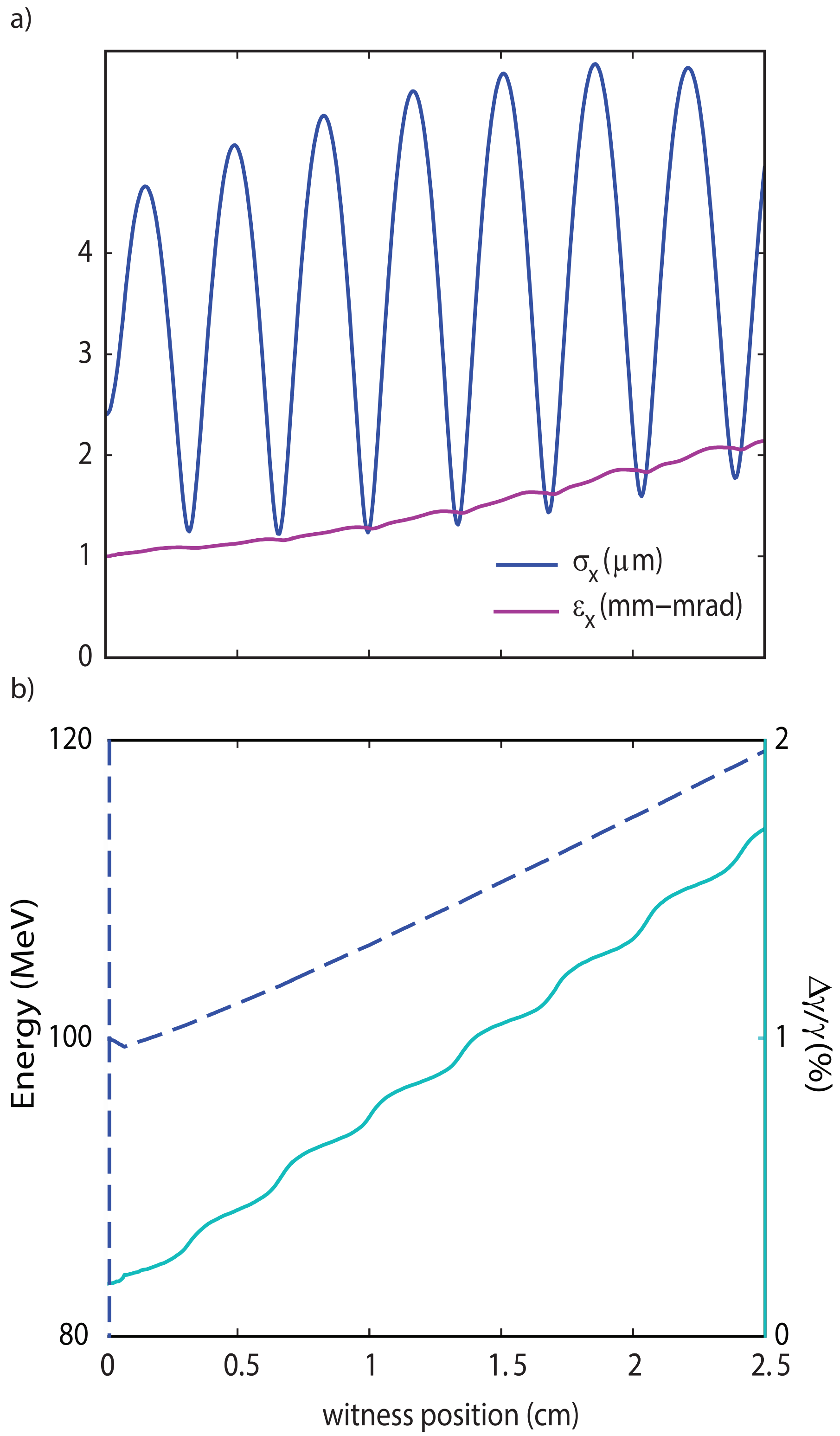

Figure 6.13: Witness-bunch integrated parameters in the multibunch scenario. On panel a) we find: rms-σ_x and transverse normalized emittance ε_x. On panel b) we have both the energy -right y-axis- and the energy spread -left y-axis-

Conclusions

The aim of the thesis has been the development of techinques to efficiently study the Plasma Wakefield Acceleration (PWFA) scheme, to provide tools for online investigation and experimental result analysis. In Chapter 1 the plasma acceleration concept and its potentials have been introduced. The PWFA scheme has been summarily described and a brief review of the main experimental milestones has been given. The main techniques and tools for electron PWFA theoretical and numerical studies have been reviewed. The COMB experiment has been introduced. A brief summary on the foundations of the most used kind of models for the study of multi particle systems, namely the kinetic and fluid models, has been given in Chapter 2, with emphasis on their application to plasma acceleration and PWFA in particular. The definition and the properties of the main quality figures for accelerated beams have been reviewed. The use of a simple 1D fluid model to study the wakefield excitation in PWFA has been discussed in Chapter 3. From this simple, relativistic, numerically integrable model many considerations about the suitability of different plasma oscillations regimes for PWFA experiments, the Transformer Ratio and the cold wave breaking limit can be derived. Transformer Ratio maps have been obtained through the fluid model varying the bunch shapes (triangular, ramped, Gaussian or rectangular), length and peak density. The high Transformer Ratio values found in the case of a ramped driver suggests the use of such a shape for PWFA experiments. A more feasible driver shape with the same properties with respect to the Transformer Ratio is a driver beam composed by a train of electron bunches with a ramped density profile. These properties are some of the main reasons for which such a driver configuration will be used for the COMB experiment. In Chapter 4 the Particle in Cell (PIC) method has been reviewed; the comparison between the semi-analytical fluid model treated in the previous Chapter and a 1D PIC code has been shown. The purely phenomenological addition of a damping term in the fluid model improves its capability to catch the oscillation features up to the weakly nonlinear regimes. Architect, a cylindrically symmetric, time-explicit hybrid kinetic-fluid code for PWFA with high flexibility in the plasma channel definition has been presented in Chapter 5. Its theoretical model has been discussed, as well as comparisons with the 3D full PIC code ALaDyn and the scaling of its simulation time varying the number of beam particles. The hybrid model has been demonstrated to significantly reduce the required simulation time with respect to fully kinetic simulations, making it suitable for fast parametric scans and data analysis. The use of Architect hybrid model for quick investigations has been proved to be suitable up to the weakly nonlinear regime, the regime of interest for the COMB experiment. Applications of Architect for the COMB experiment have been shown in Chapter 6: the study of beam matching conditions to the plasma channel, the effects of linear density ramps at the channel entrance and exit, the effect of radially parabolic density profiles and the study of two-bunch and multi-bunch acceleration scenarios. The use of the envelope equations governing the evolution of a driver bunch transverse size has been proved to accurately reproduce the Architect results, provided that they are applied to the central driver slice. Both the integration of envelope equations and Architect results showed that a linear ramp density at the plasma channel entrance would spoil a matching condition computed assuming a uniform plasma channel density. A linear density ramp at the plasma channel exit has been shown to provide a focusing force on the beam exiting the channel. This focusing could be used in the COMB experiment to keep under control the transverse size of the beam exiting the plasma until it reaches the focusing magnets after the plasma section. A parabolic plasma density profile with increasing density from the channel axis can provide focusing to the bunches as well. Working points of interest for SPARC_LAB facility in two bunches and four bunches configurations have been found using Architect. Future developments concerning the thesis topics include the analytical derivation from kinetic models of the mentioned damping coefficient in the fluid model. At the moment the damping term has only been derived empirically to phenomenologically account for kinetic damping. The integration of a laser envelope model in Architect would make it suitable to study the Laser Wakefield Acceleration scheme as well. The development of a 3D version of Architect would allow to study the effect of asymmetries in the bunches, and the use of a non-cold model would improve the accuracy in catching the shock-like features of the nonlinear regimes. Further studies on the applicability of hybrid kinetic-fluid models for PWFA like the one used by Architect or even more sophisticated will be possible on the basis of the discussed results. Finally, more systematic studies for the COMB experiment will be possible through this quick accurate tool.

Appendix A

Plasma Parameters

A brief review of the main plasma parameters is reported. For a more detailed discussion of their derivation and physical meaning refer to any plasma textbook, as [51, 52, 117]. Without loss of generality, if not otherwise specified, the derivation of these parameters always assumes $Z = 1$.

A.1 Debye Length

Electric charges in plasmas tend to collectively screen perturbations to the global neutrality of the plasma. The order of magnitude of the screening distance is given by Debye length λ_D. Such length can be estimated computing the equilibrium potential of a point charge q placed in a initially neutral plasma. Denoting with n_e and n_i the electron and ion densities, the electrostatic potential Φ can be found integrating Poisson equation:

$$\nabla^2\Phi(\boldsymbol{x}) = -\frac{1}{\varepsilon_0}[e(n_i(\boldsymbol{x}) - n_e(\boldsymbol{x})) + q\delta(\boldsymbol{x} - \boldsymbol{x}_q)], \tag{A.1}$$

where $\boldsymbol{x}_q$ is the position of the charge q Assuming a vanishing potential at infinite distance from the charge q, at equilibrium the electron and ion densities are given by the Boltzmann distribution [117]:

$$n_e(\boldsymbol{x}) = n_{e0}\exp\left(\frac{e\Phi(\boldsymbol{x})}{k_B T_e}\right),\ n_i(\boldsymbol{x}) = n_{i0}\exp\left(\frac{-e\Phi(\boldsymbol{x})}{k_B T_i}\right), \tag{A.2}$$

where n_{e0} and n_{e0} are the electron and ion initial densities and T_e and T_i are the electron and ion equilibrium temperatures. The potential at distances where the electrostatic energy is much smaller than thermal energy, i.e. $e\Phi((x)) \ll T_{e,i}$ can be found substituting Eqs.(A.2) in Eq.(A.1), expanding in series the electron and ion densities:

$$\nabla^2\Phi(\boldsymbol{x}) - e\left[n_{e0}\left(1+\frac{e\Phi(\boldsymbol{x})}{k_B T_e}\right) - n_{i0}\left(1-\frac{e\Phi(\boldsymbol{x})}{k_B T_i}\right)\right] = -\frac{1}{\varepsilon_0}[q\delta(\boldsymbol{x}-\boldsymbol{x}_q)]. \tag{A.3}$$

Assuming initial neutrality, i.e. $n_{e0} = n_{i0} = n_0$, Eq.(A.4) can be written as:

$$\nabla^2\Phi(\boldsymbol{x}) - \frac{1}{\lambda_D^2}\Phi(\boldsymbol{x}) = -\frac{1}{\varepsilon_0}[q\delta(\boldsymbol{x})], \tag{A.4}$$

where the Debye length λ_D has been with

$$\frac{1}{\lambda_D^2} = \frac{e^2 n_{e0}}{\varepsilon_0 k_B T_e} + \frac{e^2 n_{i0}}{\varepsilon_0 k_B T_i}. \tag{A.5}$$

In plasma acceleration cases $T_e \gg T_i$, thus Debye length in Eq.(A.5) reduces to

$$\lambda_D = \sqrt{\frac{\varepsilon_0 k_B T_e}{e^2 n_0}}. \tag{A.6}$$

Due to the spherical symmetry of the problem, the electrostatic potential is only function of the distance $r = \|\boldsymbol{x}-\boldsymbol{x}_q\|$ from the charge q. Integrating the inhomogeneous Helmholtz equation (A.4) assuming, as mentioned, vanishing potential at infinite distance from q the screened potential of q is found:

$$\Phi(r) = \frac{q}{4\pi\varepsilon_0 r}e^{-\frac{r}{\lambda_D}} \tag{A.7}$$

From Eq.(A.7) the Debye length can be inferred as the characteristic length beyond which the potential of a perturbation in the charge neutrality is screened by the plasma. Such screening does not occur if the studied ionized system of particles does not extend for length scales $\gg \lambda_D$.

Quantitatively, the value of the Debye length (Eq.(A.6)) is given by

$$\lambda_D(\mathrm{m}) \approx 7.43\sqrt{\frac{\mathrm{T_e(eV)}}{\mathrm{n_0(cm^{-3})}}}. \tag{A.8}$$

A.2 Plasma coupling parameter

The collective behaviour of a plasma can be quantified by the ratio of the mean thermal energy and the mean electrostatic energy between two particles:

$$\Lambda = \frac{k_B T}{\frac{e^2}{4\pi\varepsilon_0 d}} = \frac{4\pi\varepsilon_0 k_B T}{e^2 n^{1/3}}, \tag{A.9}$$

where $d = n^{-1/3}$ is the mean inter-particle distance. In a plasma of average density n, the average number of particles in a cube with side equal to the Debye length λ_D ("Debye cube") is given by $N = n\lambda_D$. Recalling the definition of the Debye length (Eq.(A.6)), the plasma coupling parameter is related to N by

$$\Lambda = 4\pi N^{\frac{2}{3}}. \tag{A.10}$$

From Eq.(A.10) it can be inferred that when $\Lambda \ll 1$ the number of particles in a Debye cube is low, the electrostatic energy between two particles is much greater than the average thermal energy and the motion of a particle is stongly dependent on the nearest particles' motion. Since, in other words, in these systems the coupling between near particles is strong, they are referred to as strongly *coupled systems*. On the contrary, when $\Lambda \gg 1$ the Debye cube is much populated and collective behaviour dominates over the binary electrostatic interaction, thus the system is referred to as *weakly coupled*.

A.3 Plasma frequency

Debye length quantifies a spatial scale for the response to a static perturbation to the plasma neutrality. The time scale for the response to a perturbation of the neutrality of a plasma is given by the electron plasma frequency ω_p. A simple derivation of its expression is obtained considering an initially uniform plasma with ion and electron density n_0. The ions are considered at rest in the timescales of interests for electron plasma oscillations. If a sheet of electrons of surface S is displaced by a distance $x \ll \sqrt{S}$ from its equilibrium position, a positively charged sheet of equal size in its former position is formed. Both the sheets contain a net charge with absolute value en_0Sx. Between them an electric field $E = enx/\varepsilon_0$ is created by the charge unbalance. Assumig that the resulting field is low enough not to accelerate electrons to relativistic velocities, the motion of an electron in this field is described by:

$$m_e \frac{d^2x}{dt^2} = -\frac{e^2 n_0 x}{\varepsilon_0} \tag{A.11}$$

In these hypotheses a harmonic variation of the electron sheet position (and thus of its density) and self-consistently of the electric field is obtained:

$$\frac{d^2x}{dt^2} + \omega_p^2 x = 0 \tag{A.12}$$

with the characteristic frequency of small amplitude electron oscillations in the plasma

$$\omega_p = \sqrt{\frac{e^2 n_0}{m_e \varepsilon_0}}. \tag{A.13}$$

Plasma frequency constitutes the timescale at which the plasma responds to charge perturbations. Collective oscillations in the studied plasma cannot be observed if the observation time is smaller than ω_p^{-1}.

Recalling the definition of electron temperature $k_B T_e = \frac{1}{2} m_e v_{th}^2$, it can be inferred from Eqs.(A.13, A.6) that average distance traveled by an electron at thermal speed v_{th} in a time interval equal to the inverse of the plasma frequency is the Debye length:

$$\lambda_D = v_{th} \omega_p^{-1}. \tag{A.14}$$

From the plasma frequency the plasma wavelength λ_p can be defined as the wavelength of plasma small amplitude electron oscillations:

$$\lambda_p = \frac{2\pi c}{\omega_p}. \tag{A.15}$$

Quantitatively, electron plasma frequency (Eq.(A.13)) and plasma wavelength (Eq.(A.15)) are given by

$$f_p(\mathrm{Hz}) = \omega_\mathrm{p}/2\pi \approx 8.98 \cdot 10^3 \sqrt{\mathrm{n_0(cm^{-3})}},\ \lambda_\mathrm{p}(\mu\mathrm{m}) = \frac{3.3 \cdot 10^{10}}{\sqrt{\mathrm{n_0(cm^{-3})}}}. \tag{A.16}$$

As is shown in Sec. 3.2, when the perturbation in the plasma density is greater than the initial plasma density, the electron velocities reach relativistic values, and their increased inertia makes them oscillate at frequencies lower than the electron plasma frequency ω_p. A more formal derivation of the electron plasma frequency expression can be found considering Gauss law and the fluid equations for the electrons in a cold plasma. Since the plasma frequency is a natural electrostatic oscillation frequency for small perturbations from the equilibrium, non-relativistic velocities must be assumed to derive its expression, thus the needed equations can be cast in the form:

$$\begin{aligned}
\frac{\partial n_e}{\partial t} + \nabla \cdot (n_e \boldsymbol{v}_e) &= 0 \\
\frac{\partial \boldsymbol{v}_e}{\partial t} + \boldsymbol{v}_e \cdot \nabla \boldsymbol{v}_e &= -\frac{e}{m_e}\boldsymbol{E} \\
\nabla \cdot \boldsymbol{E} &= -\frac{e}{\varepsilon_0}(n_e - n_i).
\end{aligned} \tag{A.17}$$

Assuming again immobile ions in the timescales of interests for the searched oscillations, initial neutrality and a uniform background density, the previous equations can be simplified further linearizing them around the equilibrium configuration ($n_e \approx n_i = n_0$, $\boldsymbol{v_e} = 0$, $\boldsymbol{E} = 0$). Denoting with a subscript 1 the quantities at the first order of perturbation, the first order perturbation equations derived from Eqs.(A.17) are [52]:

$$\begin{aligned}
\frac{\partial n_{e1}}{\partial t} + n_0 \nabla \cdot \boldsymbol{v}_{e1} &= 0 \\
\frac{\partial \boldsymbol{v}_{e1}}{\partial t} &= -\frac{e}{m_e}\boldsymbol{E_1} \\
\nabla \cdot \boldsymbol{E_1} &= -\frac{e}{\varepsilon_0} n_{e1}.
\end{aligned} \tag{A.18}$$

From Eqs.(A.19) the harmonic equations for the plasma electron density and velocities at the first order of perturbation (which are predictive in the case of small perturbations around the equilibrium) can be found:

$$\begin{aligned}
\frac{\partial^2 n_{e1}}{\partial t^2} + \omega_p^2 n_{e1} &= 0 \\
\frac{\partial^2 \boldsymbol{v}_{e1}}{\partial t^2} + \omega_p^2 \boldsymbol{v}_{e1} &= 0 \\
\frac{\partial^2 \boldsymbol{E}_1}{\partial t^2} + \omega_p^2 \boldsymbol{E}_1 &= 0.
\end{aligned} \tag{A.19}$$

A.4 Collision frequencies

In the plasmas of interest for this thesis work, the Coulomb collision frequencies are negligible with respect to the plasma frequency f_p, as shown in Section A.5. In this section an estimate of the highest collision frequency, i.e. the one referred to the electron-ion collisions, is estimated. Due to the significant difference between the ion and the electron mass (a ratio of at least 1840), in a fully ionized, non-relativistic plasma the highest collision frequencies are the ones referred to the collisions between the electrons and the ions. Such electron-ion collision frequency ν_{ei} can be estimated from Rutherford's scattering angle relation [118], treating the ion as it had infinite mass:

$$\tan\left(\frac{\theta}{2}\right) = \frac{Ze^2}{4\pi\varepsilon_0 m_e v^2 b}, \tag{A.20}$$

where θ is the deflection angle, Z is the ion atomic number, m_e is the electron mass, v is the incident electron velocity and b is the impact parameter (see Fig. A.1). In a plasma the electron incident velocity is of the order of the thermal velocity. The same result holds with the assumption of finite ion mass m_i, provided that the electron mass and velocity are substituted by the reduced mass ($\frac{m_e m_i}{m_e+m_i}$) and the relative velocity of the electron with respect to the ion. The deflection angle θ as well is defined in the center of mass reference frame, which typically moves with the ion if the electron velocity is of the same order of magnitude.

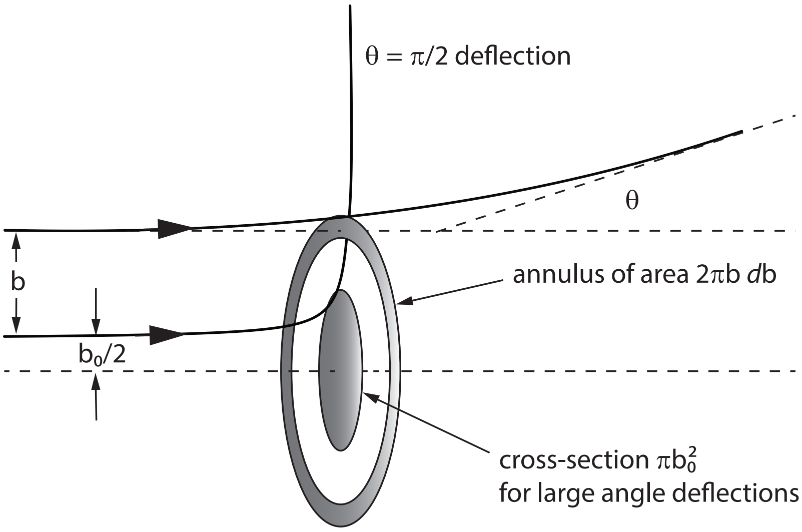

Figure A.1: Rutherford scattering, highlighting the cross-section for large angle collisions and the annulus corresponding to the impact parameter b.

Defining the distance

$$b_0 = \frac{\frac{Ze^2}{4\pi\varepsilon_0}}{\frac{1}{2}m_e v^2}, \tag{A.21}$$

i.e. the distance at which the electrostatic interaction energy is equal to the electron kinetic energy, Eq.(A.22) can be written as:

$$\tan\left(\frac{\theta}{2}\right) = \frac{b_0}{2b}, \tag{A.22}$$

to highlight that the value $b_0/2$ represents for the impact parameter b the threshold beyond which the resulting deflection angles are $\theta \leq \pi/2$. Thus, the total cross-section for *large angle* collisions, i.e. $b \leq b_0$, is the area of the circle with radius b_0 (shown in Fig. A.1):

$$\sigma_{\text{large angle}} = \pi b_0^2; \tag{A.23}$$

the area in which *small angle* collisions occur, i.e. $b \geq b_0$, is the area outside such circle. The total cross-section for the deflection angle variance in a single collision is obtained integrating the infinitesimal area of the annuli of radius b, weighted by θ^2:

$$\sigma_{\text{small angle}} = \int_{b_0}^{\infty} 2\pi b \theta^2 db. \tag{A.24}$$

For small angle collisions Eq.(A.22) yields the relation $\theta = b_0/b$, which allows to write the integral in Eq.(A.24) as:

$$\sigma_{\text{small angle}} = \int_{b_0}^{\infty} 2\pi \frac{b_0^2}{b} db. \tag{A.25}$$

The integral in Eq.(A.26) diverges. A more realistic result for the collisions in a plasma can be obtained taking into account that in the ion field beyond a Debye length λ_D from the ion position would be screened by the other charges (see Section A.1). Thus for a simple estimate λ_D can be chosen as the upper limit of the integral in Eq.(A.26), yielding

$$\sigma_{\text{small angle}} = \int_{b_0}^{\lambda_D} 2\pi \frac{b_0^2}{b} db = 2\pi b_0^2 \ln\left(\frac{\lambda_D}{b_0}\right) = 8 \ln\left(\frac{\lambda_D}{b_0}\right) \sigma_{\text{large angle}}. \tag{A.26}$$

Thus, small angle collisions are much more frequent than large angle collisions if $\lambda_D \gg b_0$. In the case of a hydrogen plasma ($Z = 1$) with ion density n_0, using the expression for the electron thermal velocity $v = \sqrt{k_B T_e/m_e}$[1] and Eqs.(A.21, A.6) the relation $b_0 = 1/2n_0\lambda_D^2$. Thus the condition to have a large argument in the logarithm of Eq.(A.26) reduces to $n_0\lambda_D^3 \gg 1$, i.e. a large number of particles N in the Debye cube (see Section A.2). Thus in a weakly coupled plasma small angle collisions are much more frequent than large angle collisions. The logarithm in Eq.(A.26), also called the Coulomb logarithm, makes the order of magnitude of $\sigma_{\text{small angle}}$ weakly dependent on the ion atomic number[2], the density and the temperature. The choice of the impact

---

[1] valid for a Maxwellian distribution of the electron velocities.

[2] With $Z > 1$ the small angle collisions would be even more frequent.

parameter threshold b_0 for small angle deflections as well does not significantly influence the order of magnitude of the small angle deflection cross-section.

The significantly higher frequency of the small angle deflections implies that the total angle deflection to which an electron is subject results mainly by the cumulative effect of small angle deflections. Since the impact parameter and the incident impact angle at each collision can be considered random, on average the total deflection angle $\langle\theta\rangle$ is zero. Thus the variance of the total deflection angle $\langle\theta^2\rangle_{\text{total}}$ for small angle deflections can be used to define the collision frequency as the inverse of the time required to have $\langle\theta^2\rangle_{\text{total}} = 1$, i.e. a total deflection angle variance equal to unity. Since the considered collision deflection angles can be considered uncorrelated, the variance of the single collision deflection angles add up in the total deflection angle variance. The total deflection angle variance is thus the product of the flux of particles relative to the electron and the cross-section of small angle collisions. An electron moving with velocity v in a plasma of density n_0 is subject to a relative flux of particles per unit time $n_0 v$. The collision frequency is thus found by the equality

$$1 = \langle\theta^2\rangle_{\text{total}} = \frac{1}{\nu_{ei}} n_0 v \, \sigma_{\text{small angle}}. \tag{A.27}$$

Finally, using Eqs.(A.27, A.21, A.6) and the relation $v = \sqrt{k_B T_e / m_e}$ for the thermal velocity, the electron-ion collision frequency is given by

$$\nu_{ei} = 2\pi b_0^2 n_0 v \ln\left(\frac{\lambda_D}{b_0}\right) = \frac{2}{\pi} \frac{Z^2 e^4 n_0}{\varepsilon_0 m_e^{1/2} \left(k_B T_e\right)^{3/2}} \ln\left(\frac{\lambda_D}{b_0}\right). \tag{A.28}$$

Quantitatively, the electron-ion collision frequency in Eq.(A.29) is given by

$$\nu_{ei}(Hz) = 2.91 \cdot 10^{-6} \frac{Z^2 n_0(\text{cm}^{-3})}{T_e(\text{eV})} \ln\left(\frac{\lambda_D}{b_0}\right). \tag{A.29}$$

The calculation of the electron-electron, ion-ion and ion-electron collision frequencies, which requires a more sophisticated statistical treatment that takes into account the motion of the center of mass of the single collisions, can be found in [119]. The result of this calculation is that the electron-ion collision frequency is the highest of such frequencies. In a relativistic plasma as well the collision frequencies involving relativistic particles are smaller than the non-relativistic electron-ion collision frequency. This can be explained heuristically by the high relativistic γ factor, which increases the electron momentum and thus decreases the deflection angle at each collision. A formal derivation of this result can be found in [120].

A.5 Plasma parameters in the COMB experiment

Tentative parameters for the hydrogen ($Z = 1$) plasma channel in the COMB experiment (see Section 6.1) are:

$$\begin{aligned} n_0 &= 10^{16}\,\mathrm{cm}^{-3}, \\ T_e &= 4\,\mathrm{eV}, \end{aligned} \tag{A.30}$$

from which the corresponding parameters defined in Sections A.1, A.2, A.3, A.4 can be computed, yielding:

$$\begin{aligned} \lambda_D &= 0.15\,\mu\mathrm{m}, \\ \Lambda &= 2 \cdot 10^5, \\ f_p &= 0.9\,\mathrm{THz}, \\ \omega_p &= 5.65\,\mathrm{Trad/s}, \\ \lambda_p &= 334\,\mu\mathrm{m}, \\ \nu_{ei} &= 88.7\,\mathrm{GHz}. \end{aligned} \tag{A.31}$$

Appendix B

Numerical methods for PIC codes

The numerical techniques used in Architect for the particle advance in the phase space ("Boris pusher") and the electromagnetic field advance in time (Finite Difference Time Domain) are briefly reviewed with no presumption of completeness in the discussion of their derivation and accuracy. More details can be found in [35, 82, 84].

B.1 Boris particle pusher

The leapfrog scheme with Boris' method to perform the rotation of the macroparticle momentum vector in the relativistic case is briefly recalled, following [35, 82]. The equation of motion integrated by the particle mover routine is:

$$\frac{d\mathbf{u}}{dt} = \frac{q_s}{m_s c}\left[\mathbf{E} + \boldsymbol{\beta} c \times \mathbf{B}\right], \tag{B.1}$$

where $\boldsymbol{u} = \boldsymbol{\beta}(1 - \|\boldsymbol{\beta}\|^2)^{-\frac{1}{2}}$ is the normalized momentum of the macroparticle, q_s and m_s are the charge and the mass of the macroparticle of species s. The fields $\mathbf{E}$ and $\mathbf{B}$ acting on the macroparticle are extrapolated from the grid, as described in Sec. 4.1.2. The time steps will be denoted in the following by the index n.

For the sake of simplicity the leapfrog scheme to integrate Eq.(B.1) with $\mathbf{B} = 0$ is first discussed. The positions and the momenta are sampled with a temporal staggering of

$\Delta t/2$. The integration scheme will be then given by:

$$\begin{aligned} \mathbf{u}^{n+1} &= \mathbf{u}^{n-1} + \frac{q_s}{m_s c}\mathbf{E}^{n+1/2}\frac{\Delta t}{2} \\ \gamma^{n+1} &= \sqrt{1 + \|\mathbf{u}^{n+1}\|^2} \\ \mathbf{x}^{n+1/2} &= \mathbf{x}^{n-1/2} + \frac{\mathbf{u}^{n+1}}{\gamma^{n+1}}\Delta t. \end{aligned} \tag{B.2}$$

The scheme introduces an error scaling as Δt^3. To account for both the speed change due to the electric field and the rotation due to a magnetic field $\mathbf{B} \neq 0$, the leapfrog scheme is modified as first proposed by Boris in [82]. The normalized momentum changed by the electric field in half time timestep is defined as

$$\mathbf{u}^- = \mathbf{u}^n + \frac{q_s}{m_s c}\mathbf{E}^{n+1/2}\frac{\Delta t}{2}, \tag{B.3}$$

then it is rotated by means of the magnetic field, obtaining the rotated momentum vector $\mathbf{u}^+$, i.e.

$$\begin{aligned} \mathbf{u}' &= \mathbf{u}^- + \mathbf{u}^- \times \mathbf{t} \\ \mathbf{u}^+ &= \mathbf{u}^- + \mathbf{u}' \times \mathbf{s}, \end{aligned} \tag{B.4}$$

where

$$\begin{aligned} \mathbf{t} &= \frac{q_s}{m_s}\frac{\mathbf{B}^{n+1/2}\Delta t}{2\gamma^{n+1/2}} \\ \mathbf{s} &= \frac{2\mathbf{t}}{(1 + \|\mathbf{t}\|^2)} \\ \gamma^{n+1/2} &= \sqrt{1 + \|\mathbf{u}^-\|^2}. \end{aligned} \tag{B.5}$$

Since in the FDTD scheme the evolved fields are typically staggered by half a timestep (see Sec. B.2), the magnetic field in the previous equations defined at the timestep $n + 1/2$ must be interpolated between its values at timesteps n and $n + 1$. The previous scheme constitutes Boris method, which conserves momentum and rotates its vector by an angle of $\theta = -2\arctan\left(\frac{q_s}{m_s}\frac{\|\mathbf{B}^{n+1/2}\|\Delta t}{2\gamma^{n+1/2}}\right)$ around the magnetic field axis with an error in θ scaling as Δt^3.

The rotated momentum $\mathbf{u}^+$ is finally accelerated in a half timestep, and the macroparticle position $\mathbf{x}$ can be advanced as in the leapfrog scheme:

$$\begin{aligned}\mathbf{u}^{n+1} &= \mathbf{u}^+ + \frac{q_s}{m_s c}\mathbf{E}^{n+1/2}\frac{\Delta t}{2} \\ \gamma^{n+1} &= \sqrt{1+\|\mathbf{u}^{n+1}\|^2} \\ \mathbf{x}^{n+1/2} &= \mathbf{x}^{n-1/2} + \frac{\mathbf{u}^{n+1}}{\gamma^{n+1}}\Delta t.\end{aligned} \tag{B.6}$$

B.2 Finite Difference Time Domain scheme

One of the most widely used explicit schemes to solve Maxwell equations in PIC codes is the Finite Difference Time Domain (FDTD) scheme [35, 84]. The electromagnetic fields are advanced in time discretizing Maxwell equations, put in the evolution equation form:

$$\begin{aligned}\frac{\partial \mathbf{B}}{\partial t} &= -\nabla \times \mathbf{E} \\ \frac{\partial \mathbf{E}}{\partial t} &= c^2\nabla \times \mathbf{B} - \frac{1}{\varepsilon_0}\mathbf{J}.\end{aligned} \tag{B.7}$$

The divergence equations given by

$$\begin{aligned}\nabla \cdot \mathbf{B} &= 0 \\ \nabla \cdot \mathbf{E} &= \frac{\rho}{\varepsilon_0}\end{aligned} \tag{B.8}$$

are initial conditions on the fields which hold also at $t > 0$, provided that continuity equation holds:

$$\nabla \cdot \mathbf{J} = -\frac{\partial \rho}{\partial t}. \tag{B.9}$$

This can be proven deriving with respect of time Eqs.(B.8).

For the sake of simplicity the FDTD scheme equations and the corresponding grid in the following are referred to a cartesian reference system. The fields and the sources are physically positioned in a cell pattern called the Yee cell (see Fig. B.1). Electric and magnetic fields are staggered by half mesh interval. Electric fields lie in the middle of the cell edges, while the magnetic fields lie on the center of the cell faces. The centering of the current densities is the same of the electric fields. The fields are staggered also with respect of time, by a half timestep, as in a leapfrog scheme involving the electromagnetic fields. With this choice the scheme is second order accurate with respect of time and space. The time centering of the current densities is the same of the magnetic fields (see Fig. B.2). With this distribution of the fields and the sources on the Yee cell, Eqs.(B.7)

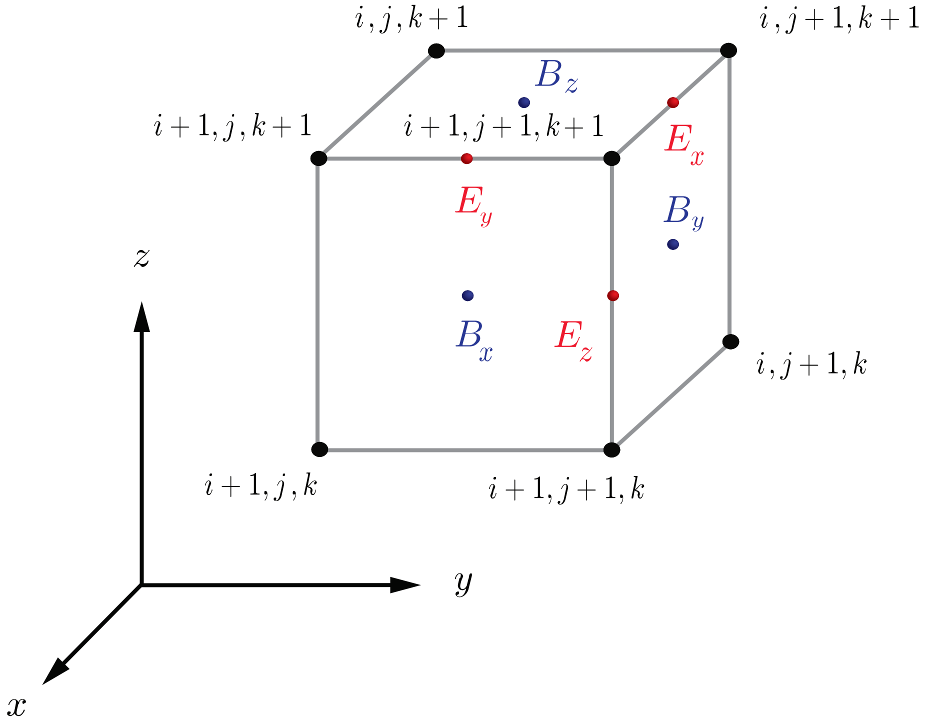

Figure B.1: Yee lattice cell in FDTD method.

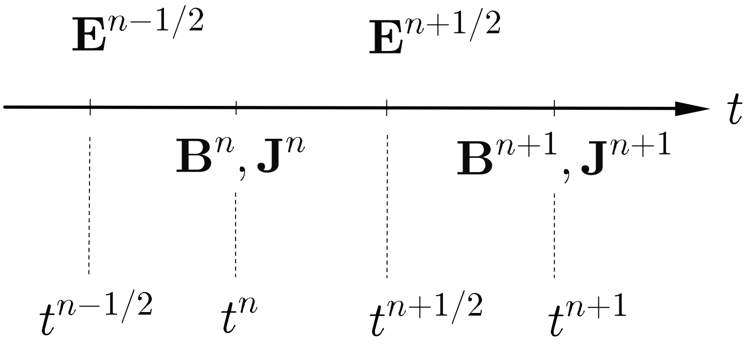

Figure B.2: Time centering of the quantities in the FDTD method. Note that the electric fields and the magnetic fields lie on staggered timesteps.

can be discretized using the finite differences in central form. Denoting the value of a quantity f at position and time $(i\Delta x, j\Delta y, k\Delta z, n\Delta t)$ with $f^n_{i,j,k}$, where Δx, Δy, Δz and Δt as spatial mesh cell sizes and integration timestep, the involved derivatives are approximated up to the first order by:

$$\begin{aligned}
\left(\frac{\partial f}{\partial t}\right)^n_{i,j,k} &\approx \frac{1}{\Delta t}\left(f^{n+1/2}_{i,j,k} - f^{n-1/2}_{i,j,k}\right), \\
\left(\frac{\partial f}{\partial x}\right)^n_{i,j,k} &\approx \frac{1}{\Delta x}\left(f^{n}_{i+1/2,j,k} - f^{n}_{i-1/2,j,k}\right), \\
\left(\frac{\partial f}{\partial y}\right)^n_{i,j,k} &\approx \frac{1}{\Delta y}\left(f^{n}_{i,j+1/2,k} - f^{n}_{i,j-1/2,k}\right), \\
\left(\frac{\partial f}{\partial z}\right)^n_{i,j,k} &\approx \frac{1}{\Delta z}\left(f^{n}_{i,j,k+1/2} - f^{n}_{i,j,k-1/2}\right).
\end{aligned} \tag{B.10}$$

Thus Maxwell equations are discretized as:

$$\begin{aligned}
\frac{E^{n+1/2}_{x_{i+1/2,j,k}} - E^{n-1/2}_{x_{i+1/2,j,k}}}{\Delta t} &= c^2\left[\frac{B^n_{z_{i+1/2,j+1/2,k}} - B^n_{z_{i+1/2,j-1/2,k}}}{\Delta y} - \frac{B^n_{y_{i+1/2,j,k+1/2}} - B^n_{y_{i+1/2,j,k-1/2}}}{\Delta z}\right] + \\
&- \frac{J^n_{z_{i+1/2,j,k}}}{\varepsilon_0} \\
\frac{E^{n+1/2}_{y_{i,j+1/2,k}} - E^{n-1/2}_{x_{i,j+1/2,k}}}{\Delta t} &= c^2\left[\frac{B^n_{x_{i,j+1/2,k+1/2}} - B^n_{x_{i,j-1/2,k-1/2}}}{\Delta z} - \frac{B^n_{z_{i+1/2,j+1/2,k}} - B^n_{y_{i-1/2,j+1/2,k}}}{\Delta x}\right] + \\
&- \frac{J^n_{y_{i,j+1/2,k}}}{\varepsilon_0} \\
\frac{E^{n+1/2}_{z_{i,j,k+1/2}} - E^{n-1/2}_{z_{i,j,k+1/2}}}{\Delta t} &= c^2\left[\frac{B^n_{y_{i+1/2,j,k+1/2}} - B^n_{y_{i-1/2,j,k+1/2}}}{\Delta x} - \frac{B^n_{z_{i,j+1/2,k+1/2}} - B^n_{x_{i,j-1/2,k+1/2}}}{\Delta y}\right] + \\
&- \frac{J^n_{z_{i,j,k+1/2}}}{\varepsilon_0}
\end{aligned} \tag{B.11}$$

$$\begin{aligned}
\frac{B^{n+1}_{x_{i,j+1/2,k+1/2}} - B^{n-1}_{x_{i,j+1/2,k+1/2}}}{\Delta t} &= -\left[\frac{E^{n+1/1}_{z_{i,j+1,k+1/2}} - E^{n+1/2}_{z_{i,j-1,k+1/2}}}{\Delta y} - \frac{E^{n+1/2}_{y_{i,j+1/2,k+1}} - E^{n+1/2}_{y_{i,j+1/2,k-1}}}{\Delta z}\right] \\
\frac{B^{n+1}_{y_{i+1/2,j,k+1/2}} - B^{n-1}_{x_{i+1/2,j,k+1/2}}}{\Delta t} &= -\left[\frac{E^{n+1/2}_{x_{i+1/2,j,k+1}} - E^{n+1/2}_{x_{i+1/2,j,k-1}}}{\Delta z} - \frac{E^{n+1/2}_{z_{i+1,j,k+1/2}} - E^{n+1/2}_{y_{i-1,j,k+1/2}}}{\Delta x}\right] \\
\frac{B^{n+1}_{z_{i+1/2,j+1/2,k}} - B^{n-1}_{z_{i+1/2,j+1/2,k}}}{\Delta t} &= -\left[\frac{E^{n+1/2}_{y_{i+1,j+1/2,k}} - E^{n+1/2}_{y_{i-1,j+1/2,k}}}{\Delta x} - \frac{E^{n+1/2}_{z_{i+1/2,j+1,k}} - E^{n+1/2}_{x_{i+1/2,j-1,k}}}{\Delta y}\right]
\end{aligned} \tag{B.12}$$

Using Eqs.(B.11) the electric fields at timestep $n + 1/2$ can be found from the value of the electric field at timestep $n - 1/2$ and the value of the magnetic fields and of the current densities at timestep n. Then, using Eqs.(B.12), the magnetic fields at timestep $n+1$ can be found from the value of the magnetic field at timestep $n-1$ and the value of the electric fields at timestep $n+1/2$. In a PIC code also the self-consistent evolution of the current densities under the effect of the electromagnetic fields is taken into account.

The Courant-Friedrichs-Lewy condition for the stability of the scheme is

$$c\Delta t < \frac{1}{\sqrt{\frac{1}{\Delta x^2} + \frac{1}{\Delta y^2} + \frac{1}{\Delta z^2}}}. \tag{B.13}$$

Appendix C

Architect equations and computational mesh

The Architect code equations and centering of the physical quantities on its mesh are reported for reader's convenience.

C.1 Architect equations

The full set of Architect equations is reported:

- The macroparticles equations of motion:

$$\begin{aligned}\frac{d\mathbf{p}_{\mathrm{p}}}{dt} &= -e(\mathbf{E}+\boldsymbol{\beta}_{\mathrm{p}}c\times\mathbf{B}),\\ \frac{d\mathbf{x}_{\mathrm{p}}}{dt} &= \boldsymbol{\beta}_{\mathrm{p}}c,\end{aligned}\tag{C.1}$$

  where the total derivatives are Lagrangian derivatives and $\mathbf{x}_{\mathrm{p}}$, $\mathbf{p}_{\mathrm{p}}$, $\boldsymbol{\beta}_{\mathrm{p}}c$ are the particle p position , momentum and velocity respectively.

- The relativistic cold fluid equations [53] for the plasma electron background, i.e. mass conservation and momentum conservation equations:

$$\begin{aligned}\frac{\partial n_e}{\partial t} + \nabla \cdot (\boldsymbol{\beta}_e c n_e) &= 0, \\ \frac{\partial \mathbf{p}_e}{\partial t} + \boldsymbol{\beta}_e c \cdot \nabla \mathbf{p}_e &= -e(\mathbf{E} + \boldsymbol{\beta}_{\boldsymbol{e}} c \times \mathbf{B}),\end{aligned} \tag{C.2}$$

  where n_e is the electron fluid density, $\boldsymbol{\beta}_e c$ the electron fluid velocity, $\mathbf{p}_e$ the electron fluid momentum.

- The electromagnetic field evolution equations, i.e. Faraday's Law and Ampère-Maxwell's Law respectively:

$$\begin{aligned}\frac{\partial \mathbf{B}}{\partial t} &= -\nabla \times \mathbf{E} \\ \frac{\partial \mathbf{E}}{\partial t} &= e\mu_0 c^3 \left(n_e \boldsymbol{\beta}_e + n_{\mathrm{b}} \boldsymbol{\beta}_{\mathrm{b}}\right) + c^2 \nabla \times \mathbf{B},\end{aligned} \tag{C.3}$$

  where n_{b} is the electron beam density, $\boldsymbol{\beta}_{\mathrm{b}} c$ the electron beam velocity.

The following adimensional quantities are defined in Architect:

$$\begin{aligned}\tilde{x} &= x \cdot \frac{\omega_p}{c}, \\ \tilde{t} &= t \cdot \omega_p, \\ \tilde{n} &= n \cdot \frac{1}{n_0}, \\ \tilde{\mathbf{p}} &= \mathbf{p} \cdot \frac{1}{m_e c}, \\ \tilde{\mathbf{E}} &= \mathbf{E} \cdot \frac{e}{m_e \omega_p c}, \\ \tilde{\mathbf{B}} &= \mathbf{B} \cdot \frac{e}{m_e \omega_p c^2},\end{aligned} \tag{C.4}$$

where x denotes a generic length, t time, $\mathbf{p}$ a generic momentum, n a generic density, n_0 the initial plasma equilibrium density, e the electron charge, m_e the electron mass and $\omega_p = \sqrt{e^2 n_0 / m_e \varepsilon_0}$ the plasma frequency. Using Eqs.(C.4) the code Equations (C.1, C.2, C.3) can be written in adimensional form:

$$\begin{aligned}
\frac{d\tilde{\mathbf{p}}_{\mathrm{p}}}{d\tilde{t}} &= -(\tilde{\mathbf{E}} + \boldsymbol{\beta}_{\mathrm{p}} \times \tilde{\mathbf{B}}), \\
\frac{d\tilde{\mathbf{x}}_{\mathrm{p}}}{d\tilde{t}} &= \boldsymbol{\beta}_{\mathrm{p}} \\
\frac{\partial \tilde{n}_e}{\partial \tilde{t}} + \tilde{\nabla} \cdot (\boldsymbol{\beta}_e \, \tilde{n}_e) &= 0, \\
\frac{\partial \tilde{\mathbf{p}}_e}{\partial \tilde{t}} + \boldsymbol{\beta}_e \cdot \tilde{\nabla} \tilde{\mathbf{p}}_e &= -(\tilde{\mathbf{E}} + \boldsymbol{\beta}_{\boldsymbol{e}} \times \tilde{\mathbf{B}}), \\
\frac{\partial \tilde{\mathbf{B}}}{\partial \tilde{t}} &= -\tilde{\nabla} \times \tilde{\mathbf{E}} \\
\frac{\partial \tilde{\mathbf{E}}}{\partial \tilde{t}} &= (\tilde{n}_e \boldsymbol{\beta}_e + \tilde{n}_{\mathrm{b}} \boldsymbol{\beta}_{\mathrm{b}}) + \tilde{\nabla} \times \tilde{\mathbf{B}}. \qquad \text{(C.5)}
\end{aligned}$$

The details of their integration and the code loop are discussed in Chapter 5.

C.2 Architect mesh

The centering of the physical quantities in Architect is depicted in Fig. C.1, with their indices shown on the mesh. The grid is defined on a $r - z$ reference system follwing the electron beam, which travels in the z direction. The electromagnetic quantities are centered as in the FDTD method (see Appendix B and [84]), with the electric field on the Yee cell edge and the magnetic field cell centered. The fluid quantities (denoted by f in the Figure), i.e. momentum $\mathbf{p}_e$, velocity $\boldsymbol{\beta}_e$, number density n_e, are cell centered. The hydrodynamic mesh is shifted by a quantity Δr in the r direction with respect to the electromagnetic mesh.

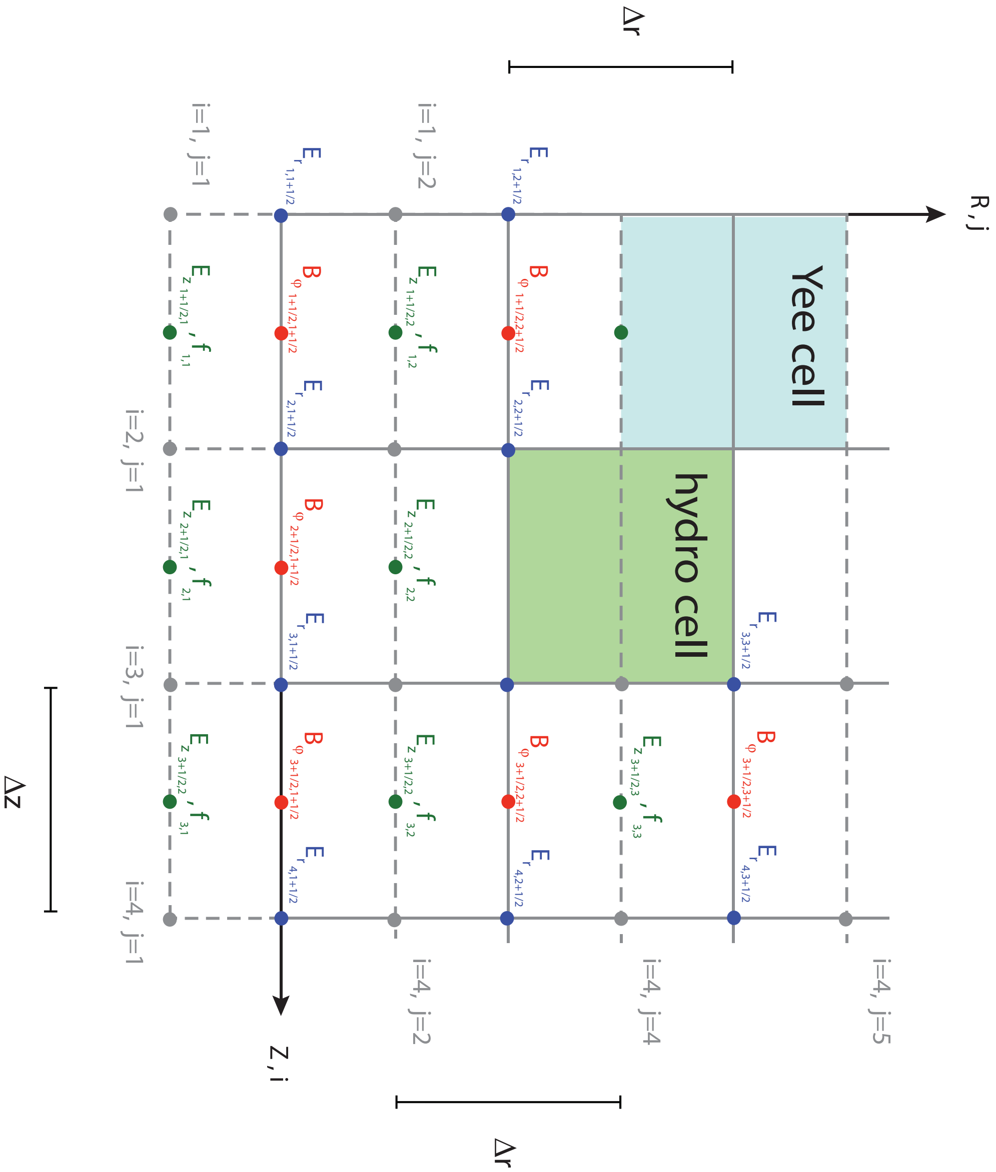

Figure C.1: Centering of the physical quantities in Architect, highlighting the indices used. The generic fluid quantities, i.e. momentum, velocity and number density are denoted with f.

Bibliography

[1] J. M. Dawson. Nonlinear electron oscillations in a cold plasma. *Phys. Rev.*, 113:383–387, 1959.

[2] A. Macchi. *A Super-Intense Laser-Plasma Interaction Theory Primer*. Springer, 2013.

[3] A. I. Akhiezer and R. V. Polovin. Theory of wave motion of an electron plasma. *Sov. Phys. JETP*, 3:696–705, 1956.

[4] A. I. Akhiezer, I. A. Akhiezer, R. V. Polovin, A. G. Sitenko, and K. N. Stepanov. *Plasma Electrodynamics - Nonlinear Theory and Fluctuations*. Pergamon Press, 1975.

[5] R. J. Noble. Plasma Beat-Wave Accelerator. *SLAC-PUB-3149*, 1983.

[6] T. Tajima and J. M. Dawson. Laser electron accelerator. *Phys. Rev. Lett.*, 43(4):267–270, 1979.

[7] E. Esarey, C. B. Schroeder, and W. P. Leemans. Physics of laser-driven plasma-based electron accelerators. *Rev. Mod. Phys.*, 81(3):1229–1285, 2009.

[8] P. Chen, J. M. Dawson, R. W. Huff, and T. Katsouleas. Acceleration of electrons by the interaction of a bunched beam with a plasma. *Phys. Rev. Lett.*, 54(7), 1985.

[9] B. Hidding. Ultracold electron bunch generation via plasma photocathode emission and acceleration in a beam-driven plasma blowout. *Phys. Rev. Lett*, 108(035001), 2012.

[10] V. Malka, A. F. Lifschitz, J. Faure, and Y. Glinec. GeV monoenergetic electron beam with laser plasma accelerator. *International Journal of Modern Physics B*, pages 277–286, 2007.

[11] W. Leemans and E. Esarey. Laser-driven plasma-wave electron accelerators. *Phys. Today*, 62(3):44–49, 2009.

[12] M. Litos et al. High-efficiency acceleration of an electron beam in aplasma wakefield accelerator. *Nature*, 515:92–95, 2014.

[13] F. Massimo, A. Marocchino, E. Chiadroni, M.Ferrario, A.Mostacci, P. Musumeci, and L. Palumbo. Transformer ratio studies for single bunch Plasma Wakefield Acceleration. *Nucl. Instr. and Meth. A*, 740:242–245, 2014.

[14] J. B. Rosenzweig, B. Breizman, T. Katsouleas, and J. J. Su. Acceleration and focusing of electrons in two-dimensional nonlinear plasma wake fields. *Phys. Rev. A*, 44(10):44–49, 1991.

[15] C. Benedetti, A. Sgattoni, G. Turchetti, and P. Londrillo. ALaDyn: A high-accuracy PIC code for the Maxwell–Vlasov equations. *IEEE Transactions on Plasma Science.*, 36(4):1790–1798, 2008.

[16] P. Londrillo, C. Benedetti, A. Sgattoni, and G. Turchetti. Charge preserving high order pic schemes. *Nucl. Instr. and Meth. A*, (1):28–35, 2010.

[17] P. Londrillo, C. Gatti, and M. Ferrario. Numerical investigation of beam-driven PWFA in quasi-nonlinear regime. *Nucl. Instr. and Meth. A*, (740):236–241, 2014.

[18] J. B. Rosenzweig, G. Andonian, M. Ferrario, P. Muggli, O. Williams, V. Yakimenko, and K. Xuan. Plasma wakefields in the quasi-nonlinear regime. *AIP Conference Proceedings*, 1299:500–504, 2010.

[19] K. Nakajima. Plasma wake-field accelerator driven by a train of multiple bunches. *Particle Accelerators*, 32, 1990.

[20] E. Kallos, T. Katsouleas, P. Muggli, I. Pavlishin, I. Pogorelsky, D. Stolyarov, V. Yakimenko, and W. D. Kimura. Plasma wakefield acceleration utilizing multiple election bunches. *Particle Accelerator Conference Proceedings*, 2007.

[21] E. Kallos. *Plasma wakefield accelerator using multiple electron bunches.* PhD thesis, University of Southern California, 2008.

[22] J. B. Rosenzweig, D. B. Cline, B. Cole, H. Figueroa, W. Gai, R. Konecny, J. Norem, P. Schoessow, and J. Simpson. Experimental observation of Plasma Wake-Field Acceleration. *Phys. Rev. Lett.*, 61(1):98–101, 1988.

[23] J. B. Rosenzweig, P. Schoessow, B. Cole, W. Gai, R. Konecny, J. Norem, and J. Simpson. Experimental measurement of nonlinear plasma wake fields. *Phys. Rev. A*, 39(3):1586–1589, 1989.

[24] S. P. D. Mangles et al. Monoenergetic beams of relativistic electrons from intense laser–plasma interactions. *Nature*, 431:535–538, 2004.

[25] C. G. R. Geddes et al. High quality electron beams from a laser wakefield accelerator using plasma-channel guiding. *Nature*, 431:538–541, 2004.

[26] J. Faure et al. Controlled injection and acceleration of electrons in plasma wakefields by colliding laser pulses. *Nature*, 431:737–739, 2004.

[27] W. P. Leemans et al. GeV electron beams from a centimetre-scale accelerator. *Nature Physics*, 2:696–699, 2006.

[28] K. Nakamura et al. GeV electron beams from a centimeter-scale channel guided laser wakefield accelerator. *Physics of Plasmas*, 14(5):696–699, 2007.

[29] P. Muggli et al. Transverse envelope dynamics of a 28.5-GeV electron beam in a long plasma. *Phys. Rev. Lett.*, 88(15), 2002.

[30] P. Muggli et al. A meter-scale plasma wakefield accelerator driven by a matched electron beam. *SLAC-PUB-10738*, 2004.

[31] M. Hogan et al. Multi-GeV energy gain in a plasma-wakefield accelerator. *Phys. Rev. Lett.*, 95:741–744, 2005.

[32] I. Blumenfeld et al. Energy doubling of 42 GeV electrons in a metre-scale plasma wakefield accelerator. *Nature*, 445:741–744, 2007.

[33] T. Katsouleas. Physical mechanisms in the plasma wake-field accelerator. *Phys. Rev. A*, 33:2056–2064, 1986.

[34] J. B. Rosenzweig. Nonlinear plasma dynamics in the plasma wakefield accelerator. *IEEE Transacrions on Plasma Science*, 15(2), 1987.

[35] C. K. Birdsall and A. B. Langdon. *Plasma Physics via Computer Simulation.* Taylor and Francis Group, 2004.

[36] R. W. Hockney and J. W. Eastwood. *Computer Simulation using Partilces.* Taylor and Francis Group, 1988.

[37] G. Lapenta. Particle in Cell method - a brief description of the pic method. Available at `https://perswww.kuleuven.be/~u0052182/weather/pic.pdf`.

[38] P. Sprangle, E. Esarey, and A. Ting. Nonlinear interaction of intense laser pulses in plasmas. *Phys. Rev A*, 41(8), 1990.

[39] P. Mora and T. M. Antonsen Jr. Electron cavitation and acceleration in the wake of an ultraintense, self-focused laser pulse. *Phys. Rev. E*, 53:R2068–R2071, 1996.

[40] P. Mora and T. M. Antonsen Jr. Kinetic modeling of intense, short laser pulses propagating in tenuous plasmas. *Phys. Plasmas*, 4:217–229, 1997.

[41] C. Huang et al. QUICKPIC: A highly efficient particle-in-cell code for modeling wakefield acceleration in plasmas. *Journal of Computational Physics*, 217:658–679, 2006.

[42] W. An, V. K. Decyk, W. B. Mori, and T. M. Antonsen Jr. An improved iteration loop for the three dimensional quasi-static particle-in-cell algorithm: QUICKPIC. *Journ. Comput. Phys.*, 250:165–177, 2013.

[43] T. Mehrling, C. Benedetti, C. B. Schroeder, and j. Osterhoff. HiPACE: a quasi-static particle-in-cell code. *Plasma Phys. Control. Fusion*, 56:658–679, 2014.

[44] K. V. Lotov. Simulation of ultrarelativistic beam dynamics in plasma wake-field accelerator. *Phys. Plasmas*, 5(785), 1998.

[45] C. Benedetti, C. B. Schroeder, E. Esarey, C. G. R. Geddes, and W. P. Leemans. Efficient modeling of laser-plasma accelerators with INF&RNO. *14th Advanced Accelerator Concepts Workshop Proc.*, 2010.

[46] P. Tomassini. Internal note, describing the code QFluid. Available at `/http://agenda.infn.it/getFile.py/access?resId=0&materialId=slides&confId=3444S`.

[47] A. F. Lifschitz, X. Davoine ad E. Lefebvrec, J. Faure, C. Rechatin, and V. Malka. Particle-in-cell modelling of laser–plasma interaction using fourier decomposition. *J. Comput. Phys.*, 228(5):1803—-1814, 2009.

[48] M. Ferrario et al. SPARC_LAB present and future. *Nucl. Instr. and Meth. B*, (309):183–188, 2013.

[49] M. Ferrario et al. Laser comb with velocity bunching: Preliminary results at SPARC. *Nucl. Instr. and Meth. A*, 637:S43–S46, 2011.

[50] M. P. Anania et al. Design of a plasma discharge circuit for particle wakefield acceleration. *Nucl. Instr. and Meth. A*, 740:193–196, 2014.

[51] D. R. Nicholson. *Introduction to Plasma Theory.* John Wiley and Sons, 1983.

[52] P. M. Bellan. *Fundamentals of Plasma Physics.* Cambridge University Press, 2006.

[53] L. Rezzolla and O. Zanotti. *Relativistic Hydrodynamics.* Oxford University Press, 2013.

[54] A. Isihara. *Statistical Physics.* Academic Press Inc., 1971.

[55] K. Huang. *Statistical Mechanics.* John Wiley and Sons, 1987.

[56] H. Goldstein, C. Poole, and J. Safko. *Classical Mechanics.* Addison-Wesley, 2002.

[57] J. V. Jose' and E. J. Salentan. *Classical Dynamics: a Contemporary Approach.* Cambridge University Press, 1998.

[58] F. M. White. *Fluid Mechanics.* McGraw-Hill, 2008.

[59] C. Clarke and R. Carswell. *Principles of Astrophysical Fluid Dynamics.* Cambridge University Press, 2007.

[60] F. Pegoraro and F. Porcelli. Equation of state for relativistic plasma waves. *Phys. Fluids*, 27(6), 1984.

[61] L. Palumbo, J. B. Rosenzweig, and L. Serafini. *The Physics and Applications of High Brightness Electron Beams - Proc. 46th Workshop of the INFN ELOISATRON Project.* World Scientific, 2005.

[62] P. Schmüser, M. Dohlus, and J. Rossbach. *Ultraviolet and Soft X-Ray Free Electron Lasers.* Springer, 2008.

[63] J. Buon. Beam phase space and emittance. *CERN 94-01, CERN, 1992*, 69, 1992.

[64] T. P. Wangler. *Principles of RF Linear Accelerators.* John Wiley and Sons, 1998.

[65] M. Reiser. *Theory and Design of Charged Particle Beams.* John Wiley and Sons, 2008.

[66] J. D. Lawson et al. Emittance, entropy and information. *Particle Accelerators*, 5, 1973.

[67] S. Humphries. *Charged particle beams*. John Wiley and Sons, 1990.

[68] A. Cianchi et al. Challenges in plasma and laser wakefield accelerated beams diagnostic. *Nucl. Instr. and Meth. A*, 720, 2013.

[69] A. Cianchi et al. Intrinsic normalized emittance growth in laser-driven electron accelerators. *Phys. Rev. Special Topics*, 16, 2013.

[70] J. B. Rosenzweig. *Fundamentals of Beam Physics*. Oxford University Press, 2003.

[71] M. Ferrario. Accelerator physics: basic principles on beam focusing and transport. *SPARC-BD-12/01*, 2012.

[72] K. Schindl. Space charge. *Report CERN/PS 99-012*, 1988.

[73] T. P. Coffey. Breaking of large amplitude plasma oscillations. *Phys. Fluids*, 14(1402), 1971.

[74] T. Katsouleas and W. B. Mori. Wave-breaking amplitude of relativistic oscillations in a thermal plasma. *Phys. Rev. Lett.*, 61(90), 1988.

[75] J. B. Rosenzweig. Trapping, thermal effects, and wave breaking in the nonlinear plasma wake-field accelerator. *Phys. Rev. A*, 38(3634), 1988.

[76] Z. M. Sheng and J. Meyer ter Vehn. Relativistic wave breaking in warm plasmas. *Physics of Plasmas*, 4(493), 1997.

[77] K. F. Bane, P. B. Wilson, and T. Weiland. Wake fields and wake field acceleration. *SLAC-PUB-3528*, 1984.

[78] P. Schutt, T. Weiland, and V. M. Tsakanov. On the wake field acceleration using the sequence of driving bunches. *Report DESY M88-13*, 1988.

[79] J. G. Power, W.Gai, X. Sun, and A. Kanareykin. Transformer ratio enhancement using a ramped bunch train in a collinear wakefield accelerator. *PAC 2001 Proceedings*, 1:114–116, 2001.

[80] J. Dawson. One-dimensional plasma model. *Phys. Fluid*, 5:455–459, 1962.

[81] J. M. Dawson. Particle simulation of plasmas. *Rev. Mod. Phys.*, 55(2):403–447, 1983.

[82] J. P. Boris. Relativistic plasma simulation-optimization of a hybrid code. *Proc. Fourth Conf. Num. Sim. Plasmas*, pages 3–67, 1970.

[83] M. V. K. Chari and S. J. Salon. *Numerical Methods in Electromagnetism.* Academic Press, 2004.

[84] K. Yee. Numerical solution of initial boundary value problems involving maxwell's equations in isotropic media. *IEEE Transactions on Antennas and Propagation*, 14(3):302–307, 1966.

[85] L. Landau. On the vibrations of electronic plasmas. *Journal of Physics*, XX, 1946.

[86] A. Marocchino. From 1D fluid model to 3D PIC simulations for resonant PWFA experiments at SPARC_LAB. Presented as the 3rd Topical Workshop on Novel Accelerating Techniques, Dresda, 2014.

[87] K. V. Lotov. Fine wakefield structure in the blowout regime of plasma wakefield accelerators. *Phys. Rev. ST Accel. Beams*, 6, 2003.

[88] K. V. Lotov. Blowout regimes of plasma wakefield acceleration. *Phys. Rev. E*, 69, 2004.

[89] H. Burau, R. Widera, W. Hönig, G. Juckeland, A. Debus, T. Kluge, U. Schramm, T. E. Cowan, R. Sauerbrey, and M. Bussmann. PIConGPU : A fully relativistic particle-in-cell code for a GPU cluster. *IEEE Transactions on plasma science*, 38(10):2831–2839, 2010.

[90] A. R. R. Rossi et al. The external-injection experiment at the sparc_lab facility. *Nucl. Instr. and Meth. A*, 740:216–221, 2014.

[91] J. P. Boris and D. L. Book. Flux-Corrected Transport I. SHASTA, a fluid transport algorithm that works. *J. Comput. Phys.*, 11(38):248–283, 1973.

[92] S. T. Zalesak. Fully multidimensional Flux-Corrected Transport algorithms for fluids. *J. Comput. Phys.*, 31(38):335–362, 1979.

[93] C. B. Laney. *Computational Gasdynamics.* Cambridge University Press, 1998.

[94] A. Marocchino and F. Massimo et al. Hybrid-code and PIC-code simulations for PWFA at SPARC_LAB. *talk at 2nd European Advanced Accelerator Concepts Workshop*, 2015.

[95] R. J. LeVeque. *Finite Difference Methods for Ordinary and Partial Differential Equations: Steady-State and Time-Dependent Problems.* Society for Industrial and Applied Mathematics, 2007.

[96] N. Barov, J. B. Rosenzweig, M.C. Thompson, and R. B. Yoder. Energy loss of a high-charge bunched electron beam in plasma: Analysis. *Phys. Rev. Special Topics - Accelerators and Beams*, 7, 2004.

[97] W. Lu, C. Huang, M. Zhou, W. B. Mori, and T. Katsouleas. Nonlinear theory for relativistic plasma wakefields in the blowout regime. *Phys. Rev. Lett.*, 96(165002), 2006.

[98] W. Lu, C. Huang, M. Zhou, M. Tzoufras, F. S. Tsung, W. B. Mori, and T. Katsouleas. A nonlinear theory for multidimensional relativistic plasma wave wakefields. *Physics of Plasmas*, 13(056709), 2006.

[99] D. Alesini et al. The SPARC project: a high brightness electron beam source at LNF to drive a SASE-FEL experiment. *Nucl. Instr. and Meth. A*, 507:345–349, 2003.

[100] M. Ferrario et al. Direct measurement of the double emittance minimum in the beam dynamics of the Sparc high-brightness photoinjector. *Phys. Rev. Lett.*, 99(234801), 2007.

[101] P. Oliva et al. Start-to-end simulation of a thomson source for mammography. *Nucl. Instr. and Meth. A*, 615:93–99, 2010.

[102] E. Chiadroni et al. The THz radiation source at SPARC. *Journal of Physics Conference Series*, 357(012034), 2012.

[103] R. Pompili et al. First single-shot and non-intercepting longitudinal bunch diagnostics for comb-like beam by means of Electro-Optic Sampling. *Nucl. Instr. and Meth. A*, 740:216–221, 2014.

[104] L. Giannessi et al. Self-amplified spontaneous emission free-electron laser with an energy-chirped electron beam and undulator tapering. *Phys. Rev. Lett.*, 106(144801), 2011.

[105] M. Labat et al. High-gain harmonic-generation free-electron laser seeded by harmonics generated in gas. *Phys. Rev. Lett.*, 107(224801), 2011.

[106] L. Giannessi et al. High-order-harmonic generation and superradiance in a seeded free-electron laser. *Phys. Rev. Lett.*, 108(164801), 2012.

[107] A. Marocchino et al. Study of plasma wakefield acceleration mechanism for emittance dominated regimes via hybrid and PIC simulations. *talk at 42nd European Physicsl Society Conference on Plasma Physics*, 2015.

[108] T. Mehrling, J. Grebenyuk, F. S. Tsung, K. Floettmann, and J. Osterhoff. Transverse emittance growth in staged laser-wakefield acceleration. *Phys. Rev. Special Topics*, 15(11303), 2012.

[109] K. Floettmann. Adiabatic matching section for plasma accelerated beams. *Phys. Rev. Special Topics*, 17(054402), 2014.

[110] G. A. Voss and T. Weiland. The wakefield acceleration mechanism. *Report DESY M82-10*, 1982.

[111] J. T. Seeman. Collective electron driven linac for high energy physics. *IEEE Transactions on Nuclear Science*, NS-30(4), 1983.

[112] K. F. Bane, P. Chen, and P. B. Wilson. On collinear wake field acceleration. *IEEE Transactions on Nuclear Science*, NS-32(5), 1985.

[113] E. M. Laziev, V. M. Tsakanov, and S. S. Vahanyan. Electromagnetic wave generation with high transformation ration by intense charged particle bunches. *YERPHI*, 1040(3), 1988.

[114] T. Katsouleas, S. Wilks, P. Chen, J. M. Dawson, and J. J. Su. Beam loading in plasma accelerators. *Particle Accelerators*, (22), 1987.

[115] M. Tzoufras, W. Lu, F. S. Tsung, C. Huang, W. B. Mori, T. Katsouleas, J. Vieira, R. A. Fonseca, and L. O. Silva. Beam loading in the nonlinear regime of plasma-based acceleration. *Phys. Rev. Lett.*, 145002(101), 2009.

[116] M. Tzoufras, W. Lu, F. S. Tsung, C. Huang, W. B. Mori, T. Katsouleas, J. Vieira, R. A. Fonseca, and L. O. Silva. Beam loading by electrons in nonlinear plasma wakes. *Physics of Plasmas*, 056705(16), 2009.

[117] A. Piel. *Plasma Physics - An Introduction to Laboratory, Space and Fusion Plasmas.* Springer, 2010.

[118] L. D. Landau and E. M. Lifschitz. *Course of Theoretical Physics - Mechanics*, volume 1. Pergamon Press, 3 edition, 1991.

[119] D. V. Sivukhin. Coulomb collisions in a fully ionized plasma. *Reviews of Plasma Physics, Edited by M. A. Leontovich. Published by Consultants Bureau, New York*, 4(16):93, 1966.

[120] H. Hora. *Plasmas at High Temperature and Density.* Springer-Verlag, 1991.

List of Figures